

Yu Huang · Min Xiong · Liuyuan Zhao

Slope Stochastic Dynamics

 Springer

Slope Stochastic Dynamics

Yu Huang · Min Xiong · Liuyuan Zhao

Slope Stochastic Dynamics

 Springer

Yu Huang
Department of Geotechnical Engineering,
College of Civil Engineering
Tongji University
Shanghai, China

Min Xiong
Department of Geotechnical Engineering,
College of Civil Engineering
Tongji University
Shanghai, China

Liuyuan Zhao
Power China Huadong Engineering
Corporation Limited
Hangzhou, Zhejiang, China

Department of Geotechnical Engineering,
College of Civil Engineering
Tongji University
Shanghai, China

ISBN 978-981-16-9696-1

ISBN 978-981-16-9697-8 (eBook)

<https://doi.org/10.1007/978-981-16-9697-8>

© The Editor(s) (if applicable) and The Author(s), under exclusive license to Springer Nature Singapore Pte Ltd. 2022

This work is subject to copyright. All rights are solely and exclusively licensed by the Publisher, whether the whole or part of the material is concerned, specifically the rights of translation, reprinting, reuse of illustrations, recitation, broadcasting, reproduction on microfilms or in any other physical way, and transmission or information storage and retrieval, electronic adaptation, computer software, or by similar or dissimilar methodology now known or hereafter developed.

The use of general descriptive names, registered names, trademarks, service marks, etc. in this publication does not imply, even in the absence of a specific statement, that such names are exempt from the relevant protective laws and regulations and therefore free for general use.

The publisher, the authors and the editors are safe to assume that the advice and information in this book are believed to be true and accurate at the date of publication. Neither the publisher nor the authors or the editors give a warranty, expressed or implied, with respect to the material contained herein or for any errors or omissions that may have been made. The publisher remains neutral with regard to jurisdictional claims in published maps and institutional affiliations.

This Springer imprint is published by the registered company Springer Nature Singapore Pte Ltd. The registered company address is: 152 Beach Road, #21-01/04 Gateway East, Singapore 189721, Singapore

Preface

The nonlinear seismic dynamic response analysis of slopes is challenged by the coupled effects of geological parameter uncertainties, dynamic nonlinearity, and the randomness of ground motion. An effective method to accurately describe the influence of these coupled phenomena has therefore become an important research focus in academic and industrial circles to effectively evaluate the seismic dynamic stability and seismic dynamic performance of natural and artificial slopes. The core difficulty of this problem is that slopes under seismic dynamic action are an extremely complex nonlinear stochastic dynamic system. Traditional classical deterministic slope seismic response analysis theory and probability theory are poorly suited to accurately and effectively simulate, analyze, and assess the nonlinear seismic dynamic stability of this complex object within a unified framework.

Numerous years of extensive effort have been devoted to resolve this problem with extensive engineering applications and theoretical studies based on free theory exploration and practical experience of slope engineering anti-seismic analysis. A new theoretical tool of stochastic dynamics is introduced in this book to access the seismic dynamic stability performance of slopes and explore a unified technical route of stochastic dynamics. In this regard, a new framework and method are introduced to model, analyze, and evaluate the nonlinear random seismic dynamic response of slopes using a systematic combination and development of previous research results. A full intensity-frequency non-stationary stochastic ground motion model is preliminarily established to characterize the randomness of earthquakes based on the time-domain stochastic process description. A spatial distribution random field model of rock and soil materials is established to characterize the spatio-temporal variability of the geotechnical parameters. A new nonlinear stochastic seismic dynamic performance assessment method is introduced, and a nonlinear seismic dynamic stability assessment framework of slope engineering based on dynamic reliability is established according to the basic theory of stochastic dynamics. Slope seismic dynamic model tests are performed based on physical simulations and large complex shaking table experiments to verify and modify the proposed framework, and some practical application studies are carried out.

This book discusses the source and characterization of randomness and the analysis of the nonlinear stochastic seismic dynamic response of slope seismic dynamic systems from the basic viewpoint of nonlinear stochastic dynamics.

Chapter 1 introduces and summarizes the latest progress in seismic design and evaluation in slope engineering, especially the development of slope seismic reliability in the field. The main dynamic analysis methods and currently developed impact factors are reviewed.

Chapter 2 presents a reasonable description of ground motion randomness at slope sites and the characterization of spatio-temporal variability of the slope geotechnical parameters. This chapter introduces the main theoretical framework of stochastic dynamics for nonlinear stochastic seismic dynamic response analysis of slope systems and its general process.

Chapters 3 and 4 present the numerical simulations and applications of the above theory on slope engineering, such as slope and earth dams for nonlinear stochastic seismic dynamic response and dynamic stability performance analysis.

Chapter 5 describes the large-scale seismic table shaking test performed to verify the simulation results.

Chapter 6 summarizes the main conclusions of this book and presents future prospects for slope nonlinear stochastic seismic dynamics.

This book presents a condensed and improved summary of previous research results. Standing upon the shoulders of predecessors in the field, previous studies are systematically sorted out and the most relevant research results are presented as a form of inheritance and ongoing development of predecessors' research, to whom my heartfelt thanks are sincerely conveyed. This book includes a wealth of references to help readers better understand the history and scope of the topic.

The research invested in the development of this book has received support from the National Science Fund for Distinguished Young Scholars (41625011), the National Natural Science Foundation for Young Scientists of China (41902274), the National Natural Science Foundation of China (51778467), the State Key Program of National Natural Science of China (Grant No. 41831291), the National Key Research and Development Program of China (2017YFC1501304), and the Sino-German mobility programme (NSFC/DFG) (M-0129). The authors thank the related publishers, including Springer, Elsevier, and the American Society of Civil Engineers for their kind authorization to reuse some of the content presented herein. The authors would like to convey their sincere thanks and respect for the aforementioned support.

I would like to thank the joint research group of graduate students who have made their own contributions, including Dr. Min Xiong, Dr. Liuyuan Zhao, Dr. Hongqiang Hu, Mr. Xuri Li, Ms. Lu Zhao, Ms. Guiying Dong, Ms. Lingling Zeng, Ms. Geye Li, Ms. Wenwen Wang, Ms. Mi Zhou, Ms. Ying Luo, Ms. Cuizhu Zhao, and Mr. Zhiming Peng. Their long-term beneficial discussions and pondering are ultimately what led to the development of this book, and I would like to take this opportunity to express my sincere appreciation for their creative work.

It is my hope that this book will provide theoretical and technical reference for geotechnical engineers and researchers in the anti-seismic slope engineering practice,

as well as serve as a milestone for further research and development of slope seismic nonlinear stochastic dynamics. Moreover, I hope readers will obtain a genuine understanding of slope nonlinear stochastic dynamics, not just in terms of knowledge and facts of slope seismic dynamic response. Although the basic theoretical framework of nonlinear stochastic seismic dynamic response analysis of slope systems is systematically established, it remains impossible to indefinitely solve all problems in light of the complexity and difficulty of nonlinear dynamic response of slope engineering under earthquake excitation conditions. The research content of this book is therefore open, and suggestions and criticism from readers are welcomed.

Shanghai, China
October 2021

Yu Huang

Contents

1	Introduction	1
1.1	Background	1
1.2	Slope Seismic Dynamic Response Analysis Methods	2
1.2.1	Deterministic Slope Seismic Dynamic Response Analysis Methods	2
1.2.2	Stochastic Slope Seismic Dynamic Response Analysis Methods	7
1.3	Limitations and Deficiencies of Existing Methods	15
1.3.1	Spatial Variability of Rock and Soil Parameters	16
1.3.2	Randomness of Seismic Ground Motion	18
1.3.3	Compound Randomness	19
1.4	Aim of This Book	20
	References	21
2	Theoretical Framework of Slope Stochastic Dynamics	27
2.1	General Process of Stochastic Seismic Dynamic Response Analysis	28
2.2	Probability Density Evolution Method	29
2.2.1	Principle of Probabilistic Conservation	30
2.2.2	Generalized Probability Density Evolution Equation	32
2.2.3	Numerical Solution of the GDEE	33
2.3	Random Field Expression of Spatial Variability of Slope Rock and Soil Parameters	34
2.4	Seismic Ground Motion Models	38
2.4.1	Stochastic Seismic Ground Motion Model	39
2.4.2	Ground Motion Synthesis Method Based on Stochastic Process Theory	46
	References	49

3	Numerical Simulation and Application of Slope Stochastic Seismic Response Analysis	53
	3.1 Slope Stochastic Seismic Analysis Methods	54
	3.1.1 Slope Dynamic Stability Analysis Method	54
	3.1.2 Finite Element Reliability Analysis Framework Based on PDEM	56
	3.2 Description of Stochastic Factors of Slope	58
	3.2.1 Generation of Stochastic Fields	59
	3.2.2 Stochastic Seismic Ground Motion Model	63
	3.3 Slope Stochastic Seismic Response Analysis	67
	3.4 Slope Nonlinear Stochastic Seismic Dynamic Reliability Analysis	71
	3.4.1 Principles of Slope Reliability Analysis	71
	3.4.2 Results of Slope Stochastic Seismic Dynamic Reliability Analysis	72
	3.5 Verification of Slope Reliability Analysis Method Based on PDEM	73
	3.5.1 Monte Carlo Simulations	73
	3.5.2 Verification Using a Closed Form Analytical Solution	78
	References	82
4	Dynamic Failure Mechanism and Post-failure Behavior Analysis of Slopes	85
	4.1 Evolution Process of Slope Failure	85
	4.2 Dynamic Failure Processes and Slope Failure Mechanism	87
	4.2.1 Dynamic Solution Steps	88
	4.2.2 Slope Dynamic Calculation Model	88
	4.2.3 Extraction of Dynamic Slip Surface Based on the Plastic Strain Increment	91
	4.2.4 Failure Process Analysis Based on Stochastic Seismic Ground Motion	94
	4.3 Critical Slip Surface Determination and Landslide Volume Analysis	96
	4.3.1 Model of Slope Stochastic Dynamic Analysis	96
	4.3.2 Dynamic Slip Surface and Instability Volume of Slopes	99
	4.3.3 Evolution Law of Slope Instability Volume	100
	4.3.4 Stochastic Seismic Risk Assessment of Slope	101
	4.4 Slope Post-failure Behavior Under Random Earthquake Based on Smoothed Particle Hydrodynamics	103
	4.4.1 SPH Model of Soil Flow Hazards	104
	4.4.2 Simulation of Random Field	104
	4.4.3 Large Deformation Analysis of Soil Flow Hazards	106
	References	112

- 5 Nonlinear Stochastic Dynamic Seismic Response Analysis of Slopes Based on Large Shaking Table Tests** 115
 - 5.1 Model Design for Large Shaking Table Test 117
 - 5.1.1 Size Determination of Slope Model 117
 - 5.1.2 Material Production of Slope Model 121
 - 5.1.3 Construction and Measurement of Slope Model 126
 - 5.1.4 Ground Motion Generation and Response Acquisition 131
 - 5.2 Seismic Response Analysis of Slope Model 132
 - 5.2.1 Dynamic Characteristics of the Slope Model 134
 - 5.2.2 Stochastic Dynamic Response Analysis of Slope 137
 - 5.2.3 Seismic Dynamic Reliability Analysis of Slope 146
 - 5.3 Comparison with Numerical Modeling Results 146
 - References 149
- 6 Conclusions and Prospects** 151
 - 6.1 Conclusions 151
 - 6.2 Prospects 153

About the Authors

Prof. Yu Huang born in 1973, received his Ph.D. in Geotechnical Engineering from Tongji University, Shanghai, China. He is now a “Distinguished Professor of Changjiang Scholars of the Ministry of Education” in geological engineering in the College of Civil Engineering at Tongji University. Professor Huang’s primary research area includes earthquake geotechnical engineering, geologic disasters, computational geomechanics, foundation engineering, and environmental geology. He has authored more than 200 technical publications, including more than 120 papers in international refereed journals such as the *Bulletin of Engineering Geology and the Environment*, *Engineering Geology*, *Landslides*, *Natural Hazards*, *Environmental Earth Sciences*, *Geotextiles and Geomembranes*, and *Acta Geotechnical*. As first author, he has written two monographs entitled “Geo-disaster modeling and analysis: An SPH-based approach” published by Springer-Verlag in 2014 and “Hazard Analysis of Seismic Soil Liquefaction” published by Springer-Verlag in 2017. He now serves on the editorial board for the *Engineering Geology* (Elsevier), *Bulletin of Engineering Geology and the Environment* (the official journal of IAEG, Springer), *Geotechnical Research* (ICE), and *Geoenvironmental Disasters* (Springer). Professor Huang received the National Science Fund for Distinguished Young Scholars from the National Natural Science Foundation of China for his research on geological disasters triggered by earthquakes.

Min Xiong born in 1986, received his Ph.D. from Tongji University under the guidance of Prof. Yu Huang. He received his bachelor’s and master’s degrees in civil engineering at Three Gorges University. He is currently working at Tongji University as a post-doctoral research fellow.

Liuyuan Zhao born in 1990, received his bachelor’s degree and Ph.D. from Tongji University under the guidance of Prof. Yu Huang. He is currently working at the Power China Huadong Engineering Corporation Limited as a post-doctoral research fellow.

List of Figures

Fig. 1.1	Acceleration (a) and frequency spectrum information (b) of two earthquakes at the same site (data from the PEER database)	19
Fig. 1.2	Basic logical framework of this book	21
Fig. 2.1	Theoretical framework and research contents of stochastic dynamic analysis of slope under seismic activity	28
Fig. 2.2	From the randomness of a slope seismic dynamic system to the nonlinear stochastic seismic dynamic response of a slope	31
Fig. 2.3	Examples of two cross-correlated non-Gaussian random fields of the cohesion (a) and friction angle (b)	38
Fig. 2.4	Typical non-stationary seismic acceleration time series	47
Fig. 3.1	Flow chart of slope reliability analysis using the PDEM	58
Fig. 3.2	Slope geometry for reliability analysis	61
Fig. 3.3	Finite element model of a slope for reliability analysis	62
Fig. 3.4	Typical realization of cohesion stochastic field	63
Fig. 3.5	Representative samples of non-stationary stochastic ground motions	66
Fig. 3.6	Comparison of the mean and standard deviation between the population and target of the non-stationary stochastic ground motion samples	66
Fig. 3.7	PDFs of the slope safety factor under a single random factor	68
Fig. 3.8	Equal probability density contour of the slope safety factor under a single random factor (5–6 s)	68
Fig. 3.9	Mean and standard deviation of the slope safety factor under dual random factors	69
Fig. 3.10	PDFs of the slope safety factor at different times under dual random factors	69
Fig. 3.11	Slope safety factor probability density evolution surface under dual random factors (5–6 s)	69

Fig. 3.12 Slope safety factor probability density contour under double random factors (5–6 s) 70

Fig. 3.13 Solution modes of slope reliability analysis 72

Fig. 3.14 PDF of the slope safety factor based on extreme events in the limit state 73

Fig. 3.15 CDF of the slope safety factor based on extreme events in the limit state 73

Fig. 3.16 PDF of the safety factor calculated based on the PDEM and MCS methods under static conditions 74

Fig. 3.17 CDF of the safety factor calculated based on the PDEM and MCS methods under static conditions 75

Fig. 3.18 Relation diagram between clay G_{max} and effective stress 76

Fig. 3.19 Time history curve of the slope safety factor 77

Fig. 3.20 Mean and sandard deviation values of the safety factors calculated based on the PDEM and MCS methods under dynamic conditions 77

Fig. 3.21 PDF of slope safety factor calculated by the PDEM and MCS methods at $t = 5$ s 78

Fig. 3.22 PDF of the slope safety factor calculated by the PDEM and MCS methods at $t = 8$ s 78

Fig. 3.23 Comparison of the slope safety factor PDF under extreme conditions 79

Fig. 3.24 Comparison of the slope safety factor CDF under extreme conditions 79

Fig. 3.25 PDF of the displacement response in a single-degree-of-freedom system ($t = 1$ s) (reprinted from Huang et al. 2015 with permission of Elsevier) 81

Fig. 3.26 Second-order statistics information (mean and standard deviation) of a single-degree-of-freedom system (reprinted from Huang et al. 2015 with permission of Elsevier) 82

Fig. 4.1 Flow chart of entire process of slope instability and failure evolution under seismic dynamic excitation conditions 86

Fig. 4.2 Model of a homogeneous soil slope **a** and sketch of the finite element mesh in FLAC2D **b** 89

Fig. 4.3 2D Slope profile: typical monitoring points area **a**; partial monitoring profiles for shear strain analysis **b** 90

Fig. 4.4 Time history of plastic strain of the slope profile under wave 1 92

Fig. 4.5 Process of determining the sliding surface position for wave 10: PGA = 0.4 g **a** and wave 100, PGA = 0.4 g **b** 93

Fig. 4.6 Position of the dynamic slip surface quantified under earthquake action 93

Fig. 4.7	Final plastic strain contours under earthquake action (wave 1, PGA = 0.4 g) (reprinted from Zhao et al. (2020) with permission of Elsevier)	94
Fig. 4.8	Deformation development patterns of slope based on the normalized shear strain and shear strain rate time history (reprinted from Zhao et al. (2020) with permission of Elsevier)	95
Fig. 4.9	Minimum FOS distributions of a slope under random earthquakes: PDF for PGA = 1 m/s ² a ; CDF for PGA = 1 m/s ² b ; PDF for PGA = 2 m/s ² c CDF for PGA = 2 m/s ² d (reprinted from Huang et al. (2018) with permission of Springer)	98
Fig. 4.10	Computational step of the critical slip surface based on the FOS curve (reprinted from Huang et al. (2018) with permission of Springer)	99
Fig. 4.11	Probability density evolutionary surface of the landslide volume (reprinted from Huang et al. (2018) with permission of Springer)	100
Fig. 4.12	Landslide volume uncertainty calculated by the MCM and PDEM: a PDF; b CDF (reprinted from Huang et al. (2018) with permission of Springer)	102
Fig. 4.13	Landslide depth uncertainty: PDF a ; CDF b (reprinted from Huang et al. (2018) with permission of Springer)	102
Fig. 4.14	Sliding volume determined by the plastic strain increment method (reprinted from Zhao et al. (2020) with permission of Elsevier)	103
Fig. 4.15	Homogeneous ideal slope model (units: m) (reprinted from Huang et al. (2020) with permission of Springer)	104
Fig. 4.16	Realization of a stochastic field of the cohesive force	106
Fig. 4.17	Realization of a stochastic field of the internal friction force	106
Fig. 4.18	Time history curve of ground motion	107
Fig. 4.19	SPH simulation process	108
Fig. 4.20	Mean and standard deviation time-history curves of the run-out distance considering spatial variability	109
Fig. 4.21	Mean and standard deviation time-history curves of the flow depth considering spatial variability	109
Fig. 4.22	PDF curve of run-out distance under typical moments considering spatial variability	109
Fig. 4.23	Three-dimensional surface of the probability density variation of run-out distance considering spatial variability	110
Fig. 4.24	Equal-probability density plot of the run-out distance considering spatial variability	110
Fig. 4.25	PDF curve of the run-out distance considering spatial variability	110

Fig. 4.26 CDF curve of the run-out distance considering spatial variability 111

Fig. 4.27 PDF curve of the flow depth considering spatial variability 111

Fig. 4.28 CDF curve of the flow depth considering spatial variability 112

Fig. 5.1 Rigid model box 120

Fig. 5.2 Frequency test results of the shaking table rigid box in the time and frequency domains (reprinted from Zhao et al. (2020) with permission of Elsevier) 121

Fig. 5.3 Variance on the elastic modulus and Poisson’s ratio of slope materials (modified from Engineering Geology Manual (2007)) 122

Fig. 5.4 Model side dyed sand treatment **a** and view of grid line **b** 127

Fig. 5.5 High-speed camera **a**, light source **b**, and lighting effect diagram during excitation with the shuttering time of 0.1 μ s **c** 130

Fig. 5.6 Stochastic response acceleration sensor observation profile 131

Fig. 5.7 Rock slope with gridlines on the plexiglass box 134

Fig. 5.8 White noise input temporal waveform and frequency power spectrum of the slope model 135

Fig. 5.9 White noise response spectra at different elevations of the slope model 136

Fig. 5.10 Seismic sample excitation sequence 137

Fig. 5.11 Response and frequency spectra of the A9 sensor inside the slope under different seismic input conditions (No. means the number of ground motions) 138

Fig. 5.12 Horizontal acceleration response along the elevation profile under one seismic excitation 139

Fig. 5.13 Time history curve of the ground motion captured in the typical test 140

Fig. 5.14 PDFs of the acceleration at 1, 10, 20, and 29 s recorded on sensors A29 **a**, A9 **b**, and A1 at different elevations **c**. PDFs of the acceleration at 5, 10, 15, and 20 s recorded on sensors A29 **d**, A9 **e**, and A1 at different elevations **f** 140

Fig. 5.15 Acceleration probability density evolution surface at sensor A29 141

Fig. 5.16 PDFs on the time-varying displacement at the slope top 141

Fig. 5.17 PDFs of the vertical settlement at different elevations of the slope model when the time is 1s, 10s and 20s 142

Fig. 5.18 PDF curves of the acceleration elevation amplifying factor 143

Fig. 5.19 CDF curves of the acceleration elevation amplifying factor 143

Fig. 5.20 Amplifying coefficient curves based on the average response spectrum under seismic excitation conditions **a**, **b**, and amplifying coefficient curves based on the average Fourier spectrum under seismic excitation conditions **c**, **d** 144

Fig. 5.21	Comparison of the different amplifying factors with elevation during ground motion input (reprinted from Zhao et al. (2020) with permission of Elsevier)	145
Fig. 5.22	Dynamic reliability of slope top cracking failure based on critical acceleration	147
Fig. 5.23	Displacement contours of the 3D calculation model and test seismic excitation input	148
Fig. 5.24	Gaussian white noise time and frequency spectra a,b , respectively. Dynamic characteristics test of the Gaussian white noise model c	148
Fig. 5.25	Horizontal acceleration response of sensor A9 in the slope under ground motion Wn 1	149

List of Tables

Table 2.1	Improved filter white noise models	42
Table 2.2	Intensity non-stationary random vibration model	43
Table 2.3	Commonly used strength envelope functions	43
Table 2.4	Two spectral representation methods of ground motion acceleration process simulation	48
Table 3.1	Parameter values of the generalized evolution spectrum model of non-stationary ground motion	65
Table 3.2	Comparison of the first two-order statistics and failure probability of the PDEM and MCS methods	75
Table 4.1	Parameters for FLAC2D slope model	90
Table 4.2	Statistical characteristics of soil parameters	105
Table 5.1	Pivotal parameters of the shaking table	118
Table 5.2	Reference slope shaking table model rigid box dimensions ...	119
Table 5.3	Engineering parameters of slope shaking table test model box	119
Table 5.4	Classification of shaking table slope model material based on previous studies	122
Table 5.5	Well-proportioned model rock material in the model test	123
Table 5.6	Dynamic similarity ratio of key physical dimension derivation	124
Table 5.7	Similarity ratio affirmation of the test physical dimensions with the Buckingham π theorem	125
Table 5.8	Comparison between slope prototype and model parameters	126
Table 5.9	Test sensors in the shaking table model	128
Table 5.10	Detailed parameters of the multi-type sensors (JF106T, DH105E)	129

Table 5.11 Detailed parameters of the I-SPEED 7 series high-speed cameras 130

Table 5.12 Parameters of artificial seismic excitation time history in slope shaking table test 131

Table 5.13 Scheme for ground motion time history spectrum of the slope 133

Chapter 1

Introduction



Abstract How to evaluate the geological hazards triggered by earthquakes has always been the top priority in the study of seismic engineering geology. This chapter introduces the main methods of seismic design and evaluation in slope engineering, including the latest progress of slope seismic reliability, and reviews the main dynamic analysis methods and the currently developed random factors to hope that through the above introduction, readers of this book can better understand the main framework of this book and the main content to be covered in the subsequent chapters.

Keywords Earthquakes · Slope seismic reliability · Impact factors

1.1 Background

Earthquakes are a natural disaster that can cause serious human and infrastructural losses, and are characterized by their suddenness and wide distribution worldwide. Nearly one-third of the largest historic earthquakes occurred from 2000 to 2020 (Hayes et al., 2020).

Earthquakes can trigger a variety of devastating secondary disasters related to major soil deformation and flow, such as soil liquefaction, landslides, and debris flows. Large seismic-induced deformation and flow disasters are typically characterized by their rapid occurrence, widespread range, and strong disaster-causing ability. Natural soil structures can be easily destroyed to form complex flow characteristics, which makes it difficult to control their movement and deformation, thus resulting in large-scale infrastructural damage, heavy casualties, economic losses, and serious social impacts.

For example, damage owing to landslides triggered by the 1984 Alaska earthquake accounted for more than 50% of the total losses (Keefer, 1984). Numerous landslides were triggered by the Loma Prieta earthquake within a sphere of approximately 15,000 km² in California (Keefer, 2000), and more than 200 homes and many roads were destroyed, resulting in approximately \$30 million in property damage. More than 10,000 landslide disasters occurred after the 1999 Chi-Chi earthquake within a distance of nearly 11,000 km² to the high and steep mountainous areas in central

Taiwan (Hung, 2000). The 2005 Pakistan earthquake directly caused more than 2,400 landslides within a sphere of 128 km², leading to more than 1000 deaths and massive property losses (Dunning et al., 2007; Sato et al., 2007). The Wenchuan earthquake in China triggered approximately 15,000 landslides, collapses, and mudslides and other geological disasters, resulting in the death of approximately 20,000 people (Yin et al., 2009).

In view of these tremendous hazards, slope seismic response evaluations and safety assessments are of great significance in the fields of slope stability and geological disaster prevention, and are a key research direction for the future. Reasonable earthquake excitation predictions, slope material constitutive descriptions, and high-precision seismic dynamic response analysis methods are required to accurately understand the slope seismic dynamic response for seismic design and performance evaluation purposes, which form the basis of slope engineering.

1.2 Slope Seismic Dynamic Response Analysis Methods

Earthquake excitations are an important factor that can induce slope instability, and the resulting losses are typically high. The comprehensive analysis of slope stability is therefore especially important to mitigate losses caused by seismic geological hazards. Two types of quantitative slope seismic dynamic analysis methods have been well developed: (1) deterministic seismic dynamic analysis methods; and (2) stochastic seismic dynamic analysis methods, which are introduced in the following two subsections.

1.2.1 *Deterministic Slope Seismic Dynamic Response Analysis Methods*

The deterministic seismic analysis methods that have been developed mainly include: the pseudo-static method; the nonlinear dynamic time-history analysis method; the Newmark sliding block displacement method; and the physical experiment method.

(1) Pseudo-static method

Slope stability analysis is a classic problem in soil mechanics that has undergone long-term development, and uses the factor of safety as the stability evaluation index.

The limit equilibrium method is a common evaluation approach that applies the Mohr–Coulomb model as the strength failure criterion, assumes that soil materials only transmit force without deformation, and determines the reaction force of the sliding surface under static balance conditions to then calculate the slope safety factor. Limit equilibrium methods often introduce some simplifying assumptions to avoid solving statically indeterminate problems by transforming the problem into statically

indeterminate solvable problems. Several limit equilibrium calculation methods have been used to assess slope overall stability. Improvements to limit equilibrium analysis have mainly included the simplification or hypothetical treatment of unknowns in the balance equation of the slice method using the Bishop, Janbu, Morgenstern and Price, or Spence slice methods, which differ only slightly in their solution of static problems (Griffiths & Lane, 1999; Zhang, 1999).

The pseudo-static method was developed based on dynamic time-history analysis, where the equivalent inertial body force is regarded as a simplified form of the seismic load applied to the slope model. The safety factor is calculated using the limit equilibrium method for slope safety assessment.

The ratio of the designed ground motion acceleration to the gravitational acceleration is called the seismic coefficient, which is an important parameter in the pseudo-static method. Extensive research has been performed to determine a reasonable value for the seismic coefficient. Terzaghi (1950) proposed specified values of 0.1, 0.2, and 0.5 to represent severe, destructive, and catastrophic earthquakes, respectively in the pseudo-static method. Seed (1979) analyzed the quasi-static design criteria of 14 dams in 10 seismically active countries using the pseudo-static method, and summarized that 13%–20% of the peak acceleration should be taken as the design seismic acceleration. Marcuson (1981) suggested the design seismic acceleration of dams should be taken as 1/2–1/3 of the peak acceleration, whereas Kramer (1996) proposed that 1/2 was reasonable for the aseismic design of most slopes.

The pseudo-static analysis method is simple in principle, easy to execute, convenient in calculation, and can realize the overall dynamic stability analysis of a slope in a relatively short time. This approach has therefore frequently been used in theoretical analysis and engineering practices of slope dynamic analysis. However, this method converts seismic time histories into equivalent static forces for analysis, which ignores the time effect of seismic excitations.

(2) Newmark sliding block displacement method

Owing to its shortcomings, the pseudo-static analysis method can be difficult to completely realize the dynamic analysis and performance evaluation of slopes during strong earthquake processes. To overcome this limitation, Newmark (1965) proposed the sliding block displacement method.

The Newmark sliding block displacement method is a slope stability evaluation method based on earthquake permanent displacement. This method assumes that even if the slope safety factor is temporarily less than 1 during the earthquake process, it will not necessarily lead to slope failure, but only a certain amount of slope permanent displacement. In this case, the evaluation of slope dynamic stability no longer depends on the minimum safety factor, but rather on the permanent displacement accumulated during the earthquake, which can be obtained by calculating the acceleration integral when the safety factor is less than 1.

This method assumes that the slider is completely rigid, and considers an ideal plastic behavior relationship between the slider and sliding surface, which is referred to as the Newmark rigid slider method. However, deformation of the slider itself on the permanent displacement is not considered. Many scholars have thus improved

this aspect, including the decoupled earthquake permanent displacement method (Makdisi & Seed, 1978; Bray & Rathje, 1998) and the coupled earthquake permanent displacement method (Macedo et al., 2018; Wartman et al., 2003).

The decoupled earthquake permanent displacement method incorporates numerical methods (e.g., finite element) to perform dynamic analysis and failure surface tracking. The permanent displacement is then calculated using the stress field obtained from the seismic dynamic analysis, which accounts for the influence of the seismic dynamic response results. Because dynamic response analysis and sliding analysis are performed separately and in an orderly manner, this method is referred to as a decoupled analysis method. For example, Bray and Rathje (1998) combined the Newmark rigid slider method with fully nonlinear seismic dynamic response analysis to analyze seismic-triggered landfill instability.

The coupled earthquake permanent displacement method is more reasonable yet relatively complicated. The dynamic response analysis and permanent displacement calculation of a sliding body are coupled, thus it not only considers the impact of the seismic response on permanent displacement but also the impact of plastic deformation on the slope seismic dynamic response.

In this approach, the time-domain characteristics of earthquakes and nonlinear characteristics of soils are partially considered using the permanent seismic displacement to evaluate the overall seismic performance or failure state of slopes and supporting structures, which is generally more intuitive, reliable, and reasonable than a safety factor index. However, this method assumes that slope soils lie within a rigid plastic body during earthquake activity and that the soil strength is not significantly reduced, both of which are incompatible with the actual soil state. The overall dynamic behavior of a slope affected by earthquake activity is therefore not truly reflected. A considerable range of different threshold selections used to identify slope instability owing to a lack of uniform standards can also exist.

In summary, for seismic dynamic stability assessment of slope, Newmark sliding block displacement method can overcome the limitations of pseudo-static analysis in the definition of seismic excitations. This method takes the seismic force as a short-term changing direction load, accounts for slope deformation caused by seismic shaking, and proposes the concepts of yield acceleration and cumulative displacement, all of which promote the development of slope dynamic stability analysis methods under seismic loads.

(3) Nonlinear seismic dynamic time history analysis

Compared with the pseudo-static and Newmark sliding block displacement methods, the nonlinear dynamic time history analysis method can be used to embed different constitutive models to reasonably characterize the deformation behavior of rock-soil mass and slope supporting structures under earthquake events and other loads, to evaluate the seismic dynamic response information of slopes. In the nonlinear analysis process, seismic excitations are input in the form of seismic accelerations, velocities, or displacement time histories, which better reflect the effect of earthquake duration on the slope system. The nonlinear dynamic time history analysis method is also more accurate, convenient, and efficient than the previously mentioned methods.

It can simulate the spatial variability of rock and soil materials and consider elastic-plastic characteristics and pore water effects to a certain extent, and has thus become an important tool for slope dynamic response and stability analysis. Several numerical simulation methods have been applied to the nonlinear dynamic analysis of slope engineering. For example, commercial software (e.g., ABAQUS, FLAC3D, Geo-studio) can be used to conduct slope dynamic time history stability analysis based on continuum mechanics. Discontinuous deformation analysis (DDA), universal distinct element code, and particle flow code (PFC) can be used for non-continuum mechanics analysis and other purposes.

a. Slope dynamic time history analysis based on continuum mechanics

The advantage of slope dynamic time history analysis based on continuum mechanics lies in the analysis of the dynamic response and failure surface formation process. For example, FLAC3D was used to calculate dynamic deformation to analyze the seismic instability process of the Wangjiayan landslide (Yin et al., 2015), analyze the seismic displacement of an associated dam (Liu et al., 2016), and investigate the historical stress state of each element by obtaining the dynamic penetration process of the slope plastic zone (Wang et al., 2010). Similar research using Geo-studio software has also been applied to carry out dynamic finite element calculations of seismic amplification effects (Zhao et al. 2015a).

b. Slope dynamic time history analysis based on non-continuum mechanics

Dynamic time history analysis based on non-continuum mechanics can be used in the initiation, movement, and accumulation process of seismic-induced landslides. For example, DDA can be used to study the initiation and movement process of landslides induced by seismic activity. Zhang et al. (2013, 2015) pointed out that seismic activity, especially vertical activity, induced the Donghekou and Daguangbao landslides, and had a strong influence on the initial and movement stages of the landslide disaster. Other particle flow analysis methods can also be used to analyze the movement process of seismic-induced landslides by applying the seismic acceleration or velocity time histories as boundary conditions. For example, Tang et al. (2009) used the seismic information of the Chi-Chi earthquake CHY080 station to study the Tsaoling landslide by the program PFC2D and reported a maximum landslide velocity of 50 m/s due to seismic excitations.

(4) Physical experiment method

The use of physical model experiments (e.g., centrifugal tests, 1 g shaking table tests) is becoming increasingly common in the field of seismic stability and the overall performance analysis of slopes and supporting structures. Physical model experiments, such as shaking table tests, can be used to verify the accuracy and effectiveness of slope supporting structure seismic design theory at relatively low cost and with repeatable observations. The complex mechanisms of earthquake-induced landslides can also be solved using shaking table tests by investigating actual seismic damage phenomena or analyzing seismic measured data, using concrete or generalized slope models to determine the seismic dynamic response laws by considering seismic

factors that influence the slope stability. Numerous studies have performed shaking table tests, the existing shaking table test literature is thus thoroughly presented herein.

The first slope shaking table test recognized by the academic community was successfully carried out by (Clough & Pirtz, 1956). This new method is of far-reaching significance to seismic-related research in engineering geology and geotechnical engineering (Fan et al., 2016; Wartman et al., 2005). In recent decades, the overall bearing capacity of shaking tables has gradually increased and the experimental model size has also correspondingly increased to better simulate the prototype size. The development of large-scale shaking table tests is very helpful to further study the dynamic response behavior of slopes. A large number of shaking table tests are introduced and summarized in this section. Tests regarding slope model response have mainly concentrated on seismic related factors, such as amplitude and frequency characteristics, slope structure, rock mass structure, seismic design measures, and related reinforcement measures.

The acceleration response is an important aspect of slope dynamic response research. The magnification effect of the stochastic dynamic response of a slope with increasing elevation cannot be ignored, especially that of the horizontal seismic component (Zhang et al., 2017). However, ground motion in other directions also has a certain impact on the slope dynamic response. The vertical acceleration amplification factor has been shown to increase when a horizontal wave is simultaneously applied (Liu et al., 2013). Ground motion therefore affects the slope dynamic response, and provides helpful information to further track the slope seismic dynamic response laws.

Slope acceleration amplification owing to topography has been confirmed by actual earthquake observations (Harp & Jibson, 2002; Sepúlveda et al., 2005). The amplification of four-sided slopes has been shown to be the largest in response to seismic acceleration, followed by two-sided slopes and lastly single-sided slopes (Yang et al., 2015). Slope lithology also has an impact. The relationship between the acceleration amplification effect and slope lithology (soft versus hard rock) is variable. For example, Liu et al. (2014b) studied the shaking table test results of measured waves with respect to the Wenchuan earthquake and found that the horizontal acceleration magnification factor of soft rock is larger than that of hard rock. The slope structure also affects the acceleration response of a slope. For example, the amplification effect of a layered slope is greater than that of a homogeneous slope (Liu et al., 2014b) possibly because of the reflection and refraction of the structure facing the seismic wave, which enhances the slope dynamic response (Dong et al., 2011). Topography, slope lithology, and slope structure therefore exert a certain degree of influence on the slope acceleration amplification effect. The amplification effect itself affects the slope stability, thus influencing the slope seismic dynamic response.

Shaking table tests can also be applied to better understand the physical mechanism of slopes by supplying a better reference basis for slope seismic performance design (e.g., slope support structure and reinforcement research). For example, in the case of the Northridge earthquake, studies have shown that retaining walls and

reinforced soils have good seismic performance (Sandri, 1997), whereas the Jiji earthquake led to the damage of slope support structures (Ling et al., 2001). Experiments have shown that the natural frequency of slope itself significantly decreases under earthquake action, the final basic frequency may be only approximately half of the initial model value (Fan et al., 2016; Liu et al., 2013), and the damping ratio is enhanced. Some previous studies have therefore proposed a reinforcement mechanism in which vibration causes the model stiffness to decrease, whereas reinforcement increases the stiffness, which drives the higher natural frequency of the slope itself (Lin et al., 2015). In general, more reinforcement measures are more likely to be associated with a greater increase in natural frequency. Reinforcement not only changes the slope frequency but also alters the failure surface location, thus resulting in different failure modes (Hong et al., 2005). Furthermore, although reinforced slopes still have a certain degree of amplification effect, the overall slope performance can also be satisfactory (Huang et al., 2010). Reinforcing only 1/5 of a dam top can also significantly enhance the overall dam stability (Liu et al., 2014a).

Most supporting slope model soils have been made of geosynthetic materials and silica sand (i.e., geosynthetic reinforced slopes). Reinforcement methods include piles, soil nails, reinforced retaining walls, and expanded polystyrene (Gao et al., 2017; Hong et al., 2005; Panah et al., 2015; Srilatha et al., 2013; Yang et al., 2017). Hong et al. (2005) carried out shaking table tests on soil–nail-supported slopes and demonstrated the advantage of this support design for improving the seismic performance of steep slopes. For solid slopes, the acceleration magnification factor of horizontal seismic activity is very small, and the maximum possible acceleration is only 1.35 under 0.86 g of shaking, which ensures the slope stability (Ling et al., 2005). Tests have shown that the seismic performance of supported slopes is good (Lin et al., 2015), and various supporting shaking table models have demonstrated a substantial reduction of the acceleration amplification effect and slope displacement (Panah et al., 2015; Srilatha et al., 2013; Yang et al., 2017).

Shaking table tests not only are useful for studying the slope seismic dynamic response (e.g., acceleration response and amplification effect) but also can be applied to study physical failure mechanisms, and are therefore an important experimental research method.

1.2.2 Stochastic Slope Seismic Dynamic Response Analysis Methods

Traditional deterministic differential equations have been widely used in the fields of physics, engineering technology, biology, and economic systems. However, the description of actual problems requires increasingly high accuracy. The influence of random factors in a system can therefore not be ignored, and it is necessary to adjust the analysis of some actual processes from the typical deterministic view to a random view, and from a deterministic system to a random system.

Most of the traditional and existing performance-based seismic evaluation and design methods for slope engineering are based on deterministic theory. However, different uncertainty sources can affect the seismic dynamic performance in the design service period of a slope project, including the spatial uncertainty of geotechnical material property parameters, which are affected by the geological and sedimentary history, the uncertainty of external environment excitations (e.g., earthquakes, rainfall), and slope geometry, size, and structural material uncertainties. The geometry and size of slope models are affected by excavation and weathering. Conventional deterministic analysis and design methods often fail to account for the influence of uncertainties on the seismic performance of slopes.

Different probability analysis methods and reliability theories have recently provided new ideas for quantitatively characterizing these uncertainties and their effects on slope stability and seismic performance. The relatively mature slope reliability analysis methods under earthquake action mainly include: approximate moment methods based on the sampling of several critical moment points (mainly the first-order and second-moment method); Monte Carlo stochastic simulation methods for random sampling in probability space; functional response surface methods for determining complex geotechnical structures; and the pseudo-excitation method (PEM), which is highly efficient and can rapidly solve the response of a linear stochastic dynamical system.

(1) First-order second-moment method.

The basic principle of the first-order second-moment (FOSM) method is to use a Taylor series to expand the functional function at a certain point, take its linear first-order term, and solve the reliability index based on the first second-moment of the random variable (i.e., mean value and variance). This is further divided into the central point method and checking point method according to the different expansion points of the Taylor series.

a. Central point method

The central point method is also known as the mean first-order second-moment (MFOSM) method (Hasofer & Lind, 1974). In this approach, the functional function Z is expanded by a Taylor series at the central point (i.e., mean point) to obtain the first-order term, namely:

$$Z \approx g(\mu_X) + \sum_{i=1}^n \left(\frac{\partial g}{\partial X_i} \right)_{\mu_X} (X_i - \mu_{X_i}) \quad (1.1)$$

where the components of the basic random vector $X = (X_1, X_2, \dots, X_n)^T$ are independent of each other with a mean of $\mu_X = (\mu_{X_1}, \mu_{X_2}, \dots, \mu_{X_n})^T$ and standard deviation of $\sigma_X = (\sigma_{X_1}, \sigma_{X_2}, \dots, \sigma_{X_n})^T$, and $\left(\frac{\partial g}{\partial X_i} \right)_{\mu_X}$ is the derivative of the function at the mean point.

The central point method directly describes the relationship between the statistical parameters of random variables and the reliability index of functional functions. The central point method has a clear concept, simple calculation, and certain practicability. However, this method also has the following drawbacks.

- (1) The central point method is based on the assumption that random variables obey a normal or lognormal distribution, and other probability distributions cannot be directly used.
- (2) The essence of expanding the functional function at the center and taking the first term is the linearization of the limit state function. When the limit state function is nonlinear, the calculation error cannot be ignored.
- (3) For limit state equations of the same mechanical significance but different forms, their reliability indexes are different.

b. Advanced first-order second-moment method

The advanced FOSM method selects the Taylor series expansion point of the functional function on the failure surface and considers the actual distribution type of the basic random variable, which overcomes the above limitations of the central point method (Hasofer & Lind, 1974).

Let us assume that the basic random variable is subject to an independent normal distribution. Expand the functional function at the point in accordance with the Taylor series $x^* = (x_1^*, x_2^*, \dots, x_n^*)^T$ and take the first-order term:

$$Z \approx g(x^*) + \sum_{i=1}^n \left(\frac{\partial g}{\partial X_i} \right)_{x^*} (X_i - x_i^*) \quad (1.2)$$

Equation (1.2) corresponds to the tangent plane of the limit state surface at the crossing point x^* in the space of random variable X . The point y^* in the space of the standard normal random variable Y corresponding to the point x^* in the space of the random variable X is called the checking point.

The iterative algorithm is usually applied to solve the checking points and their corresponding reliability indexes. The specific steps are as follows.

- (1) Assume that the initial value of x^* is generally the mean value point.
- (2) Insert the initial value of x^* into Eq. 1.2 and calculate α_{X_i} and β in turn.
- (3) Use the calculated value of β to obtain the new x^* .
- (4) Repeat the above steps until the error on x^* before and after is less than the accuracy requirement.

Rüdiger and Bernd (1978) proposed a method based on equivalent normalization to include the non-normal distribution of random variables. The basic idea is to normalize the equivalent variable of the non-normal distribution, and then calculate the reliability index based on the mean value and variance of the equivalent normalized variable. According to the conditions of equivalent normalization, at checking point x_i^* , the cumulative distribution function and probability density function of the

equivalent normalized variable and original non-normal distributed variables should be equal, respectively.

The actual distribution of random variables is considered in the checking point method, and the expansion points are located on the limit state plane. The calculation accuracy is thus higher than that of the center point method. However, the essence of this approach still involves the linear approximation of the limit state equation (i.e., taking the first-order term), and the calculation error is large when the degree of nonlinearization of the functional function is high.

Although a second-order reliability method (SORM) has been developed by some scholars based on the FOSM method, it is seldom used in engineering because of the calculation complexity. Furthermore, the most fundamental defect of the approximate moment method represented by the FOSM method is that the probability density function of the system response cannot be obtained, rather only the finite order statistical moment of the functional function. It is therefore impossible to accurately grasp the evolution of the probability density of the system at the probability density level.

(2) Monte Carlo simulation method

Although several methods have been applied to problems with uncertain parameters described by the stochastic process, the Monte Carlo simulation (MCS) method is generally accepted as the only accurate method with universality, and thus is commonly applied to uncertainty stochastic mechanics problems with any dimensions of nonlinearity, randomness, stochastic stability, parametric excitation, and/or variability.

The MCS method (also known as the stochastic simulation method) is a numerical analysis method based on statistical sampling theory that uses a computer to study random variables. The MCS method is a widely used and relatively accurate approach in reliability analysis, and is the only method for testing the accuracy of other reliability methods in some cases (Schueller, 1997, 2006) (e.g., perturbation, statistical linearization, and random average methods).

Many scholars have performed Monte Carlo stochastic simulations to address geological engineering problems. For example, Monte Carlo stochastic simulations have been applied to evaluate the seismic performance and aseismic reliability of a slope after reinforcement considering the uncertainty of slope rock mass parameters (e.g., internal friction angle, yield strength, and rigidity of the reinforced material) and deterministic seismic input. Monte Carlo stochastic simulation analysis has also been used to obtain the power spectral density function of the slope seismic response (e.g., slope displacement, stress) considering both the randomness of ground motion and uncertainty of the rock and soil mass parameters, and the slope seismic reliability has been investigated based on the first pass failure theory (Hayashi & Tang, 1994).

On the basis of the modal perturbation analysis method, Pan and Lou (2008) assumed that the stratified earth is equivalent to a uniform shear beam and bedrock ground motion is a stationary stochastic process with the mean value of zero. They inputted the corresponding power spectral density function, obtained the corresponding modal and frequency based on the frequency domain analysis method,

transferred the differential equations that describe the stochastic response of stratified earth into an algebraic equation, and proposed the approximate analysis method.

$$Z = g(R, Q) = g(\mathbf{X}) = F_s(\mathbf{X}) - 1 \quad (1.3)$$

where, \mathbf{X} is a random vector, F_s is the expression of slope stability by safety factor, Q is the load, R is resistance, Z is the functional function of slope stability, and $g(\cdot)$ is the functional function characterized by resistance and external excitations.

With reference to the definition of frequency, MCS can be performed to determine the failure probability. After determining the basic probability distribution of random variables (e.g., slope geotechnical mechanics parameters, load) according to the functional Eq. (1.3), the random sampling method can be used to produce a set of random vectors that conform to the distribution of the random variables. The generated result is substituted into the functional equation to calculate a response value of the functional equation. In the same way, N sample response values can be generated. According to the large number theorem, If the number of sample responses less than zero (i.e., failure zone) is M , when the sampling times N is sufficiently large, the probability can be approximately estimated by the frequency as follows.

$$\hat{P}_f = P(Z < 0) = \frac{M}{N} \quad (1.4)$$

where \hat{P}_f represents the estimated value of the failure probability P_f . The mean value and standard deviation of the functional function Z can be further calculated according to the N calculated values of the functional functions, and its probability distribution function can be fitted.

Random sampling is the basis of the MCS method and is also the key to determine the computational efficiency. There are many sampling methods to improve computational efficiency, such as importance sampling, Latin hypercube sampling, and direction sampling. Latin hypercube sampling is a multi-dimensional stratified sampling technique that is widely used in slope reliability analysis because of its advantages of high sampling efficiency and good sampling effects (Li et al., 2013). The Latin hypercube sampling method evenly divides the value range of the probability distribution function of basic random variables X_i into N sections. The inverse function of the probability distribution is then used to obtain N equal probability intervals of the domain of the basic random variable X_i , and select one point from every equal probability interval, which are composed of N sample values of the basic random variables X_i (Olsson & Sandberg, 2002).

The calculation accuracy of the MCS method is only related to the number of samples, and insensitive to the number of random variables. According to the principle of mathematical statistics, the coefficient of variation of the failure probability estimate \hat{P}_f can be expressed as:

$$\delta_{\hat{P}_f} \approx \sqrt{\frac{(1 - \hat{P}_f)}{N \hat{P}_f}} \quad (1.5)$$

It is easy to show from Eq. (1.5) that under the specific calculation accuracy requirements, the number of samples required by the stochastic simulations rapidly increases with decreasing failure probability, which leads to a large calculation amount. For example, when $\hat{P}_f = 10^{-4}$ and $\delta_{\hat{P}_f} = 0.1$, the number of required simulations N is 10^6 .

It is generally believed that the biggest advantage of the Monte Carlo stochastic simulation method is that it offers sufficient accuracy for any dimension of a random problem. The only disadvantage is the very large calculation cost and machine capacity consumption. The large amount of required computing power to accurately estimate the failure probability has thus become the bottleneck that restricts the method from practical application, especially for functions without an analytic expression and a relatively small failure probability.

The theoretical basis of the Monte Carlo stochastic simulation method also follows the law of large numbers, and the calculation results should be a random variable. The method to develop the calculation accuracy of MCS is therefore to control the simulation variance. Notably, a variance, instead of truncation errors, exists, which also leaves the MCS method with an innate defect, namely random convergence problems. Some studies have shown that even if the variance of Monte Carlo random simulations is less than 5%, the accuracy of the calculation results cannot be guaranteed to be less than 5% (Engelund & Rackwitz, 1993).

a. Response surface method

The response surface method (RSM) was first proposed by mathematicians Box and Wilson in 1951 (Box & Wilson, 1951). The basic idea is to approximately construct a functional function that contains some unknown parameters to replace the implicit functional function. This approximate functional function is called the response surface function.

Under the premise to fulfill both the calculation accuracy and efficiency requirements, a quadratic polynomial without cross terms is typically adopted as the response surface function for a function containing n random variables $Z = g(X_1, X_2, \dots, X_n)$, namely:

$$\tilde{Z} = a + \sum_{i=1}^n b_i x_i + \sum_{i=1}^n c_i x_i^2 \quad (1.6)$$

where a , b_i , and c_i are undetermined coefficients with totally $2n + 1$ numbers. The specific method is as follows.

- (1) Obtain $2n + 1$ sampling points according to the sampling point design.
- (2) Use the deterministic method to calculate the slope stability $2n + 1$ times. The deterministic method can be a simple limit equilibrium method or mature numerical methods.
- (3) Substitute the sampling points and their corresponding response values into Eq. (1.6) and use the least square method to determine the undetermined coefficient.
- (4) After determining the approximate explicit expression of the functional function, the FOSM or MCS method can be used to calculate the failure probability and reliability indexes of the slope.

b. Pseudo-excitation method

The pseudo-excitation method (PEM) was proposed by Lin and Zhang (2004), and is very efficient and precise for determining the stable response of linear stochastic systems. It is also an important method for complete quadratic combination in seismic design code for building construction as well as the square root of the sum of squares, which provide a complete theoretical basis. This section briefly introduces the basic theory of the PEM for linear stationary stochastic systems, and analyzes its application in the analysis of the linear stationary random seismic response of a slope. This method greatly reduces the calculation of linear stochastic dynamical systems, and thus makes it possible to design and evaluate large complex structures based on stochastic vibration theory.

The following is divided into two types of PEM: stationary random response and non-stationary random response. For a linear stationary stochastic system, when a single-point excitation is received, the power spectral density (PSD) function of excitation $X(t)$ is assumed to be $S_{XX}(\omega)$, and the self-power spectral density function of response y is $S_{YY}(\omega)$:

$$S_{YY}(\omega) = |H|^2 S_{XX}(\omega) \quad (1.7)$$

where H is based on the frequency response function of the frequency domain analysis method. If the single-point random excitation is the unit harmonic excitation $\exp(i\omega t)$, the corresponding harmonic response is $y = H \exp(i\omega t)$.

If the excitation is assumed to be the product of constant $\sqrt{S_{xx}}$ and $\exp(i\omega t)$, the following virtual excitation can be constructed, where $\tilde{x}(t)$ is $\sqrt{S_{xx}} e^{i\omega t}$.

$$(a) S_{xx} \Rightarrow H(\omega) \Rightarrow S_{yy} = |H|^2 S_{xx} \quad (1.8)$$

$$(b) x = \exp(i\omega t) \Rightarrow H(\omega) \Rightarrow y = H e^{i\omega t} \quad (1.9)$$

$$(c) \tilde{x} = \sqrt{(S_{xx})} e^{i\omega t} \Rightarrow H(\omega) \Rightarrow S_{yy} = H^2 S_{xx} \quad (1.10)$$

$$(d)\tilde{x} = \sqrt{(S_{xx})}e^{i\omega t} \Rightarrow H(\omega) \Rightarrow \begin{cases} \tilde{y}_1 = \sqrt{(S_{xx})}H_1e^{i\omega t} \\ \tilde{y}_2 = \sqrt{(S_{xx})}H_2e^{i\omega t} \end{cases} \quad (1.11)$$

$$\tilde{x}(t) = \sqrt{(S_{xx})}e^{i\omega t} \quad (1.12)$$

In the stochastic seismic response analysis of engineering structures, we are concerned with quantities such as the displacement structure U , internal force F , stress σ , and strain response ε , among others. According to the PEM and Eq. (1.12), \tilde{U} , \tilde{F} , $\tilde{\sigma}$, and $\tilde{\varepsilon}$ are the responses to the amount of virtual response, and can be directly obtained from the PSD or mutual power spectral density of the physical quantity of interest.

The PEM can very conveniently obtain the PSD function of the structural response, and the formulas for calculating the self-power spectrum and cross-power spectrum of the response are simple and unified. It should be emphasized that as long as the relationship between the excitation and response can be described by a linear random frequency response function, the random response solution of the structure can be solved using the PEM. In the calculation process of the self-power spectrum and cross-power spectral density function, the virtual external excitation $\exp(i\omega t)$ and its complex conjugate always appear in pairs and their product cancels each other. This characteristic indicates that the self-power spectrum and mutual PSD function of the stationary random excitation response are time-invariant. The PEM can similarly be used to obtain the self-power spectrum and cross-power spectral density functions of each order of the stationary random process.

It is unreasonable to assume a stationary excitation because there are notable intensity variations and stationary and attenuation periods during a given loading period, such as earthquakes, explosions, and gusts. With the construction of long flexible structures in recent years (e.g., long bridge structures, large buildings, and high dams), the natural vibration period of some engineering structures can reach more than 10 s or even longer than 20 s because the displacement of long-period structures is mainly controlled by transient vibrations. The displacement of a long-period structure may occur not only at the resonance time of the structure, but also after the disappearance of the external excitation.

According to Yeh and Wen (1990), the influence of non-stationary characteristics of ground motion on engineering structures is mainly concentrated on structures with stiffness and strength degradation. Li et al. (2016) showed that a structure's period is longer after earthquake-induced damage. If the natural vibration frequency of the damaged structure is similar to the ground motion frequency after the strong earthquake, the seismic response of the structure will be large or even exceed the damage caused by the strong earthquake. The reason is that such structures have accumulated a considerable amount of damage, and this scenario is called the "instantaneous resonance". The non-stationary characteristics of ground motion are therefore particularly important for the seismic response of engineering structures, especially long-period flexible structures.

Numerous studies have addressed non-stationary random processes (Douglas & Edwards, 2016). In the field of earthquake engineering, the evolutionary power spectrum model proposed by (Priestley, 1967) has attracted substantial research attention. On the basis of the Priestley power spectrum model, this kind of non-stationary random vibration process with an evolving power spectral density function can be represented by the Riemann–Stieltjes integral:

$$X(t) = \int_{-\infty}^{+\infty} A(\omega, t) \exp(i\omega t) d\alpha(\omega) \quad (1.13)$$

This represents a non-uniformly modulated evolutionary random ground motion process. Solving the random seismic response of engineering structures excited by non-stationary random earthquakes can be very difficult. The approximate method is generally adopted, and the non-stationary characteristics of the intensity-frequency energy distribution with non-stationary random excitation frequency are ignored. This can thus be simplified to stationary random excitation. Although this simplification is unreasonable and it is difficult to accurately grasp the precise response of engineering structures under earthquake action, even the simplification is quite difficult to calculate for actual engineering (Schuellër, 1997).

The ultimate goal of the PEM is to solve the dynamic system response with the PSD level, whether linear or nonlinear. However, a slope under dynamic seismic conditions represents a nonlinear stochastic dynamic system owing to the strong nonlinear dynamic behavior of the slope soil material. Calculating the dynamic reliability of a slope under earthquake action by only obtaining a solution for the power spectral density hierarchy is therefore quite difficult. As a result, it is challenging to obtain the stochastic seismic response and reliable seismic slope analysis of a slope under earthquake action using the PEM.

1.3 Limitations and Deficiencies of Existing Methods

The previous section briefly introduced the existing slope seismic dynamic stability analysis methods. However, these methods still face certain limitations, and the uncertainties involved in slope engineering continue to lack complete and comprehensive consideration. There are several uncertain factors that require additional study in slope engineering. For example, seismic excitation randomness is complex and remain poorly understood. Housner (1947) first regarded ground motion as a stochastic process. Furthermore, geotechnical materials are often affected by geological conditions and human activities. The physical and mechanical parameters of slope soil materials thus present spatial uncertainties.

The randomness of seismic excitations and geotechnical material uncertainties constitute the main sources of uncertainties in slope systems. To accurately grasp the

slope seismic dynamic response, the potential uncertainties of slope dynamic analysis must be discussed in terms of the slope stochastic seismic dynamic response and seismic stability from a stochastic perspective (Al-Homoud & Tahtamoni, 2001, 2002; Shinoda et al., 2006; Tsompanakis et al., 2010). Studies regarding the uncertainties in slope engineering are discussed in the following subsections.

1.3.1 Spatial Variability of Rock and Soil Parameters

The key to slope seismic performance and safety evaluation is to accurately grasp and evaluate the deformation characteristics and seismic stability of the slope under possible future earthquake conditions at an engineering site. In dynamic time history analysis, an approach to select the appropriate dynamic constitutive models and corresponding parameter calibration are the two major bottlenecks that restrict geotechnical engineering.

The rock-soil materials that make up a slope are also generally highly nonlinear materials that assume various deformation characteristics under different forces. Rock-soil materials are highly sensitive to ground motion, and slopes tend to have very different seismic dynamic responses under different earthquake conditions. The seismic dynamic response of a slope exhibits considerable variability owing to the randomness of the rock and soil parameters even for the same ground motion because of the sensitivity differences of the non-linear part of the rock and soil parameters to seismicity.

Crawford and Eden (1967) first regarded soil parameters as variables, and pioneered the use of the reliability method to obtain probabilistic information of slope stability. This set off an upsurge in reliability research regarding the spatial differences of rock and soil materials. Related research considering the uncertainty of geotechnical materials is herein roughly divided into slope reliability analysis based on the random variable model and random field model according to different spatial variability models of rock and soil materials.

The random variable model regards the physical or mechanical parameters of rock or soil as random variables that obey a certain probability distribution. The quantitative description of the uncertainty of rock and soil parameters in this approach uses a marginal probability distribution function (single variable) or joint probability distribution function (multivariate).

Some research regarding slope reliability analysis is summarized here. Malkawi et al. (2000) regarded the soil cohesion, internal friction angle, gravity, and other parameters as random variables, and used the FOSM and MCS methods to compare and analyze the reliability of homogeneous and nonhomogeneous soil slopes. Dodagoudar and Venkatachalam (2000) introduced fuzzy sets based on random variable models to further consider the ambiguity of soil parameters, and proposed the fuzzy point estimate method (FPEM), which they applied to a double-layer soil slope. Tan et al. (2003) later improved the FPEM, and Giasi et al. (2003) put forward a FOSM method that considers the randomness and ambiguity of soil parameters.

According to the graphical meaning of the reliability index, Low and Tang (2007) regarded the relevant soil parameters as random variables, and proposed a slope reliability analysis data table method by using a first order reliability method (FORM) in Microsoft Excel. Low et al. (2011) further developed this reliability calculation method within the data table method for the SORM, and calculated the system reliability of slopes with retaining walls. Tan and Wang (2009) considered the uncertainties of soil mechanical parameters and used the FOSM method based on the nonlinear finite element method to obtain the slope system reliability. With the aim to reduce the amount of calculation required for MCS in cases of low failure probability, Johari and Javadi (2012) evaluated the reliability of infinite slopes using the joint distributed random variable method. Development of artificial intelligence and machine learning methods has led many scholars to begin using genetic algorithms (Xue & Gavin, 2007), support vector machines (Chen et al., 2011; Zhao, 2008), artificial neural networks (Cho, 2009), particle swarm optimization (Taha et al., 2012), and other advanced algorithms, which have been introduced into the field of slope reliability analysis to improve the reliability calculation efficiency.

Babu and Murthy (2003) evaluated the dynamic reliability of slopes by introducing an amplification factor and peak acceleration based on the random variable description of soil parameters. Peng et al. (2005) combined the FOSM method, quasi-static method, and artificial neural network algorithm, and proposed a slope seismic reliability calculation method that considers the randomness of soil parameters. Shinoda et al. (2006) proposed a new MCS method with low deviation and combined the Newmark sliding block displacement method to study the slope dynamic reliability with reinforced measures.

Notably, in the random variable model, the geotechnical materials are regarded as a homogeneous material. This assumes that the parameter values at each point in the space are exactly the same, and the stochastic characteristics of the rock and soil materials are only shown for the values of different samples generated in the random variable model. However, the material properties of even homogeneous rock and soil often exhibit certain spatial variability and stratification owing to geological processes, natural conditions, human activities, and other factors (Vanmarcke, 1977). The random field model was developed to describe the internal characteristics and spatial variability of geotechnical materials. It is believed that for the random field model, the physical and mechanical parameters of rock and soil materials differ at different positions in space and have a certain correlation with each other. This correlation is usually described by indicators such as the correlation distance, correlation function, and variance reduction function. Research related to slope reliability analysis based on random field theory has been gradually carried out.

For example, Li and Lumb (1987) used the FOSM method to analyze the influence of relative distance on the slope reliability index. Auvinet and Gonzalez (2000) studied reliability of a three-dimensional cohesive slope and analyzed the influence of the mean value, variance, and correlation distance of soil parameters on the failure mechanism and its corresponding reliability index. Hicks and Samy (2004) simulated the variability of anisotropic undrained shear strength, achieved the generation of a random field, and combined with the MCS method to analyze its influence on

the reliability of heterogeneous slopes. Griffiths et al. (2004, 2009a) proposed the random finite element method (RFEM) based on random field theory. This method uses the local averaging method to simulate random fields, and is combined with the elastic–plastic strength reduction method and MCS method to determine the failure probability (Griffiths & Fenton, 2004; Griffiths et al. 2009a). Shortly thereafter, Griffiths et al. (2009b) successfully applied the RFEM to calculate the reliability of three-dimensional soil slopes. Cho (2007, 2010) used the local average method and Karhunen-Loève expansion method to calculate the slope stability probability in combination with the MCS method. Srivastava et al. (2010) combined random field model, finite difference numerical analysis, and MCS method to analyze how the spatial variability of the permeability coefficient affects the slope stability and seepage flow behavior. Wang et al. (2011) improved the calculation efficiency of MCS method in slope reliability analysis by subset simulations, and analyzed how the soil parameters and spatial variability of the critical slip surface affect reliability indicators. Li et al. (2014) obtained the reliability of infinite slopes by analyzing a random field of geotechnical parameters that linearly increase with depth. Jha (2015) successfully compared and analyzed the differences among the FOSM, improved FOSM, and RFEM methods, and suggested the advantage of RFEM in the slope reliability analysis. Kasama and Whittle (2016) regarded undrained shear strength and soil weight as random variables with a lognormal distribution and studied the slope stability by combining Cholesky decomposition with numerical analysis. Michael et al. (2016) generated an anisotropic non-Gaussian random field of shear module using the expansion optimal linear estimation method, and calculated the reliability of slope dynamic response combined FLAC software and MCS method.

1.3.2 Randomness of Seismic Ground Motion

Parameters related to ground motion include frequency, strength, and duration. Actual measured records show that even for the same location, ground motion information is not completely identical, as shown in Fig. 1.1, and has notable randomness, which will affect the slope dynamic stability and make it difficult to accurately command the ground motion information for future events. It is therefore reasonable to regard ground motion as a stochastic process to analyze slope stochastic dynamic stability under stochastic seismic activity.

Hayashi and Ang (1992) considered a sliding block in a single degree of freedom system and analyzed the slope reliability under seismic action using the stochastic vibration theory and first-passage failure theory. Huang and Xiong (2017) analyzed the stochastic dynamic reliability of homogeneous slopes based on the power spectrum probability model using the probability density evolution method.

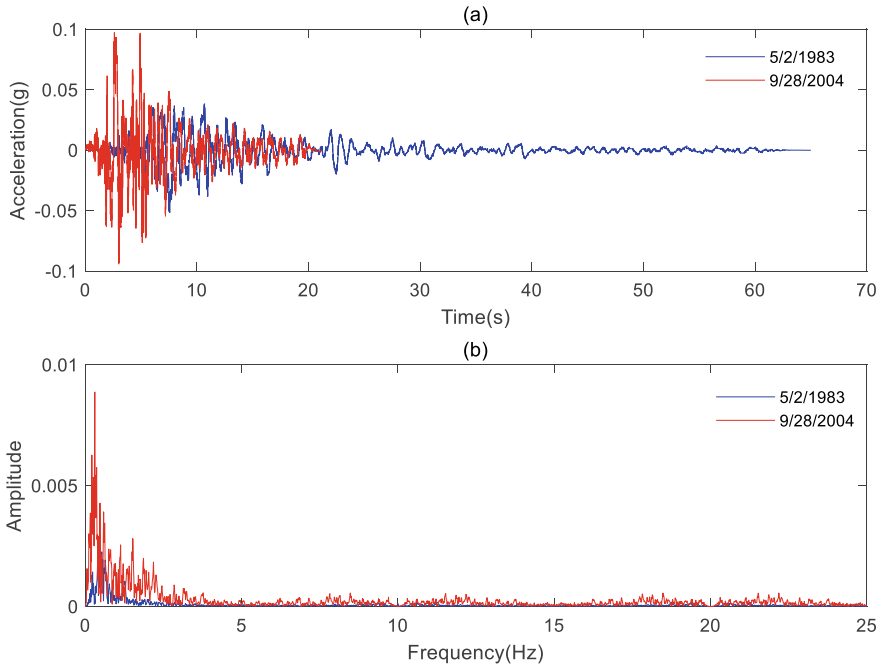


Fig. 1.1 Acceleration (a) and frequency spectrum information (b) of two earthquakes at the same site (data from the PEER database)

1.3.3 Compound Randomness

The slope uncertainty analysis introduced in this book mainly addresses two respects: parameter uncertainty and ground motion randomness. However, the above introduction only includes a single uncertainty factor and lacks a more comprehensive multi-factor discussion. The above two factors should be comprehensively considered in slope uncertainty analysis to fully analyze the uncertain factors in slope systems. The coupling of randomness of rock and soil parameters and ground motions has been the focus of numerous studies. Al-Homoud and Tahtamoni (2000, 2002) considered the above two factors in the analysis of safety factor and permanent displacement, and proposed a three-dimensional model of dynamic reliability analysis. Kim and Sitar (2013) used the stochastic process and random field to describe the stochastic characteristics of ground motions and geotechnical parameters, and combined Newmark sliding block displacement and MCS methods to study the dynamic reliability of slopes.

1.4 Aim of This Book

Upon summarizing the above research, it is clear that slope stability analysis remains an active research hot spot. Especially in slope dynamic analysis, the stochastic dynamic stability of slopes is still in the initial stage. Various simplified analysis methods have to be sought to account for the complexity of dynamic problems. The increased number of dimensions of stochastic variables introduces a geometric increase in the calculation amount. As a result, unsolved problems still exist in slope dynamic reliability research. Comprehensive hazard analysis on slope stochastic dynamic stability problems is therefore necessary to reduce losses and casualties caused by seismic geological disasters.

This book establishes a basic theoretical framework of stochastic dynamic analysis for slope engineering by quantifying uncertain factors in slope engineering stability analysis, and provides a reference for slope risk assessment based on stochastic dynamics. The book outline is introduced here.

In this chapter, the background of this book is introduced in detail, including earthquake and geological disasters that have occurred in recent years, existing slope seismic stability analysis methods, their current advantages and limitations, and uncertainties that are not covered in these evaluation methods. The overarching hope is to establish a new century-breaking slope stochastic dynamics framework.

Chapter 2 pertains to the basic framework and general process of the stochastic dynamic theory of slope engineering. The basic application of the slope stochastic dynamic theoretical framework is introduced by means of slope seismic dynamic nonlinear time history analysis and applied to slope stochastic stability analysis in Chap. 3 as a reference. On the basis of slope instability analysis and numerical simulations, failure mode, failure mechanism, and post-failure behavior analysis of slope after failure based on stochastic dynamics are also important, which will be clearly defined and described in Chap. 4.

The validity and accuracy of the theoretical framework and slope stochastic nonlinear dynamic response law and characteristic are classified using a physical model experiment in Chap. 5. However, considering the limitations of the experiment itself, no experimental discussion is provided here for the study of slopes after failure, which will hopefully be continuously improved in future research.

Chapter 6 summarizes the conclusions of this book and presents future prospects for slope nonlinear stochastic dynamics analysis. For convenience, Fig. 1.2 illustrates the basic contents of this book.

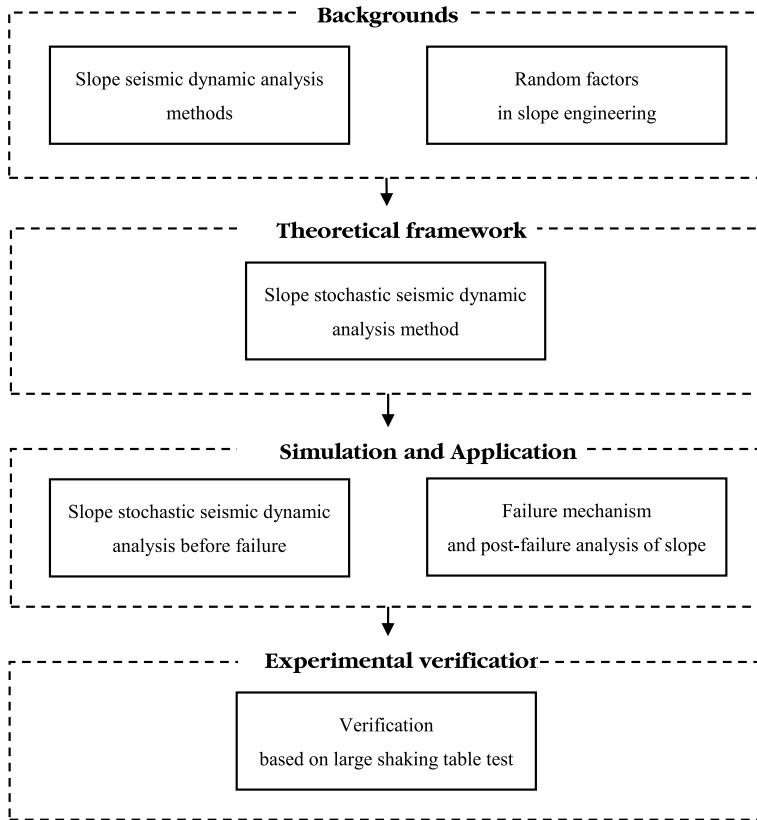


Fig. 1.2 Basic logical framework of this book

References

- Al-Homoud, A. S., & Tahtamoni, W. W. (2000). Reliability analysis of three-dimensional dynamic slope stability and earthquake-induced permanent displacement. *Soil Dynamics and Earthquake Engineering*, 19(2), 91–114.
- Al-Homoud, A. S., & Tahtamoni, W. W. (2001). A reliability based expert system for assessment and mitigation of landslides hazard under seismic loading. *Natural Hazards*, 24(1), 13–51.
- Al-Homoud, A. S., & Tahtamoni, W. W. (2002). Seismic reliability analysis of earth slopes under short term stability conditions. *Geotechnical and Geological Engineering*, 20(3), 201–234.
- Auvinet, G., & Gonzalez, J. (2000). Three-dimensional reliability analysis of earth slopes. *Computers and Geotechnics*, 26(3–4), 247–261.
- Babu, S. G., & Murthy, S. D. (2003). Reliability based seismic stability of soil slopes. *Indian Geotechnical Journal*, 33(3), 233–247.
- Box, G. E. P., & Wilson, K. B. (1951). On the Experimental Attainment of Optimum Conditions. *Journal of the Royal Statistical Society*, 13(1), 1–45.
- Bray, J. D., & Rathje, E. M. (1998). Earthquake-induced displacements of solid-waste landfills. *Journal of Geotechnical and Geoenvironmental Engineering*, 124(3), 242–253.

- Chen, C., Xiao, Z., & Zhang, G. (2011). Time-variant reliability analysis of three-dimensional slopes based on Support Vector Machine method. *Journal of Central South University of Technology*, 18(6), 2108–2114.
- Cho, S. E. (2007). Effects of spatial variability of soil properties on slope stability. *Engineering Geology*, 92(3–4), 97–109.
- Cho, S. E. (2009). Probabilistic stability analyses of slopes using the ANN-based response surface. *Computers and Geotechnics*, 36(5), 787–797.
- Cho, S. E. (2010). Probabilistic assessment of slope stability that considers the spatial variability of soil properties. *Journal of Geotechnical and Geoenvironmental Engineering*, 136(7), 975–984.
- Clough, R. W., & Pirtz, D. (1956). Earthquake resistance of rock-fill dams. *Journal of the Soil Mechanics and Foundations Division*, 82(2), 1–26.
- Crawford, C. B., & Eden, W. J. (1967). Stability of natural slopes in sensitive clay. *Journal of the Soil Mechanics and Foundations Division*, 93(4), 419–436.
- Dodagoudar, G., & Venkatachalam, G. (2000). Reliability analysis of slopes using fuzzy sets theory. *Computers and Geotechnics*, 27(2), 101–115.
- Dong, J., Yang, G., & Wu, F., et al. (2011). The large-scale shaking table test study of dynamic response and failure mode of bedding rock slope under earthquake. *Rock and Soil Mechanics*, 32(10), 2977–2983.
- Douglas, J., & Edwards, B. (2016). Recent and future developments in earthquake ground motion estimation. *Earth-Science Reviews*, 160, 203–219.
- Dunning, S., Mitchell, W., & Rosser, N., et al. (2007). The Hattian Bala rock avalanche and associated landslides triggered by the Kashmir Earthquake of 8 October 2005. *Engineering Geology*, 93(3–4), 130–144.
- Engelund, S., & Rackwitz, R. (1993). A benchmark study on importance sampling techniques in structural reliability. *Structural Safety*, 12(4), 255–276.
- Fan, G., Zhang, J., & Wu, J., et al. (2016). Dynamic response and dynamic failure mode of a weak intercalated rock slope using a shaking table. *Rock Mechanics and Rock Engineering*, 49(8), 3243–3256.
- Gao, H., Hu, Y., & Wang, Z., et al. (2017). Shaking table tests on the seismic performance of a flexible wall retaining EPS composite soil. *Bulletin of Earthquake Engineering*, 15(12), 5481–5510.
- Giasi, C., Masi, P., & Cherubini, C. (2003). Probabilistic and fuzzy reliability analysis of a sample slope near Aliano. *Engineering Geology*, 67(3–4), 391–402.
- Griffiths, D., & Fenton, G. A. (2004). Probabilistic slope stability analysis by finite elements. *Journal of Geotechnical and Geoenvironmental Engineering*, 130(5), 507–518.
- Griffiths, D. V., & Lane, P. A. (1999). Slope stability analysis by finite elements. *Geotechnique*, 49(3), 387–403.
- Griffiths, D., Huang, J., & Fenton, G. A. (2009). On the reliability of earth slopes in three dimensions. *Proceedings of the Royal Society a: Mathematical, Physical and Engineering Sciences*, 465(2110), 3145–3164.
- Griffiths, D., Huang, J., & Fenton, G. A. (2009). Influence of spatial variability on slope reliability using 2-D random fields. *Journal of Geotechnical and Geoenvironmental Engineering*, 135(10), 1367–1378.
- Harp, E. L., & Jibson, R. W. (2002). Anomalous concentrations of seismically triggered rock falls in Pacoima Canyon: Are they caused by highly susceptible slopes or local amplification of seismic shaking? *Bulletin of the Seismological Society of America*, 92(8), 3180–3189.
- Hasofer, A. M., & Lind, N. C. (1974). Exact and invariant second-moment code format. *Journal of the Engineering Mechanics Division*.
- Hayashi, H., & Ang, A. H. S. (1992). Reliability of Cut Slopes Under Seismic Loading. *Soils and Foundations*, 32(2), 45–56.
- Hayashi, H., & Tang, W. H. (1994). Probabilistic evaluation on progressive failure in cut slopes. *Structural Safety*, 14(1–2), 31–46.

- Hayes, G. P., Smoczyk, G. M., & Villaseñor, A. H., et al. (2020). Seismicity of the Earth 1900–2018: U.S. Geological Survey Scientific Investigations Map 3446, scale 1:22,500,000, from <https://doi.org/10.3133/sim3446>.
- Hicks, M. A., & Samy, K. (2004). Stochastic evaluation of heterogeneous slope stability. *Italian Geotechnical Journal*, 38(2), 54–66.
- Hong, Y. S., Chen, R. H., & Wu, C. S., et al. (2005). Shaking table tests and stability analysis of steep nailed slopes. *Canadian Geotechnical Journal*, 42(5), 1264–1279.
- Housner, G. W. (1947). Characteristics of strong-motion earthquakes. *Bulletin of the Seismological Society of America*, 37(1), 19–31.
- Huang, Y., & Xiong, M. (2017). Dynamic reliability analysis of slopes based on the probability density evolution method. *Soil Dynamics and Earthquake Engineering*, 94, 1–6.
- Huang, C. C., Horng, J. C., & Chang, W. J., et al. (2010). Dynamic behavior of reinforced slopes: Horizontal acceleration response. *Geosynthetics International*, 17(4), 207–219.
- Hung, J. J. (2000). Chi-Chi earthquake induced landslides in Taiwan. *Earthquake Engineering and Engineering Seismology*, 2(2), 25–33.
- Jha, S. K. (2015). Effect of spatial variability of soil properties on slope reliability using random finite element and first order second moment methods. *Indian Geotechnical Journal*, 45(2), 145–155.
- Johari, A., & Javadi, A. (2012). Reliability assessment of infinite slope stability using the jointly distributed random variables method. *Scientia Iranica*, 19(3), 423–429.
- Kasama, K., & Whittle, A. J. (2016). Effect of spatial variability on the slope stability using random field numerical limit analyses. *Georisk: Assessment and Management of Risk for Engineered Systems and Geohazards*, 10(1), 42–54.
- Keefer, D. K. (1984). Landslides caused by earthquakes. *Geological Society of America Bulletin*, 95(4), 406–421.
- Keefer, D. K. (2000). Statistical analysis of an earthquake-induced landslide distribution—the 1989 Loma Prieta. *California Event. Engineering Geology*, 58(3–4), 231–249.
- Kim, J. M., & Sitar, N. (2013). Probabilistic evaluation of seismically induced permanent deformation of slopes. *Soil Dynamics and Earthquake Engineering*, 44, 67–77.
- Kramer, S. L. (1996). *Geotechnical earthquake engineering*. Pearson Education.
- Li, K., & Lumb, P. (1987). Probabilistic design of slopes. *Canadian Geotechnical Journal*, 24(4), 520–535.
- Li, D., Jiang, S., & Zhou, C., et al. (2013). Reliability analysis of slopes considering spatial variability of soil parameters using non-intrusive stochastic finite element method. *Chinese Journal of Geotechnical Engineering*, 35(8), 1413–1422.
- Li, D., Qi, X., & Phoon, K., et al. (2014). Effect of spatially variable shear strength parameters with linearly increasing mean trend on reliability of infinite slopes. *Structural Safety*, 49, 45–55.
- Li, Y., Conte, J. P., & Barbato, M. (2016). Influence of time-varying frequency content in earthquake ground motions on seismic response of linear elastic systems. *Earthquake Engineering and Structural Dynamics*, 45(8), 1271–1291.
- Lin, Y., Leng, W., & Yang, G., et al. (2015). Seismic response of embankment slopes with different reinforcing measures in shaking table tests. *Natural Hazards*, 76(2), 791–810.
- Lin, J. H., & Zhang, Y. H. (2004). Pseudo - excitation method for random vibration.
- Ling, H. I., Leshchinsky, D., & Chou, N. N. (2001). Post-earthquake investigation on several geosynthetic-reinforced soil retaining walls and slopes during the Ji-Ji earthquake of Taiwan. *Soil Dynamics and Earthquake Engineering*, 21(4), 297–313.
- Ling, H. I., Mohri, Y., & Leshchinsky, D., et al. (2005). Large-scale shaking table tests on modular-block reinforced soil retaining walls. *Journal of Geotechnical and Geoenvironmental Engineering*, 131(4), 465–476.
- Liu, H., Xu, Q., & Li, Y., et al. (2013). Response of high-strength rock slope to seismic waves in a shaking table test. *Bulletin of the Seismological Society of America*, 103(6), 3012–3025.
- Liu, J., Liu, F., & Kong, X., et al. (2014a). Large-scale shaking table model tests of aseismic measures for concrete faced rock-fill dams. *Soil Dynamics and Earthquake Engineering*, 61, 152–163.

- Liu, H., Xu, Q., & Li, Y. (2014b). Effect of lithology and structure on seismic response of steep slope in a shaking table test. *Journal of Mountain Science*, 11(2), 371–383.
- Liu, J., Liu, F., & Kong, X., et al. (2016). Large-scale shaking table model tests on seismically induced failure of concrete-faced rockfill dams. *Soil Dynamics and Earthquake Engineering*, 82, 11–23.
- Low, B., & Tang, W. H. (2007). Efficient spreadsheet algorithm for first-order reliability method. *Journal of Engineering Mechanics*, 133(12), 1378–1387.
- Low, B., Zhang, J., & Tang, W. H. (2011). Efficient system reliability analysis illustrated for a retaining wall and a soil slope. *Computers and Geotechnics*, 38(2), 196–204.
- Macedo, J., Bray, J., & Abrahamson, N., et al. (2018). Performance-based probabilistic seismic slope displacement procedure. *Earthquake Spectra*, 34(2), 673–695.
- Makdisi, F. I., & Seed, H. B. (1978). Simplified procedure for estimating dam and embankment earthquake-induced deformations. *Journal of the Geotechnical Engineering Division*, 104(7), 849–867.
- Malkawi, A. I. H., Hassan, W. F., & Abdulla, F. A. (2000). Uncertainty and reliability analysis applied to slope stability. *Structural Safety*, 22(2), 161–187.
- Marcuson, W. (1981). Moderator's report for session on earth dams and stability of slopes under dynamic loads. In *Paper presented at the proceedings of the international conference on recent advances in geotechnical earthquake engineering and soil dynamics*. University of Missouri.
- Michael, M., Al-Bittar, T., & Soubra, A. (2016). Effect of soil spatial variability on the dynamic behavior of a slope. In Paper presented at the VII European congress on computational methods in applied sciences and engineering. Crete Island, Greece.
- Newmark, N. M. (1965). Effects of earthquakes on dams and embankments. *Geotechnique*, 15(2), 139–160.
- Olsson, A. M. J., & Sandberg, G. E. (2002). Latin hypercube sampling for stochastic finite element analysis. *Journal of Engineering Mechanics-Asce*, 128(1), 121–125.
- Pan, D., & Lou, M. (2008). An approach to solve random seismic response of layered soil. *Engineering Mechanics*, 25(3), 91–95.
- Panah, A. K., Yazdi, M., & Ghalandarzadeh, A. (2015). Shaking table tests on soil retaining walls reinforced by polymeric strips. *Geotextiles and Geomembranes*, 43(2), 148–161.
- Peng, H., Deng, J., & Gu, D. (2005). Earth slope reliability analysis under seismic loadings using neural network. *Journal of Central South University of Technology*, 12(5), 606–610.
- Priestley, M. B. (1967). Power spectral analysis of non-stationary random processes. *Journal of Sound and Vibration*.
- Rüdiger, R., & Bernd, F. (1978). Structural reliability under combined random load sequences. *J Pergamon*, 9(5).
- Sandri, D. (1997). A performance summary of reinforced soil structures in the greater Los Angeles area after the Northridge earthquake. *Geotextiles and Geomembranes*, 15(4–6), 235–253.
- Sato, H. P., Hasegawa, H., & Fujiwara, S., et al. (2007). Interpretation of landslide distribution triggered by the 2005 Northern Pakistan earthquake using SPOT 5 imagery. *Landslides*, 4(2), 113–122.
- Schuellër, G. I. (1997). Special issue - A state-of-the-art report on computational stochastic mechanics - Preface. *Probabilistic Engineering Mechanics*, 12(4), 197–321.
- Schuellër, G. I. (2006). Developments in stochastic structural mechanics. *Archive of Applied Mechanics*, 75(10–12), 755–773.
- Seed, H. B. (1979). Soil liquefaction and cyclic mobility evaluation for level ground during earthquakes. *Journal of the Geotechnical Engineering Division-Asce*, 105(2), 201–255.
- Sepúlveda, S. A., Murphy, W., & Jibson, R. W., et al. (2005). Seismically induced rock slope failures resulting from topographic amplification of strong ground motions: The case of Pacoima Canyon. *California. Engineering Geology*, 80(3–4), 336–348.
- Shinoda, M., Horii, K., & Yonezawa, T., et al. (2006). Reliability-based seismic deformation analysis of reinforced soil slopes. *Soils and Foundations*, 46(4), 477–490.

- Srilatha, N., Latha, G. M., & Puttappa, C. G. (2013). Effect of frequency on seismic response of reinforced soil slopes in shaking table tests. *Geotextiles and Geomembranes*, 36, 27–32.
- Srivastava, A., Babu, G. S., & Haldar, S. (2010). Influence of spatial variability of permeability property on steady state seepage flow and slope stability analysis. *Engineering Geology*, 110(3–4), 93–101.
- Taha, M. R., Khajehzadeh, M., & El-Shafie, A. (2012). Application of particle swarm optimization in evaluating the reliability of soil slope stability analysis. *Sains Malaysiana*, 41(7), 847–854.
- Tan, X., & Wang, J. (2009). Finite element reliability analysis of slope stability. *Journal of Zhejiang University-SCIENCE A*, 10(5), 645–652.
- Tan, W., Cai, M., & Zhou, R. (2003). Modified fuzzy point estimate method and its application to slope reliability analysis. *Journal of University of Science and Technology Beijing*, 10(6), 5–10.
- Tang, C., Hu, J., & Lin, M., et al. (2009). The Tsaoling landslide triggered by the Chi-Chi earthquake, Taiwan: Insights from a discrete element simulation. *Engineering Geology*, 106(1–2), 1–19.
- Terzaghi, K. (1950). *Mechanism of landslides* (pp. 83–123). Geological Society of American.
- Tsompanakis, Y., Lagaros, N. D., & Psarropoulos, P. N., et al. (2010). Probabilistic seismic slope stability assessment of geostructures. *Structure and Infrastructure Engineering*, 6(1–2), 179–191.
- Vanmarcke, E. H. (1977). Probabilistic modeling of soil profiles. *Journal of the Geotechnical Engineering Division*, 103(11), 1227–1246.
- Wang, J., Yao, L., & Hussain, A. (2010). Analysis of earthquake-triggered failure mechanisms of slopes and sliding surfaces. *Journal of Mountain Science*, 7(3), 282–290.
- Wang, Y., Cao, Z., & Au, S. K. (2011). Practical reliability analysis of slope stability by advanced Monte Carlo simulations in a spreadsheet. *Canadian Geotechnical Journal*, 48(1), 162–172.
- Wartman, J., Bray, J. D., & Seed, R. B. (2003). Inclined plane studies of the Newmark sliding block procedure. *Journal of Geotechnical and Geoenvironmental Engineering*, 129(8), 673–684.
- Wartman, J., Seed, R. B., & Bray, J. D. (2005). Shaking table modeling of seismically induced deformations in slopes. *Journal of Geotechnical and Geoenvironmental Engineering*, 131(5), 610–622.
- Xue, J., & Gavin, K. (2007). Simultaneous determination of critical slip surface and reliability index for slopes. *Journal of Geotechnical and Geoenvironmental Engineering*, 133(7), 878–886.
- Yang, C., Zhang, J., & Liu, F., et al. (2015). Analysis on two typical landslide hazard phenomena in the Wenchuan earthquake by field investigations and shaking table tests. *International Journal of Environmental Research and Public Health*, 12(8), 9181–9198.
- Yang, G., Yu, T., & Yang, X., et al. (2017). Seismic resistant effects of composite reinforcement on Rockfill dams based on shaking table tests. *Journal of Earthquake Engineering*, 21(6), 1010–1022.
- Yeh, C. H., & Wen, Y. K. (1990). Modeling of nonstationary ground motion and analysis of inelastic structural response. *Structural Safety*, 8(1–4), 281–298.
- Yin, Y., Wang, F., & Sun, P. (2009). Landslide hazards triggered by the 2008 Wenchuan earthquake, Sichuan. *China. Landslides*, 6(2), 139–152.
- Yin, Y., Li, B., & Wang, W. (2015). Dynamic analysis of the stabilized Wangjiayan landslide in the Wenchuan Ms 8.0 earthquake and aftershocks. *Landslides*, 12(3), 537–547.
- Zhang, X. (1999). Slope stability analysis based on the rigid finite element method. *Geotechnique*, 49(5), 585–593.
- Zhang, Y., Chen, G., Zheng, L., Li, Y., & Wu, J. (2013). Effects of near-fault seismic loadings on run-out of large-scale landslide: a case study. *Engineering Geology*, 166(8), 216–236.
- Zhang, Y., Wang, J., Xu, Q., Chen, G., Zhao, J. X., & Zheng, L., et al. (2015). Dda validation of the mobility of earthquake-induced landslides. *Engineering Geology*, 194, 38–51.
- Zhang, Z., Wang, T., & Wu, S., et al. (2017). Investigation of dormant landslides in earthquake conditions using a physical model. *Landslides*, 14(3), 1181–1193.
- Zhao, H. (2008). Slope reliability analysis using a support vector machine. *Computers and Geotechnics*, 35(3), 459–467.
- Zhao, M., Huang, D., & Cao, M., et al. (2015). Shaking table tests on deformation and failure mechanisms of seismic slope. *Journal of Vibroengineering*, 17(1), 382–392.

Chapter 2

Theoretical Framework of Slope Stochastic Dynamics



Seismic engineering design and a large number of slope engineering tests have shown that slopes under seismic dynamic action behave as a nonlinear random dynamic system. Associated uncertainties arise from the rock and soil materials, slope geological conditions, geometric dimensions, and external excitation (mainly ground motion), among others. The uncertainty and randomness must be considered to more accurately grasp the dynamic response of slope engineering under possible ground motion conditions. The basic theory of slope stochastic dynamics is therefore established.

Slope stochastic dynamics includes a nonlinear seismic dynamic stability assessment framework for modeling, analysis, and evaluation of the slope stochastic seismic dynamic response based on dynamic reliability. The stochastic dynamic analysis method uses the dynamic time history analysis method to solve the associated equations and obtain the probability density function (PDF) solution of the slope random seismic response. Many different methods are available within the field of stochastic dynamics to handle stochastic dynamic problems whose uncertainties are derived from random initial conditions, random parameters, random excitation, and compound random factors. These random sources are usually characterized by random variables, random processes, random fields, and random waves.

In this book, the probability density evolution method (PDEM) is selected as a part of the theoretical framework of slope stochastic dynamics. Its main advantages are that the PDF of the nonlinear stochastic dynamic system can be obtained and less calculation is required. The PDEM follows the principle of probability conservation, which overcomes the difficulty of solving the general stochastic dynamic system for the high-dimensional and high-order Fokker–Planck–Kolmogorov (FPK) equation. It also overcomes the large amount of required calculation and random convergence of Monte Carlo random simulations.

The emergence and development of the PDEM therefore provide a theoretical basis for the random seismic response and seismic dynamic stability reliability analysis of slope. The concept of performance-based seismic design also provides a reference for the seismic evaluation and design of slopes.

2.1 General Process of Stochastic Seismic Dynamic Response Analysis

The theoretical framework and research contents of the stochastic dynamic analysis method are presented in detail in Fig. 2.1. The purpose of stochastic dynamic analysis includes three aspects: (1) solve the probability information of the slope dynamic stochastic system; (2) achieve a quantitative randomness characterization; and (3) verify and apply the stochastic dynamic analysis method.

A large number of slope engineering tests and seismic engineering design indicate that the response of slope under seismic dynamic action is related to the uncertainty of the rock and soil mass material, slope geological conditions, geometric size, and external excitation (mainly seismic ground motion excitation). In related studies, this has mainly been regarded as a nonlinear stochastic dynamical system composed of various randomness. In deterministic seismic dynamic analysis, the slope safety factor is a function of several geotechnical parameters and loads. Owing to the variability of the geotechnical parameters and randomness of the seismic excitations, it is clearly unreasonable to assess the slope safety degree based on the safety factor obtained from deterministic theory. There are some cases of slope failure in which the safety factor meets the slope engineering design requirements, for which the slope reliability analysis method based on uncertainty theory is presented.

The transition from certainty theory to uncertainty theory is the second theoretical leap from qualitative analysis to quantitative analysis in the process of slope stability research. To accurately grasp the dynamic response of slope engineering under unexpected ground motion, the above uncertainties and randomness must be considered and the seismic dynamic response of slope must be studied from the

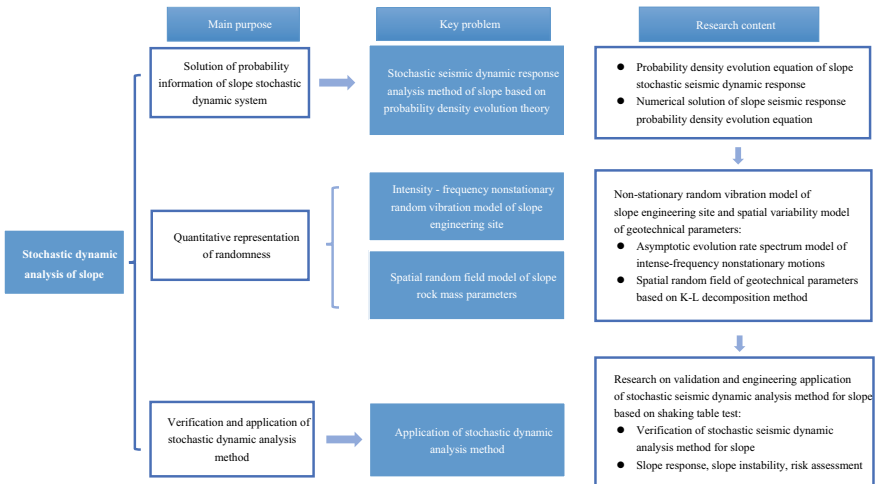


Fig. 2.1 Theoretical framework and research contents of stochastic dynamic analysis of slope under seismic activity

perspective of seismic dynamic reliability. The stochastic seismic dynamic response analysis method based on the PDEM is used to analyze the slope response from a random viewpoint.

At present, stochastic seismic dynamic response analysis mainly includes slope stochastic dynamic analysis based on rock and soil parameter uncertainties and/or ground motion uncertainties. The randomness of ground motion and geotechnical parameter uncertainties constitute the main sources of the uncertainty factors of a slope system. These two uncertainties can be quantified using a ground motion model and random field model. The random ground motion model selected in this book is the power spectrum model with a gradual evolution of intensity and frequency of non-stationary ground motion, which considers the non-stationary characteristics of ground motion, and the selected field parameters and model parameters are time-varying. A spatial random field model of slope rock and soil parameters are established based on the Karhunen-Loève (K-L) decomposition method to quantitatively characterize the spatial variabilities of the soil parameters. This method is an efficient way to compress the data and extract the essential features of the stochastic processes.

The stochastic dynamic analysis method for slope seismic dynamic response analysis is composed of a probabilistic information solution and quantitative characterization of randomness. In this book, the stochastic dynamic analysis method is applied to study the stochastic seismic response and seismic dynamic reliability analysis of slope. The numerical simulation process includes model building, stochastic seismic response analysis, reliability analysis, and results verification. The results obtained using the stochastic dynamic analysis method are compared and verified by shaking table tests. The results show that the stochastic dynamic analysis method has good accuracy for site evaluation, slope response, slope instability conditions, and slope reliability.

2.2 Probability Density Evolution Method

The description of the PDF is the most intrinsic expression of physical events. The PDEM follows the principle of probability conservation and overcomes the difficulty of obtaining a solution of a general stochastic dynamic system for the high-dimensional and high-order FPK equation (Boyadjiev, 1975).

After obtaining the PDF solution of the slope seismic response (e.g., displacement, acceleration, stress, and strain), the second-order statistics (e.g., mean and standard deviation) and higher-order statistics of the response can be further obtained by the integration of the PDF, which also overcomes the defects of Monte Carlo simulations (MCS), such as the large calculation amount and random convergence (Schueller, 1997).

The emergence and development of PDEM theory therefore provide a theoretical basis for the random seismic response and reliability analysis of seismic dynamic stability of slope. Furthermore, because it can be combined with the concept

of performance-based seismic design, the PDEM provides a reference for slope evaluation and design.

PDEM theory has benefited from the development of stochastic dynamic system analysis. In the past half century, extensive studies have made numerous fruitful advances in stochastic vibration theory and stochastic structural analysis theory.

From the aspect of stochastic vibration theory, which mainly considers load randomness, the theory of stationary response analysis of linear systems represented by the pseudo-excitation method is well suited and has been applied in engineering. For nonlinear dynamic systems, Zhu (2003) obtained a stationary analytical solution of the FPK equation based on Hamiltonian theory. The stochastic simulation method, stochastic perturbation method, and orthogonal polynomial expansion theory have been developed based on stochastic structural analysis theory, and good results have been achieved in solving linear stochastic structural systems (Schueller, 1997).

The PDEM theory can effectively consider the randomness from initial conditions, system parameters, and external loads. The stochastic and nonlinear state equations are decoupled using the stochastic event description of the probability conservation principle. The nonlinearity of the system is then handled based on the existing deterministic theory. After solving the generalized probability evolution equation (GDPE), the PDF of the nonlinear system is obtained. Because the PDF contains all the random information of the system, this method can realize the full-time refinement analysis, which covers the entire process of a slope system from static to vibration, and the final state is analyzed.

2.2.1 Principle of Probabilistic Conservation

The response of the slope dynamic system must be described as a stochastic process regardless of whether the randomness of a seismic dynamical system is derived from the initial conditions, external excitation, or system parameters. The statistical characteristics of these dynamical systems are completely dependent on the initial conditions, external excitation, and randomness of the system parameters. The influence of random factors must therefore be considered to analyze the seismic dynamic response of the slope. The stochastic vibration of the structure is divided into the stochastic dynamic response and seismic reliability analysis.

Similar to the conservation of energy, mass, and momentum in the physical theory of continuum mechanics, the conservation of probability is the basic principle of stochastic dynamical systems. The definition of probability conservation is that in a conservative stochastic system, the probability is conserved during the evolution of the state. A conservative stochastic system implies that no new random factors are added or existing ones disappear in the evolution process. There are two ways to describe the probability conservation principle: random event description and state space description (Chen & Li, 2009).

The probability conservation principle is described by a random event having the same probability in different moments of the system evolution. From the perspective

of state space, this principle is described that the increased probability of a fixed region in any time period is equal to the probability of crossing the boundary and entering the region in that time period. The basic principle of random event description is introduced according to the purpose of this book, and the GDEE is deduced.

On the basis of the probability conservation principle, the physical relationship between samples is reflected by the physical equations and evolution equation used to control the probability transfer process of the physical stochastic system.

An n -dimensional dynamical system is taken as an example to elaborate the probability conservation principle. For an n -dimensional stochastic dynamical system, this can be expressed as:

$$\dot{\mathbf{X}} = \mathbf{A}(\mathbf{X}, t), \mathbf{X}(t_0) = \mathbf{X}_0 \quad (2.1)$$

where $\mathbf{X} = (X_1, X_2, \dots, X_n)^T$ is the n -dimensional state vector, $\mathbf{X}_0 = (X_{0,1}, X_{0,2}, \dots, X_{0,n})^T$ is the initial state vector, and $\mathbf{A}(\cdot)$ is the deterministic operator vector.

When the initial condition \mathbf{X}_0 is given, the solution \mathbf{X} in Eq. (2.1) exists uniquely and continuously depends on the initial condition \mathbf{X}_0 , denoted as:

$$\mathbf{X}(t) = g(\mathbf{X}_0, t) \quad (2.2)$$

\mathbf{X}_0 is a random vector, and therefore the event $\{\mathbf{X}_0 \in \Omega_0\}$ is a random event, where Ω_0 is any region in the initial state space. When \mathbf{X}_0 evolves from time t_0 to $\mathbf{X}(t)$ at time t , Ω_0 also evolves over time to the region Ω_t , belonging to $\mathbf{X}(t)$, that is:

$$\Omega_t = g(\Omega_0, t) \quad (2.3)$$

Random events $\{\mathbf{X}_0 \in \Omega_0\}$ accordingly change with t for $\{\mathbf{X}(t) \in \Omega_t\}$, as shown in Fig. 2.2. These two random events are an equivalent random event, thus their probabilities must be equal, that is:

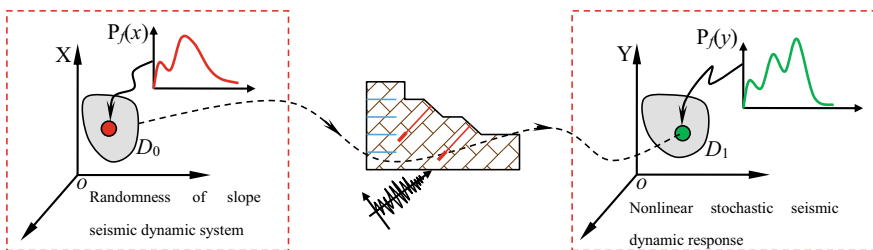


Fig. 2.2 From the randomness of a slope seismic dynamic system to the nonlinear stochastic seismic dynamic response of a slope

$$P_f(x) = P_f(y)\{X(t) \in \Omega_t\} \quad (2.4)$$

Let us assume that the joint PDF of the initial random vector X_0 is $P_{x_0}(x_0)$ and the joint PDF of $X(t)$ is $P_X(x, t)$, where $\mathbf{x}_0 = (x_{0,1}, x_{0,2}, \dots, x_{0,n})^T$ and $\mathbf{x} = (x_1, x_2, \dots, x_n)^T$. Equation (2.3) then changes to:

$$\int_{\Omega_t} P_X(\mathbf{x}, t) d\mathbf{x} = \int_{\Omega_t} P_X(\mathbf{x}, t_0) d\mathbf{x} \quad (2.5)$$

For convenience, Ω_0 is changed to Ω_{t_0} , then $P_X(\mathbf{x}, t) = P_{x_0}(\mathbf{x}_0, t)$. Equation (2.5) is valid for any t , thus:

$$\frac{D}{Dt} \int_{\Omega_t} P_X(\mathbf{x}, t) d\mathbf{x} = 0 \quad (2.6)$$

where $\frac{D(\cdot)}{Dt}$ represents the total derivative, and its exact meaning is:

$$\frac{D}{Dt} \int_{\Omega_t} P_X(\mathbf{x}, t) d\mathbf{x} = \lim_{\Delta t \rightarrow 0} \frac{1}{\Delta t} \left(\int_{\Omega_{t+\Delta t}} P_X(\mathbf{x}, t + \Delta t) d\mathbf{x} - \int_{\Omega_t} P_X(\mathbf{x}, t) d\mathbf{x} \right) \quad (2.7)$$

Equations (2.6) and (2.7) are mathematical expressions that describe random events under the principle of probability conservation.

2.2.2 Generalized Probability Density Evolution Equation

Randomness in engineering systems mainly originates from the parameters and load. The randomness of the parameters is noted as $\boldsymbol{\eta}$. The project of the dynamic load incentives (e.g., excitation of an earthquake, wind, and waves) is also considered a random process and the basic random variables are noted as $\boldsymbol{\omega}$.

To unify the symbols, all the basic random variables in the system are written as:

$$\boldsymbol{\Theta} = (\boldsymbol{\eta}, \boldsymbol{\omega}) = (\eta_1, \eta_2, \dots, \eta_{s_1}, \omega_1, \omega_2, \dots, \omega_{s_2}) = (\boldsymbol{\Theta}_1, \boldsymbol{\Theta}_2, \dots, \boldsymbol{\Theta}_s) \quad (2.8)$$

In the practice of slope seismic design and evaluation, the physical quantities of interest are not only the acceleration, velocity, and displacement of the system, but also the stress, strain, internal forces of the control interface, and the safety factor. These physical quantities can be precisely expressed as functions of velocity and displacement.

A random system composed of $(F_s(t), \boldsymbol{\Theta})$ is considered conservative because all of the random factors are included. Following the random event description of probability conservation (Eq. (2.6)) yields:

$$\begin{aligned}
& \frac{D}{Dt} \int_{\Omega_t \times \Omega_{\Theta}} p_{F_s, \Theta}(f_s, \theta, t) d f_s d \theta \\
&= \frac{D}{Dt} \int_{\Omega_{t_0} \times \Omega_{\Theta}} p_{F_s, \Theta}(f_s, \theta, t) |J| d f_s d \theta \\
&= \int_{\Omega_{t_0} \times \Omega_{\Theta}} \left[|J| \frac{D p_{F_s, \Theta}(f_s, \theta, t)}{Dt} + p_{F_s, \Theta}(f_s, \theta, t) \frac{D|J|}{Dt} \right] d f_s d \theta \\
&= \int_{\Omega_{t_0} \times \Omega_{\Theta}} \left[|J| \left(\frac{\partial p_{F_s, \Theta}}{\partial t} + \sum_{j=1}^m r_j \frac{\partial p_{F_s, \Theta}}{\partial f_{s,j}} \right) + P_{Z\Theta} |J| \sum_{j=1}^m \frac{\partial(r_j)}{\partial(f_{s,j})} \right] d f_s d \theta \\
&= \int_{\Omega_{t_0} \times \Omega_{\Theta}} |J| \left(\frac{\partial p_{F_s, \Theta}}{\partial t} + \sum_{j=1}^m r_j \frac{\partial p_{F_s, \Theta}}{\partial f_{s,j}} \right) d f_s d \theta \\
&= \int_{\Omega_{t_0} \times \Omega_{\Theta}} \left(\frac{\partial p_{F_s, \Theta}}{\partial t} + \sum_{j=1}^m r_j \frac{\partial p_{F_s, \Theta}}{\partial f_{s,j}} \right) d f_s d \theta = 0 \tag{2.9}
\end{aligned}$$

where $|J|$ is the Jacobian determinant and $p_{F_s, \Theta}(f_s, \theta, t)$ is the joint PDF of $(F_S(t), \Theta)$. Because Ω_t can be a region at any time, the following can be obtained according to Eq. (2.9):

$$\frac{\partial p_{F_s, \Theta}(f_s, \theta, t)}{\partial t} + \sum_{j=1}^m r_j \frac{\partial p_{F_s, \Theta}(f_s, \theta, t)}{\partial f_{s,j}} = 0 \tag{2.10}$$

The above equation is the generalized probability density evolution equation, which is a partial differential equation and its initial condition is:

$$p_{F_s, \Theta}(f_s, \theta, t) \Big|_{t=t_0} = \delta(f_s - f_{s_0}) p_{\Theta}(\theta) \tag{2.11}$$

where f_{s_0} is the deterministic initial value and $\delta(\cdot)$ is the Dirichlet function.

2.2.3 Numerical Solution of the GDEE

The closed analytical solution of the GDEE can be obtained for some simple problems. However, approximate solutions are generally adopted for most practical slope engineering problems, which are obtained using numerical methods. The specific implementation steps are as follows.

- (1) A series of discrete points is selected on behalf of the probability distribution of random variables Θ in space Ω_{Θ} , namely $\theta_q = (\theta_{q,1}, \theta_{q,2}, \dots, \theta_{q,s})$, where $q =$

$1, 2, \dots, n_{sel}, n_{sel}$ is the number of discrete sample points. The assigned probability P_q of each discrete representative point can then be calculated according to:

$$P_q = \int V_q p_{\Theta}(\theta) d\theta \quad (2.12)$$

where V_q is the representative volume.

- (2) The time derivative of the safety factor, $\dot{F}_{s,j}(\boldsymbol{\theta}, t)$, can be obtained for a given $\boldsymbol{\Theta} = \boldsymbol{\theta}_q$, using the deterministic dynamic equation numerical solution method, such as the Newmark- β and Wilson- θ method.
- (3) The $\dot{F}_{s,j}(\boldsymbol{\theta}, t)$ obtained in step 2 is substituted into the generalized probability density evolution in Eq. (2.10). The finite difference numerical method is used to solve the problem combined with the initial conditions in Eq. (2.19).
- (4) After all values of $P_{F_s, \boldsymbol{\Theta}}(f_s, \theta, t)$ are determined, the numerical solution of the PDF $P_{F_s}(f_s, t)$ can be obtained by summation:

$$P_{F_s}(f_s, t) = \sum_{q=1}^{n_{sel}} P_{F_s, \boldsymbol{\Theta}}(f_s, \theta, t) \quad (2.13)$$

2.3 Random Field Expression of Spatial Variability of Slope Rock and Soil Parameters

The uncertainty of geotechnical parameters in the stochastic dynamic analysis of slope refers to the spatial variability of geotechnical parameters. Numerous studies have addressed the variability of geotechnical parameters mainly because those obtained from geotechnical and in situ tests inevitably have certain variability. These include the strength parameters obtained from indoor geotechnical tests, geotechnical parameters obtained from cross-plate shear tests, shear wave velocities obtained from in situ tests, and supporting structure parameters (Al-Homoud & Tahtamoni, 2000, 2001; Kramer & Paulsen, 2004; Tsompanakis et al., 2010). The study of slope geotechnical parameter variability has important practical significance in engineering (Wu, 2015).

The first-order second-moment method or MCS method are used to calculate the failure probability when considering the variation of rock and soil parameters of a slope (Griffiths et al., 2009; Jiang et al., 2017; Peng et al., 2005). If the PDF of the parameters is known, the MCS method can be used to generate random analysis samples of the slope, after which the quasi-static method or Newmark rigid slider

method can be used for the seismic dynamic analysis to obtain a dynamic solution. It should be pointed out that these two methods are slightly oversimplified to handle earthquake action. For example, quasi-static analysis may only be able to consider earthquake action for the earthquake of magnitude 7–8. The non-linearity of rock and soil materials and magnifying effect of the slope on ground motion can therefore not be well considered (Johari & Khodaparast, 2015).

Several studies have considered the spatial variability of slope geotechnical parameters but mainly focused on the static problem, and the dynamic response of slope has not yet been considered. This results in inconsistencies between the analysis and actual response of the slope. The spatial variability of geotechnical parameters refers to rock mass parameters that are related to the spatial location, which is mainly considered to be influenced by the deposition and consolidation history.

Random field theory is introduced to study the uncertainty of rock and soil parameters.

The proper orthogonal decomposition (POD) method is an efficient data compression and extraction method for stochastic processes, and is closely related with principal component analysis, also known as the K-L decomposition method, which is adopted in this book. Higher accuracy is achieved and fewer items must be expanded for specific accuracy when using the K-L decomposition method to simulate a random field (Ghiocel & Ghanem, 2002). The K-L decomposition method is introduced to establish the random field model and quantitatively characterize the spatial variability of rock and soil mass parameters.

In K-L decomposition theory, a random field can be described by a series of random variables and deterministic spatial correlation functions. Two-dimensional random fields can be expanded as:

$$R_k(x, y; \vartheta) = \mu_k + \sum_{i=1}^{\infty} \lambda_i \vartheta_i(x, y) \xi_{k,i}(\vartheta), \quad (x, y) \in \Omega \quad (2.14)$$

where μ_k and σ_k are the mean and standard deviation of the geotechnical engineering parameter, respectively, $\xi_{k,i}(\vartheta)$ is the mutually independent standard normal random variable, ϑ is outer space coordinates, (x, y) is a two-dimensional random field model of structural system Ω coordinates, and λ_i and $\phi_i(x, y)$ are the eigenvalues of the autocorrelation function and characteristic function, respectively, which can be determined by:

$$\int \Omega \rho(x, x') \phi_i(x') d\Omega_{x'} = \lambda_i \phi_i(x) \quad (2.15)$$

where $\rho(x, x')$ is the autocorrelation function. The exponential autocorrelation function is adopted here, which is given as:

$$\rho(x, y) = \exp\left(-\frac{|x - x'|}{l_x} - \frac{|y - y'|}{l_y}\right) \quad (2.16)$$

where l_x and l_y are horizontal and vertical components the autocorrelation distance, respectively. Considering the anisotropy of rock and soil mass materials, different autocorrelation distances are adopted in the horizontal and vertical directions (i.e., different l_x and l_y values). To ensure accuracy, the first n items in Eq. (2.14) can be intercepted as:

$$\widehat{R}_k(x, y; \vartheta) = \mu_k + \sum_{i=1}^n \sigma_k \sqrt{\lambda_i} \varphi_i(x, y) \xi_{k,i}(\vartheta), \quad (x, y) \in \Omega \quad (2.17)$$

where n is the number of terms in the expanded series and a parameter that controls the random field expansion depending on the required precision and selected autocorrelation function. To guarantee the accuracy of the generated random fields, n is set here to 150 according to the suggestion by Cho (2010).

Previous studies showed that the different parameters in geotechnical engineering are relevant. For considering the relationship between the parameters of rock body, according to Vorechovsky (2008), the independent standard normal distribution and related random variables in Eq. (2.17) not associated with the Gaussian random field can be converted into the following Gaussian correlation random field model:

$$\widehat{R}_k^C(x, y; \vartheta) = \mu_k + \sum_{i=1}^n \sigma_k \sqrt{\lambda_i} \varphi_i(x, y) \chi_{k,i}(\vartheta), \quad (x, y) \in \Omega \quad (2.18)$$

A Gaussian distribution may be not applicable in engineering practice because the physical and mechanical parameters of rock and soil are all positive. Geotechnical parameters can generally be assumed to have a lognormal distribution with a relatively large distribution range. The uncertainty of geotechnical parameters with relatively large variability can thus be analyzed (Nour et al., 2003). The Gaussian correlation random field can therefore be transformed into a non-Gaussian correlation random field model according to:

$$\widehat{R}_k^{CN}(x, y; \theta) = \exp\left(\mu_{lnk} + \sum_{i=1}^n \sigma_{lnk} \sqrt{\lambda_i} \varphi_i(x, y) \chi_{k,i}(\vartheta)\right), \quad (x, y) \in \Omega \quad (2.19)$$

The POD method was first applied to the study of fluid dynamics and turbulence by Lumley (1967), who investigated the deterministic function to describe a random process and proved that using the characteristic function of the covariance function of the random process can directly describe the random process itself. Aubry et al. (1993) proposed that the POD symmetry must be retained even if the energy is zero. The eigen orthogonal expansion method was first applied to structural

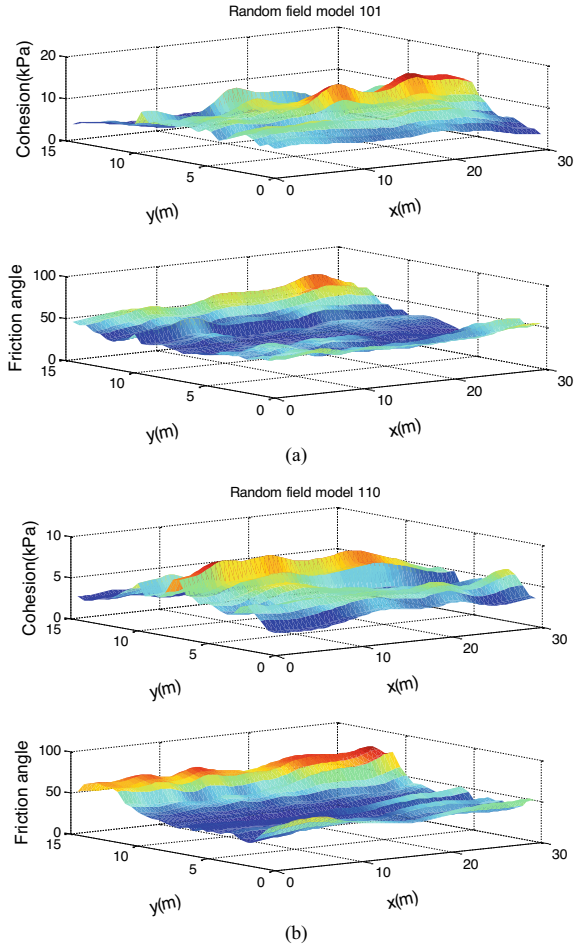
dynamics by Masri et al. (1998), who proposed a mathematical analytical expression of the linear response covariance function of a single degree of freedom system through the progressive spectral decomposition of the covariance function of a non-stationary random process. Masri et al. (1998) used the eigen orthogonal expansion method to analyze the seismic non-stationary responses of single-degree-of-freedom and multi-free systems. Gullo et al. (1998) decomposed the stationary process into the sum of several sub-vector processes, and established the response moment of wind-earthquake excitation for systems with multiple degrees of freedom. Tubino et al. (2003) used the POD method of ground motion to decouple the quasi-static and dynamic parts of a multi-point support structure. Cusumano and Bai (1993) proposed that the eigen orthogonal expansion method should be used to identify the base-dimensional subspace. Rathinam and Petzold (2003) proposed a theoretical framework of an eigen orthogonal expansion method for nonlinear dynamic systems.

DiPaola and Pisano (1996) embedded the spectral decomposition of the cross PSD matrix of a multivariable random process into a MCS to simulate the wave random field, and pointed out that the combination of random and spectral decomposition is necessary to a considerable extent. Grigoriu (2004) evaluated the advantages and disadvantages of the eigen orthogonal expansion method and pointed out that the spectrum representation method is a special case in the analysis of problems related to stationary random processes. Phoon et al. (2005) implemented the simulation analysis of strongly non-Gaussian stochastic processes through the eigen orthogonal expansion method. Chen and Kareem (2005) embedded the POD method into the autoregressive method, and pointed out its advantages in wind-load random field simulations. Carassale and Solari (2006) used the POD method to simulate a turbulent field in complex regions.

The most important point in the generation of a random field model is to estimate and obtain the required statistical parameters, including the mean value, standard deviation, autocorrelation distance, and autocorrelation function. However, field data are often limited and difficult to obtain. Moreover, the data obtained by conventional geotechnical engineering investigation methods are insufficient, and it can be difficult to obtain a reliable statistical distribution law of geotechnical body parameters using these data. It is also impossible to evaluate the variability of the geotechnical body parameters with a reasonable confidence interval (Montoya-Noguera et al., 2019). However, sparsely measured data can also be used to estimate the probability distribution model of the parameters based on reasonable distribution assumptions. In the simulation of random fields, most studies have therefore been based on the distribution hypothesis and available data in the literature.

Figure 2.3. The values of the rock and soil mass parameters clearly differ in different spatial positions, and the spatial variation forms and rules also vary in different random fields.

Fig. 2.3 Examples of two cross-correlated non-Gaussian random fields of the cohesion (a) and friction angle (b)



2.4 Seismic Ground Motion Models

Research on the randomness of ground motion in stochastic dynamic analysis of slopes mainly includes the randomness of the input parameters of ground motion and the randomness of the time history of ground motion samples. The randomness of input parameters of ground motion refers to the uncertainty of considering seismic action in quasi-static analysis or the Newmark rigid slider method. The randomness of input parameters refers to the randomness of ground action in quasi-static analysis or Newmark analysis. For example, Al-Homoud and Tahtamoni (2001) assumed the distribution of physical quantities such as epicenter distance, strong earthquake duration, and peak acceleration (e.g., uniform distribution, normal distribution) when studying the variability of ground motion. Tsompanakis et al. (2010) used the pseudo-static method to analyze slope dynamic vulnerability, but the horizontal seismic

action coefficient had a certain variability. Strenk and Wartman (2011) showed that there is a certain variability of the false seismic yield acceleration when applying the Newmark rigid slider method to calculate the permanent displacement of a slope.

An appropriate number of measured ground motion data can be selected from the available seismic database (Rathje et al. 2010), and the generation of the time history of ground motion samples can depend on random vibration theory (Huang & Xiong, 2017a, b; Kim & Sitar, 2013; Pang et al., 2018a, b), which is an advanced research method to generate the time history of ground motion samples using random vibration theory in dynamic analysis.

The development of seismic engineering and random vibration theory has allowed non-stationary characteristics to be considered in the stochastic dynamic analysis of slopes. Related random vibration theories, such as the pseudo-excitation method and PDEM, have been gradually applied in slope engineering (Huang et al., 2018, 2019; Huang & Xiong, 2017a, b). For example, some scholars have considered the randomness of ground motion in seismic studies of earth-rock dams and concrete face rockfill dams. Dynamic time history analysis has indicated that ground motion randomness is an important factor that affects the dynamic response and reliability of slopes (Pang et al., 2018a, b).

2.4.1 Stochastic Seismic Ground Motion Model

The randomness of earthquake activity occurs not only in time and space, but also in the focal mechanism, propagation route, and site conditions. The randomness of both the seismicity and ground motion are two parts that contribute to the overall randomness of ground motion. An approach to reasonably simulate and predict the randomness of ground motion is a popular yet difficult problem in ground motion input research. The first step of seismic design in slope engineering is to determine the ground motion. Reasonable ground motion input is a necessary condition to ensure the correct design result. Without a reasonable ground motion model design, the seismic resistance of slope engineering can only remain in the seismic damage investigation stage and be tested or numerical analyzed using strong earthquake data. Since Housner (1947) first proposed stochastic processes to simulate seismic ground motion in 1947, stochastic ground motion models and their engineering applications have been studied in depth.

Stochastic ground motion models are divided into three categories: stationary random vibration models; intensity single non-stationary random vibration models; and intensity-frequency non-stationary stochastic ground motion models.

(1) Stationary random vibration model

a. *White noise model*

White noise is a stationary random process with a zero mean value and constant power spectral density (PSD) function. This approach was first used to simulate the

random process of ground motion following the ideal white noise model proposed by Housner (1947), which simulates the process of ground motion as a random pulse according to the limited acceleration records of strong earthquakes. The PSD function of ground motion can be expressed as:

$$S(\omega) = S_0, \quad -\infty < \omega < \infty \quad (2.20)$$

$$\sigma^2 = \int_{-\infty}^{\infty} S(\omega) d\omega = \infty \quad (2.21)$$

where S_0 is a constant that reflects the ground motion intensity. This model assumes the power spectrum is a specific constant, which can reflect the engineering characteristics to a certain extent, such as the ground motion amplitude. However, it has infinite variance, and thus infinite total energy, which is purely theoretical and contrary to actual situations. Although the white noise model is only based on mathematical considerations, it has no specific physical meaning. Nevertheless, it has laid a useful theoretical foundation for the study of random ground motion modeling.

b. *Kanai-Tajimi model—filter white noise model*

Tajimi (1960) regarded the ground motion of bedrock as white noise and the overburden of bedrock as a linear filter of a single degree of freedom. The smooth white noise process is linearly filtered to obtain the filtered white noise model (K-T model), and the acceleration power spectrum is expressed as follows:

$$S_{k-T}(\omega) = \frac{(\omega_g^4 + 4\xi_g^2 \omega_g^2 \omega^2) \cdot S_0}{(\omega^2 - \omega_g^2)^2 + 4\xi_g^2 \omega_g^2 \omega^2} \quad (2.22)$$

This model considers the physical nature of ground motion, such as the influence of soil layer characteristics on the spectral characteristics of ground motion, and can effectively simulate the ground motion characteristics of an earthquake. However, the final velocity and displacement power spectrum exist in singularity at the zero frequency, and the mean square velocity are unbounded. This effect may not be particularly good when applying the K-T model to analyze the response of low-frequency structures with ground motion because it enhances the influence of the low-frequency ground motion content.

c. *Clough-Penzien model—double filter white noise model*

To solve the singular point problem, Clough and Penzien (1975) modified the low-frequency energy of the K-T model and proposed a double-filter white noise model (C-P model), in which the foundation rock and site soil are assumed as second-order linear filters. In the second filtration, the appropriate frequency and damping parameters are selected for the required filtering characteristics to eliminate extremely low frequencies. The PSD function of the improved C-P model is:

$$S_{C-P}(\omega) = \frac{(\omega_g^4 + 4\xi_g^2\omega_g^2\omega^2) \cdot \omega^4 \cdot S_0}{\left((\omega^2 - \omega_g^2)^2 + 4\xi_g^2\omega_g^2\omega^2\right) \cdot \left((\omega^2 - \omega_f^2)^2 + 4\xi_f^2\omega_f^2\omega^2\right)} \quad (2.23)$$

$$\omega_f = 0.1 \text{ } 0.2\omega_g; \quad \xi_f = \xi_g \quad (2.24)$$

where ω_g and ξ_g are the prominent circular frequency and site damping ratio of the site soil, respectively, ω_f and ξ_f are the secondary filtration frequency parameters and damping ratio parameters, respectively, that control the variation of the low-frequency ground motion energy, and S_0 is the spectral intensity of white noise on the bedrock.

d. *Other improved filter white noise models based on the K-T model*

Numerous earthquake engineering studies have improved the shortcomings of the K-T model from different angles, as shown in Table 2.1.

In view of the two classical filter white noise models, namely the C-P model and improved filter white noise model 1, it has been pointed out that the C-P model is more reasonable for seismic random response analysis of long-period structures because it can more fully reflect the possible variation of low-frequency ground motion energy.

(2) **Intensity single non-stationary earthquake ground motion model**

The measured earthquake time-history record reflects a non-stationary process that consists of three parts: a strengthening stage; a stationary stage; and a weakening stage. Strictly speaking, intensity varies with time and its non-stationarity is mainly reflected in the two dimensions of the time domain and frequency domain, including intensity non-stationarity (time-domain non-stationarity) and frequency non-stationarity (frequency-domain non-stationarity characteristics). The frequency composition of the ground motion process exhibits notable time-varying characteristics.

a. *Intensity non-stationary earthquake ground motion model*

The ground motion model of a stationary earthquake only describes the statistical characteristics of the stationary phase. Thus, in engineering applications, the intensity non-stationarity of ground motion is mainly reflected by multiplying the stationary model by the time-varying intensity envelope function.

The non-stationarity of ground motion has been extensively studied and a corresponding non-stationarity model of intensity has been proposed, as shown in Table 2.2. Among them, the Bolotin model is widely used and plays a crucial role in the field of engineering.

On the basis of the power spectrum evolution theory of the non-stationary random process of ground motion, the power spectrum density function of the evolution of the non-stationary process of ground motion acceleration intensity can be expressed as:

$$S(t, \omega) = |f(t)|^2 \cdot S(\omega) \quad (2.25)$$

Table 2.1 Improved filter white noise models

White noise model	PSD function	Description
Improved filter white noise Model 1 (Hu & Zhou, 1962)	$S(\omega) = \frac{(\omega_g^4 + 4\xi_g^2 \omega_g^2 \omega^2) \cdot \omega^n \cdot S_0}{\left((\omega^2 - \omega_g^2)^2 + 4\xi_g^2 \omega_g^2 \omega^2 \right) \cdot (\omega^n + \omega_c^n)}$	ω_c is the low-frequency content and the value range of parameter n is 4 ~ 6
Improved filter white noise Model 2 (Matsushima, 1986)	$S'_0(\omega) = \frac{S_0}{1 + \frac{\omega^2}{\omega_k^2}}$	Markov spectrum
	$S(\omega) = \frac{(\omega_g^4 + 4\xi_g^2 \omega_g^2 \omega^2) \cdot S'_0(\omega)}{\left((\omega^2 - \omega_g^2)^2 + 4\xi_g^2 \omega_g^2 \omega^2 \right)}$	ω_k is the spectral parameter representing ground motion parameters
Improved filter white noise Model 3 (Hong et al., 1994)	$S(\omega) = \frac{(\omega_g^4 + 4\xi_g^2 \omega_g^2 \omega^2) \cdot \omega^2 \cdot S_0}{\left((\omega^2 - \omega_g^2)^2 + 4\xi_g^2 \omega_g^2 \omega^2 \right) \cdot (\omega^2 + \omega_c^2)}$	ω_c is the filter parameter
Improved filter white noise Model 4 (Du & Chen, 1994a, b)	$L(\omega) = \frac{1}{1 + (D\omega)^2}$	Low pass and high pass filters are introduced, and D is the source parameter
	$H(\omega) = \frac{\omega^4}{\omega^2 + \omega_0^2}$	
	$S(\omega) = \frac{(\omega_g^4 + 4\xi_g^2 \omega_g^2 \omega^2) \cdot L(\omega) \cdot H(\omega) \cdot S_0}{\left((\omega^2 - \omega_g^2)^2 + 4\xi_g^2 \omega_g^2 \omega^2 \right)}$	
Improved double filter white noise Model (Lai et al., 1995)	$S(\omega) = \frac{(\omega_1^4 + 4\xi_1^2 \omega_1^2 \omega^2) \cdot (\omega_2^4 + 4\xi_2^2 \omega_2^2 \omega^2) \cdot S_0}{\left((\omega^2 - \omega_1^2)^2 + 4\xi_1^2 \omega_1^2 \omega^2 \right) \cdot \left((\omega^2 - \omega_2^2)^2 + 4\xi_2^2 \omega_2^2 \omega^2 \right)}$	ω_1, ξ_1 and ω_2, ξ_2 are respectively the circular frequency and damping ratio of surface soil and bedrock
Matsuda-Asano model (Matsuda & Asano, 2006)	$S(\omega) = \frac{\omega_g^2 \omega^2 \cdot S_0}{\left(\omega^2 - \omega_g^2 \right)^2 + 4\xi_g^2 \omega_g^2 \omega^2}$	Only have ω_g (Superior circle frequency), ξ_g (Damping ratio) and S_0 (Spectral intensity factor) three parameters

where $S(\omega)$ is the acceleration PSD function of the stationary random ground motion model.

Numerous strength envelope functions have been proposed in the literature, which can be divided into two categories: (1) a piecewise expression of curvilinear envelope functions; and (2) continuous curvilinear unimodal envelope functions. Four commonly used strength envelope functions are listed in Table 2.3.

The non-stationary characteristics of ground motion are realized by the intensity envelope function. This means that the amplitude of the ground motion acceleration time history varies with time, but its frequency component remains the same in each

Table 2.2 Intensity non-stationary random vibration model

Intensity non-stationary model	Functional expression	Description
Cornell model (Cornell, 1960)	$a(t) = \sum_j V_j f(\tau_j) h'(t - \tau_j)$	$H(t)$ is Heaviside step function, V_j is random variable; The strength is nonstationary through $f(t)$
	$f(t) = e^{-\alpha t} H(t)$	
	$h^*(t) = \sin 2\pi t/l$	
Bolotin model (Bolotin, 1960)	$a(t) = f(t) \cdot x(t)$	$f(t)$ is the deterministic envelope function, and $x(t)$ is the stationary vibration model
Goldberg model (Goldberg et al., 1964)	$a(t) = \sum_j V a_j t e^{-\alpha_j t} H(t) \cos(\omega_j t + \varphi_j)$	Attenuated trigonometric superposition model, $\omega_j, \varphi_j \in (0, 2\pi)$
Amin and Ang model (Amin & Ang, 1968)	$a(t) = f(t) \cdot x_0(t)$	$f(t)$ is the deterministic envelope function, $x_0(t)$ is a standardized high stage process
Ruiz and Penzien model (Ruiz & Penzien, 1969)	$a(t) = f(t) \cdot W(t)$	Bedrock acceleration filtering granular noise model, $W(t)$ has granular noise characteristics

Table 2.3 Commonly used strength envelope functions

Expression of strength envelope function	Parametric description
$f(t) = \begin{cases} \left(\frac{t}{t_1}\right)^2 & t \leq t_1 \\ 1 & t_1 < t \leq t_2 \\ \exp[-c(t - t_2)] & t > t_2 \end{cases}$	t_1 and t_2 are the first and last moments of the peak stationary period, and the speed of attenuation can be controlled by c (Amin & Ang, 1968)
$f(t) = a(t) \exp(-bt) \quad a > 0, b > 0$	b is the number at which the peak acceleration arrives: a is the cross product of b and the Euler number e (Bogdanoff et al., 1961)
$f(t) = \left[\frac{t}{c} \exp\left(1 - \frac{t}{c}\right)\right]^d \quad d = 1 \sim 3$	c control the arrival time of peak ground motion acceleration (Ou & Wang, 1998)
$f(t) = I_0 (e^{-at} - e^{-bt})$	I_0 is the intensity factor, and a, b control the peak point and shape of the function (Hu & Zhou, 1962)
$t^* = \frac{\ln b - \ln a}{b - a}; I_0 = \frac{1}{e^{-at^*} - e^{-bt^*}}$	

time period and the frequency remains stable. However, different frequency components have a significant influence on the analysis of the random dynamic response of strongly nonlinear structure ground motion, thus both intensity and frequency non-stationarity should be considered in random ground motion models.

b. *Intensity-frequency non-stationary earthquake ground motion model*

There are presently two effective ways to fully consider the intensity and frequency non-stationary aspects of random ground motion models. The first is to consider the frequency content in the intensity envelope function mentioned in the intensity non-stationary earthquake ground motion model. In the second one, the time variation is considered in the frequency parameters of the stationary power spectrum model.

The first type of intensity-frequency non-stationary earthquake ground motion models considers the frequency content in the intensity envelope function. Kameda (1975) described the random process of intensity-frequency non-stationary ground motion acceleration as follows:

$$a(t) = \int_{-\infty}^{\infty} A(t, \omega) e^{-i\omega t} dZ(\omega) \quad (2.26)$$

Its evolutionary PSD function is:

$$S_A(t, \omega) = |A(t, \omega)|^2 S(\omega) \quad (2.27)$$

is the PSD function of the stationary random process of ground motion acceleration, where $A(t, \omega)$ is the time–frequency modulation function determined at time t and frequency ω .

The study of the time–frequency modulation function $A(t, \omega)$ is the key to realize the intensity-frequency non-stationary model. To solve this problem, many scholars have constructed the frequency modulation function based on the existing intensity envelope function, and jointly constituted the time–frequency modulation function.

Hu and Chen (2008) proposed a dual-modulation function model:

$$A(t, \omega) = I_0 \left[\exp\left(-b_1 \frac{\omega t}{\omega_a t_a}\right) - \exp\left(-b_2 \frac{\omega t}{\omega_a t_a}\right) \right] f(t) \quad (2.28)$$

where I_0 is the intensity factor, $f(t)$ is the intensity envelope function, and b_1 and b_2 are the shape parameters that control the frequency modulation function. The value of parameters ω_a and t_a is related to the ground motion condition.

The second type of intensity-frequency non-stationary earthquake ground motion model takes into account the variation of the frequency parameter time. The process of temporal change is considered in the frequency parameters of the stationary power spectrum model, and the function is expressed as:

$$S_A(t, \omega) = |f(t)|^2 S(t, \omega) \quad (2.29)$$

where $f(t)$ is the intensity envelope function and $S_A(t, \omega)$ is the time–frequency power spectrum model that accounts for the frequency variation.

On the basis of the Clough-Penzien power model, Deodatis (1996) proposed that the frequency and damping ratio of the site prominent circle evolve over time. Cacciola and Deodatis (2011) made further modifications and its PSD function is expressed as:

$$S_A(t, \omega) = f^2(t) \cdot \frac{(\omega_g^4(t) + 4\xi_g^2(t)\omega_g^2(t)\omega^2) \cdot \omega^4 \cdot S_0(t)}{\left((\omega^2 - \omega_g^2(t))^2 + 4\xi_g^2(t)\omega_g^2(t)\omega^2\right) \cdot \left((\omega^2 - \omega_f^2(t))^2 + 4\xi_f^2(t)\omega_f^2(t)\omega^2\right)} \quad (2.30)$$

$$\omega_g(t) = 20 - 7\frac{t}{30}; \quad \xi_g(t) = 0.6 - 0.2\frac{t}{30} \quad (2.31)$$

$$\omega_f(t) = 0.1\omega_g(t); \quad \xi_f(t) = \xi_g(t) \quad (2.32)$$

$$S_0(t) = \frac{s^2}{\gamma^2\pi\omega_g(t)\left(2\xi_g(t) + \frac{1}{2\xi_g(t)}\right)}; \quad s = 1m/s^2 \quad (2.33)$$

where $f(t)$ is the intensity envelope function. As shown in Table 2.3, parameter s can be modified to the mean value of ground motion peak acceleration, and parameter r is the effective peak factor.

The random ground motion model adopted in this book is an intensity-frequency non-stationary model, and the selection of model parameters accounts for the characteristics of the slope engineering site (Huang et al., 2018; Huang & Xiong, 2017a). As a relatively advanced seismic dynamic model, this approach considers the non-stationary characteristics of ground motion and the selected site parameters and model parameters are time-varying.

The adopted random ground motion model is an evolutionary rate spectrum model based on the modified C-P spectrum (Cacciola & Deodatis, 2011). The C-P power spectrum and modified evolutionary power spectrum are respectively given as:

$$S(\omega) = \frac{\omega_g^4 + 4\xi_g^2\omega_g^2\omega^2}{(\omega_g^2 - \omega^2) + 4\xi_g^2\omega_g^2\omega^2} \times \frac{\omega^4}{(\omega_f^2 - \omega^2) + 4\xi_f^2\omega_f^2\omega^2} \cdot S_0 \quad (2.34)$$

$$S(t, \omega) = \frac{\omega_g^4(t) + 4\xi_g^2(t)\omega_g^2(t)\omega^2}{[\omega^2 - \omega_g^2(t)]^2 + 4\xi_g^2(t)\omega_g^2(t)\omega^2} \times \frac{\omega^4 \cdot S_0(t)}{[\omega^2 - \omega_f^2(t)]^2 + 4\xi_f^2(t)\omega_f^2(t)\omega^2} \quad (2.35)$$

where $\omega_g(t)$ and $\xi_g(t)$ are functions of the circular frequency and damping ratio of the slope site with time, respectively, and $\omega_f(t)$ and $\xi_f(t)$ are the time-varying frequency parameters and time-varying damping parameters considering the filtration characteristics, respectively. For general ground motion, $\xi_f(t) = \xi_g(t)$ can be

assumed and $S_0(t)$ is called the spectral intensity factor. The relevant expression can be written as:

$$S_0(t) = 2 \frac{\bar{a}_{\max}^2}{\bar{r}^2 \pi \omega_g(t) \left(2\xi_g(t) + \frac{1}{2\xi_g(t)} \right)} \quad (2.36)$$

$$\omega_g(t) = \omega_0 - a \left(\frac{t}{T} \right)^p; \xi_g(t) = \xi_0 + b \left(\frac{t}{T} \right)^p \quad (2.37)$$

$$\omega_f(t) = 0.1\omega_g(t); \omega_0 = \bar{\omega}_g + \frac{a}{2}\xi_g - \frac{b}{2} \quad (2.38)$$

$$A(t) = \left[\frac{t}{c} \exp\left(1 - \frac{t}{c}\right) \right]^d \quad (2.39)$$

where T is the ground motion duration, p is the shape control variable of the function, where $p = 1$ represents the linear time variation, ω_0 and ξ_0 determine the specific site characteristic parameters according to different site categories, parameters c and d reflect the time-domain non-stationary characteristics of the ground motion, parameters a and b reflect the non-stationary characteristics of the ground motion in the frequency domain, a_{\max} is the average value of the peak acceleration of the ground motion, and \bar{r} is the equivalent peak factor of the stationary vibration.

The non-stationary generalized power spectrum model of ground motion can thus be fully determined using 10 parameters. A suitable number of ground motion samples can be generated based on the modified evolutionary power spectrum model and the concept of the correlation spectrum form-random function. These samples have their own assigned probabilities, which is convenient for the stochastic dynamic analysis of slope under the stochastic dynamics framework. Relevant content can be found in the literature (Huang et al., 2018; Huang & Xiong, 2017a) (Fig. 2.4).

2.4.2 Ground Motion Synthesis Method Based on Stochastic Process Theory

The generation of representative time-history curves of stochastic processes is required to solve applied engineering problems that cannot be solved by the descriptor in the frequency domain. The methods of simulating and generating representative time-history curves of stochastic process mainly include the spectral representation method (harmonic superposition method), linear filtering method, eigen orthogonal decomposition method, and wavelet analysis method.

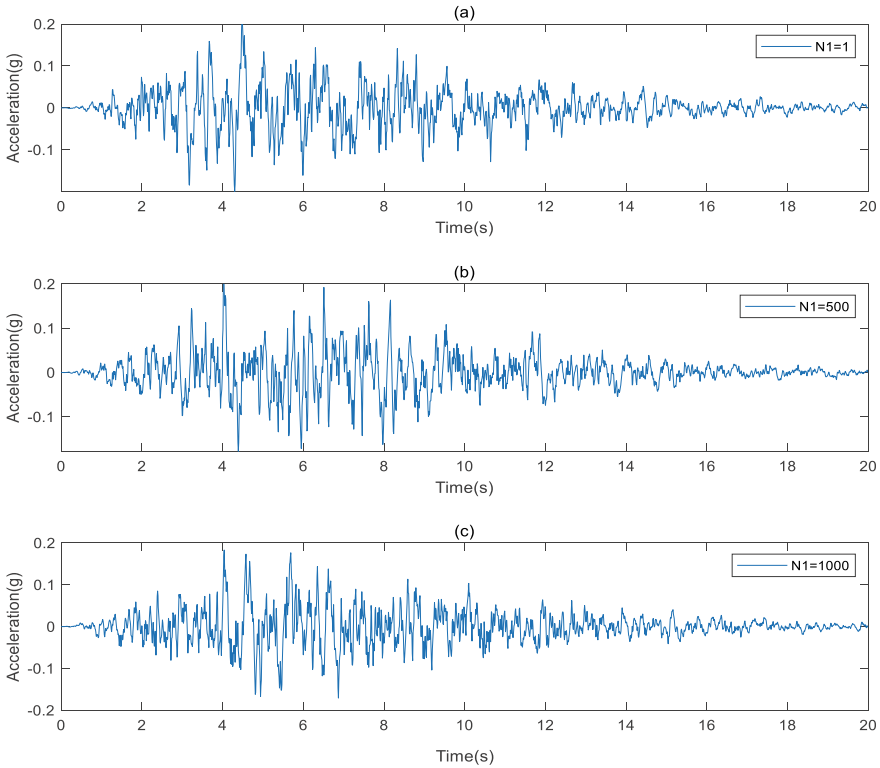


Fig. 2.4 Typical non-stationary seismic acceleration time series

(1) Spectral representation for ground motion synthesis

The spectral representation method is presently the most direct and relatively mature ground motion synthesis method. The random process of ground motion is the sum of a series of sine or cosine functions with a random phase, which is divided into the first and second spectral representation methods, as shown in Table 2.4.

The application of stochastic simulation research results in engineering practice began in the 1960s. The harmonic superposition method has been used to study and simulate the wave stochastic process but is limited to one-dimensional stochastic processes. To study multivariable non-stationary random processes, Shinozuka (1972) formally proposed the basic principle of the spectral representation method. Many scholars have thereafter carried out in-depth research on the spectral representation method, which is widely used in seismic engineering fields.

Yang (1972) proposed the expression formula of the random envelopment process and greatly improved the computational efficiency of the spectral representation method using the fast Fourier transform. Grigoriu (2000) proposed a harmonic superposition method with the random amplitude, frequency, and phase angle to generate time history samples with different periods. Shinozuka and Deodatis (1991) proposed

Table 2.4 Two spectral representation methods of ground motion acceleration process simulation

The first spectral representation method (Liang, 2005)	$X_a(t) = \sum_{k=1}^N A_{t,k} (\cos(\omega_k t) X_k + \sin(\omega_k t) Y_k)$ $A_{t,k} = \sqrt{2S_A((t, \omega_k)) \Delta\omega}; \omega_k = k \Delta\omega$
The second spectral representation method (Shinozuka & Deodatis, 1991)	$X_a(c) = \sqrt{2} \sum_{k=0}^{N-1} A_{t,k} \cos(\omega_k t + \varphi_k)$ $A_{t,k} = \sqrt{2S_A((t, \omega_k)) \Delta\omega}; \omega_k = k \Delta\omega$

Difference between the two kinds of spectrum representation methods

First spectral representation method— $2N$ orthonormal random variables: the random variable must only meet the orthonormal conditions and does not require a specific probability distribution form of the random variable

Second spectral representation method— N cosine series with mutually independent random phase angles: random variables must satisfy the condition of a mutually independent uniform distribution

Note $A_{t,k}$ is the power spectral density function of the random process, φ_k is the independent random phase angle, and ω_u is the truncation frequency, which is used to calculate the mean square relative error

the principle and mathematical expression formula of the spectral representation method (univariate and one-dimensional random process). After modifying the classical spectral representation of stationary stochastic processes, the population and time autocorrelation functions of the stochastic simulation processes can better maintain consistent convergence with the target self-correlation functions. Deodatis and Shinozuka (1989) evaluated the advantages and disadvantages of the spectral representation method in the random process of ground motion, further improved the spectral representation method, and simulated and generated the time-history samples of the earthquake ground motion acceleration stochastic process. Liang (2005) proposed a spectral representation method for simulating non-stationary random vibration processes from the perspective of a progressive power spectrum.

(2) Linear filtering method for ground motion synthesis

The linear filtering method, which can be referred to as the white noise filtering method, applies a random process abstraction to satisfy the certain condition of zero mean white noise, and the time domain model of the process is fitted by appropriate transformation of a hypothetical system. (see rational function of the PSD function in Eq. (2.40)). The theoretical basis include any smooth Gaussian random process that is available for use in the autoregressive moving average (ARMA) model, and the spectral density function can only be determined by the model structure. The ARMA model can represent the response value of a sample at the current moment as a linear combination of the response value of the sample at the past moment. The excitation value of the white noise can be regarded as a set of digital filters to transform the white noise into a discrete random process with an approximate target spectral density.

$$x(t) + \lambda x(t) = \xi(t) \quad (2.40)$$

$$E[\xi(t)\xi(\tau)] = 2\lambda\beta^2\delta(t - \tau) \quad (2.41)$$

Equation (2.40) presents a stochastic differential process of a linear system, where white noise $\xi(t)$ is taken as the input with filtered white noise $x(t)$ because the output, λ , is a constant associated with a random process, $x(t)$ is the time series generated by filtering, and $\xi(t)$ is a zero-mean Gaussian white noise process. Equation (2.41) is the condition for the covariance of Eq. (2.40) to be satisfied.

The linear filtering method can achieve the approximate representation of the target spectral density matrix with the least parameters, and the calculation speed is relatively fast. However, the model type, parameters, and order must be estimated, the algorithm is complicated, and the calculation accuracy is low, which limits the linear filtering method for engineering applications.

This chapter mainly provides an introduction to the PDEM and quantification method of slope uncertainty. The following chapters introduce the simulation, application, and verification of the slope stochastic dynamic analysis method in detail.

References

- Al-Homoud, & Tahtamoni. (2000). Reliability analysis of three-dimensional dynamic slope stability and earthquake-induced permanent displacement. *Soil Dynamics and Earthquake Engineering*, 19(2), 91–114.
- Al-Homoud, & Tahtamoni. (2001). A reliability based expert system for assessment and mitigation of landslides hazard under seismic loading. *Natural Hazards*, 24(1), 13–51.
- Amin, M., & Ang, A. (1968). Nonstationary stochastic models of earthquake motions. *Journal of the Engineering Mechanics Division, ASCE*, 94(EM2), 559–583.
- Aubry, N., Lian, W. Y., & Titi, E. S. (1993). Preserving symmetries in the proper orthogonal decomposition. *Siam Journal on Scientific Computing*, 14(2), 483–505.
- Bogdanoff, J. L., Goldberg, J. E., & Bernard, M. C. (1961). Response of a simple structure to a random earthquake-like disturbance. *J Bulletin of the Seismological Society of America*, 51(2), 293–310.
- Bolotin. (1960). Statistical theory of the aseismic design of structures *Proceedings of the 2nd World Earthquake Engineering*, 1365–1374.
- Boyadjiev, T. L. (1975). Variational principle for Fokker-Planck-Kolmogorov equation. *Dokladi Na Bolgarskata Akademiya Na Naukite*, 28(12), 1587–1589.
- Cacciola, P., & Deodatis, G. (2011). A method for generating fully non-stationary and spectrum-compatible ground motion vector processes. *Soil Dynamics and Earthquake Engineering*, 31(3), 351–360.
- Carassale, L., & Solari, G. (2006). Monte Carlo simulation of wind velocity fields on complex structures. *Journal of Wind Engineering and Industrial Aerodynamics*, 94(5), 323–339.
- Chen, J. B., & Li, J. (2009). A note on the principle of preservation of probability and probability density evolution equation. *Probabilistic Engineering Mechanics*, 24(1), 51–59.
- Chen, X. Z., & Kareem, A. (2005). Proper orthogonal decomposition-based modeling, analysis, and simulation of dynamic wind load effects on structures. *Journal of Engineering Mechanics*, 131(4), 325–339.
- Cho, S. E. (2010). Probabilistic assessment of slope stability that considers the spatial variability of soil properties. *Journal of Geotechnical and Geoenvironmental Engineering*, 136(7), 975–984.
- Clough, & Penzien. (1975). *Dynamics of Structures*. McGraw-Hill.

- Cornell, C. A. (1960). Stochastic Process Models in Structural Engineering. *Technical Report*.
- Cusumano, J. P., & Bai, B. Y. (1993). Period-infinity periodic motions, chaos, and spatial coherence in a 10 degree-of-freedom impact oscillator. *Chaos Solitons & Fractals*, 3(5), 515–535.
- Deodatis, G. (1996). Non-stationary stochastic vector processes: Seismic ground motion applications. *Probabilistic Engineering Mechanics*, 11(3), 149–167.
- Deodatis, G., & Shinozuka, M. (1989). Simulation of seismic ground motion using stochastic waves. *Journal of Engineering Mechanics-Asce*, 115(12), 2723–2737.
- DiPaola, M., & Pisano, A. A. (1996). Multivariate stochastic wave generation. *Applied Ocean Research*, 18(6), 361–365.
- Du, X. L., & Chen, H. Q. (1994a). Random simulation of ground motion and its parameter determination method. *Earthquake Engineering and Engineering Vibration*, 14(14), 11–15.
- Du, X. L., & Chen, H. Q. (1994b). Random simulation of ground motion and its parameter determination method [J]. Earthquake engineering and engineering vibration. *Earthquake engineering and Engineering Vibration*, 14(4), 1–5.
- Ghiocel, D. M., & Ghanem, R. G. (2002). Stochastic finite-element analysis of seismic soil-structure interaction. *Journal of Engineering Mechanics-Asce*, 128(1), 66–77.
- Goldberg, J. E., Bogdanoff, J. L., & Sharpe, D. R. (1964). The response of simple nonlinear systems to a random disturbance of the earthquake type. *Bulletin of the Seismological Society of America*, 54(51), 263–276.
- Griffiths, D. V., Huang, J., & Fenton, G. A. (2009). Influence of spatial variability on slope reliability using 2-D random fields. *Journal of Geotechnical and Geoenvironmental Engineering*, 135(10), 1367–1378.
- Grigoriu, M. (2000). A spectral representation based model for Monte Carlo simulation. *Probabilistic Engineering Mechanics*, 15(4), 365–370.
- Grigoriu, M. (2004). Spectral representation for a class of non-Gaussian processes. *Journal of Engineering Mechanics*, 130(5), 541–546.
- Gullo, I., Di Paola, M., & Spanos, P. D. (1998). Spectral approximation for wind induced structural vibration studies. *Meccanica*, 33(3), 291–298.
- Hong, F., Jiang, J. R., & Li, Y. T. (1994). Power spectrum model of earthquake ground motion and determination of its parameters. *Earthquake Engineering and Engineering Vibration*, 4(2), 46–51.
- Housner. (1947). Characteristics of strong-motion earthquakes. *Bulletin of the Seismological Society of America*, 37(1), 19–31.
- Hu, C. Y., & Chen, Q. J. (2008). Research on bi-modulation model of non-stationary earthquake ground Motion. *Chinese quarterly of mechanics*, 29(4), 530–536.
- Hu, Y. X., & Zhou, X. Y. (1962). Response of elastic system under steady and stabilized ground motion [a]. Collection of research reports on seismic engineering. *Beijing: Science Press*, pp. 33–50.
- Huang, Y., Hu, H., & Xiong, M. (2018). Probability density evolution method for seismic displacement-based assessment of earth retaining structures. *Engineering Geology*, 234, 167–173.
- Huang, Y., Hu, H., & Xiong, M. (2019). Performance-based seismic fragility analysis of retaining walls based on the probability density evolution method. *Structure and Infrastructure Engineering*, 15(1), 103–112.
- Huang, Y., & Xiong, M. (2017a). Dynamic reliability analysis of slopes based on the probability density evolution method. *Soil Dynamics and Earthquake Engineering*, 94, 1–6.
- Huang, Y., & Xiong, M. (2017b). Probability density evolution method for seismic liquefaction performance analysis of earth dam. *Earthquake Engineering & Structural Dynamics*, 46(6), 925–943.
- Jiang, S. H., Huang, J., & Zhou, C. B. (2017). Efficient system reliability analysis of rock slopes based on Subset simulation. *Computers and Geotechnics*, 82, 31–42.
- Johari, A., & Khodaparast, A. R. (2015). Analytical stochastic analysis of seismic stability of infinite slope. *Soil Dynamics and Earthquake Engineering*, 79, 17–21.

- Kameda. (1975). Evolutionary spectra of seismogram by multifilter. *Journal of the Engineering Mechanics Division-Asce*, 101(6), 787–801.
- Kim, J. M., & Sitar, N. (2013). Probabilistic evaluation of seismically induced permanent deformation of slopes. *Soil Dynamics and Earthquake Engineering*, 44, 67–77.
- Kramer, S. L., & Paulsen, S. B. (2004). Seismic performance evaluation of reinforced slopes. *Geosynthetics International*, 11(6), 429–438.
- Lai, M., Ye, T. Y., & Li, Y. M. (1995). Double filtered white noise model of ground motion. *Journal of Civil Engineering*, 28(26), 60–66.
- Liang, J. W. (2005). Simulation of non-stationary ground motion processes (I). *Acta Seismologica Sinica*, 27(2), 213–224.
- Lumley. (1967). The structure of inhomogeneous turbulent flows. *Proceedings International Coll. on the Fine Scale Structure of the Atmosphere and its Influence on Radio Wave Propagation, Doklady Akademia Nank SSSR, Moscow*, pp. 166–176.
- Masri, S. F., Smyth, A. W., & Traina, M. I. (1998). Probabilistic representation and transmission of nonstationary processes in multi-degree-of-freedom systems. *Journal of Applied Mechanics-Transactions of the Asme*, 65(2), 398–409.
- Matsuda, & Asano. (2006). Analytical expression of earthquake input energyspectrum based on spectral density model of ground acceleration. *Proceeding of the 8th U. S. National Conference on Earthquake Engineering*.
- Matsushima. (1986). A study on the orchid of a single degree of freedom system. [A]. Proceedings of the Department of architecture. *Japan Architectural Society*, 369, 342–346.
- Montoya-Noguera, S., Zhao, T., Hu, Y., et al. (2019). Simulation of non-stationary non-Gaussian random fields from sparse measurements using Bayesian compressive sampling and Karhunen-Loeve expansion. *Structural Safety*, 79, 66–79.
- Nour, A., Slimani, A., Laouami, N., et al. (2003). Finite element model for the probabilistic seismic response of heterogeneous soil profile. *Soil Dynamics and Earthquake Engineering*, 23(5), 331–348.
- Ou, J. P., & Wang, G. Y. (1998). Random vibration of structures *Beijing: Higher Education Press*.
- Pang, R., Xu, B., Kong, X., et al. (2018a). Seismic reliability assessment of earth-rockfill dam slopes considering strain-softening of rockfill based on generalized probability density evolution method. *Soil Dynamics and Earthquake Engineering*, 107, 96–107.
- Pang, R., Xu, B., Zou, D., et al. (2018b). Stochastic seismic performance assessment of high CFRDs based on generalized probability density evolution method. *Computers and Geotechnics*, 97, 233–245.
- Peng, H. S., Deng, J., & Gu, D. S. (2005). Earth slope reliability analysis under seismic loadings using neural network. *Journal of Central South University of Technology*, 12(5), 606–610.
- Phoon, K. K., Huang, H. W., & Quek, S. T. (2005). Simulation of strongly non-Gaussian processes using Karhunen-Loeve expansion. *Probabilistic Engineering Mechanics*, 20(2), 188–198.
- Rathinam, M., & Petzold, L. R. (2003). A new look at proper orthogonal decomposition. *Siam Journal on Numerical Analysis*, 41(5), 1893–1925.
- Rathje, E. M., Kottke, A. R., & Trent, W. L. (2010). Influence of input motion and site property variabilities on seismic site response analysis. *Journal of Geotechnical and Geoenvironmental Engineering*, 136(4), 607–619.
- Ruiz, & Penzien. (1969). Probabilistic study of the behavior of structures during earthquakes. *Earthquake Engineering Research Center*.
- Schuellër, G. I. (1997). Special issue—a state-of-the-art report on computational stochastic mechanics—preface. *Probabilistic Engineering Mechanics*, 12(4), 197–321.
- Shinozuka. (1972). Monte Carlo solution of structural dynamics. *Computers and Structures*, 2(5–6), 855–874.
- Shinozuka, M., & Deodatis, G. (1991). Simulation of stochastic processes by spectral representation. *Applied Mechanics Reviews*, 44(4), 191–204.
- Strenk, P. M., & Wartman, J. (2011). Uncertainty in seismic slope deformation model predictions. *Engineering Geology*, 122(1–2), 61–72.

- Tajimi. (1960). Statistical Method of Determining the Maximum Response of a Building During an Earthquake.
- Tsompanakis, Y., Lagaros, N. D., Psarropoulos, P. N., et al. (2010). Probabilistic seismic slope stability assessment of geotechnical structures. *Structure and Infrastructure Engineering*, 6(1–2), 179–191.
- Tubino, F., Carassale, L., & Solari, G. (2003). Seismic response of multi-supported structures by proper orthogonal decomposition. *Earthquake Engineering & Structural Dynamics*, 32(11), 1639–1654.
- Vorechovsky, M. (2008). Simulation of simply cross correlated random fields by series expansion methods. *Structural Safety*, 30(4), 337–363.
- Wu, X. Z. (2015). Development of fragility functions for slope instability analysis. *Landslides*, 12(1), 165–175.
- Yang, J. N. (1972). Simulation of random envelope process. *Journal of Sound and Vibration*, 26(3), 417–428.
- Zhu, W. Q. (2003). *Nonlinear stochastic dynamics and control: Framework of Hamilton theory system*. Science Press.

Chapter 3

Numerical Simulation and Application of Slope Stochastic Seismic Response Analysis



Numerical analysis methods are based on theoretical research, and are currently the most common analysis tool owing to their efficient and accurate calculations. Numerical analysis can effectively reproduce the dynamic response process of slopes and be used to quickly obtain the data response of any unit body at any time. It is therefore the most common method to study the random dynamic stability of slopes. This chapter uses numerical simulations to study and analyze the random dynamic stability of slopes based on the theoretical introduction in the previous chapter.

Earthquakes are important natural phenomena that can induce slope failure and have always been a hotspot in slope stability analysis and seismic engineering design research (Del Gaudio & Wasowski, 2004). The traditional quantitative analysis methods of seismic slope stability are all based on deterministic theory, which regards the factors affecting slope instability as definite and homogeneous, such as the strength reduction method (Wang et al., 2016). However, many factors have large uncertainties that affect slope stability, such as the physical properties of the geotechnical materials and ground motion intensity (Huang et al., 2020). The use of the deterministic method to calculate and analyze slope stability produces substantial errors. However, reliability theory makes it possible to quantitatively consider these uncertain factors (Chen et al., 2018; Liu & Cheng, 2018). The slope seismic analysis method based on reliability theory regards the uncertain factors that affect slope stability as stochastic variables. The stability is then determined using deterministic analysis methods, such as the limit equilibrium method. The reliability index is calculated by the reliability solution method to obtain the slope reliability analysis and evaluation results. The most commonly used method for reliability solution is the Monte Carlo method. The evaluation index system based on uncertainty analysis therefore covers the stability coefficient under the theoretical framework of certainty, and can provide a better basis for engineering decision-making.

The commonly used methods of slope dynamic stability analysis include the pseudo-static method, Newmark slider displacement method, and stochastic vibration method. The pseudo-static method has the advantages of simplicity and practicality, but cannot consider the nonlinear dynamic behavior of soil mass, the non-stationary strength-frequency features of seismic oscillation, and the on-site amplification effects (Lin & Wang, 2006). The Newmark slider displacement method partially considers the spectral characteristics of seismic oscillation and the nonlinear mechanical behavior of soil. However, this method assumes that the slope soil is rigid and plastic, and that the soil strength is not significantly reduced during an earthquake. This is far from the real situation and does not fully reflect the true nonlinear dynamic behavior of a slope in an earthquake event. Although these two methods are simple and quick to calculate, they are too simplified to approximate actual situations, thus leading to errors in the analysis results. A method based on the stochastic theory of dynamic reliability can therefore be used to avoid the aforementioned shortcomings.

This chapter proposes a slope reliability analysis method based on the probability density evolution method (PDEM). This approach uses the nonlinear dynamic time history analysis method for calculation, and the nonlinear elastoplastic constitutive model and ground motion time history curve are input as random variables in the reliability analysis.

3.1 Slope Stochastic Seismic Analysis Methods

3.1.1 Slope Dynamic Stability Analysis Method

(1) Finite element sliding surface stress method

The nonlinear dynamic time history analysis method calculates the changes of each particle's velocity, acceleration, and displacement with time to obtain the time history response of the slope internal force, deformation, and safety factor. This section considers the nonlinear mechanical behavior of soil.

The finite element method (FEM) is used as an example to introduce the numerical calculation process of the nonlinear dynamic time history analysis method. The finite element sliding surface stress method has the advantages of fast calculation speed and the ability to simultaneously determine the sliding surface position and its stress and strain state, and is thus adopted in this section. This method calculates the stress field through the FEM and integrates the entire sliding surface to obtain the shear strength and sliding shear stress on the sliding surface. The piecewise linear fitting method is typically used for complex stress fields to avoid the difficulty of solving the integral by simulating the sliding surface of an arbitrary shape (Zou et al., 1995).

There are presently many FEM applications, including ANSYS, ABAQUS, FLAC3D, and GeoStudio. For a simple and rapid calculation, this book uses

GeoStudio software, which can use the finite element slip surface stress method and integrate modules (e.g., SLOPE/W, SIGMA/W, QUAKE/W) to perform dynamic, static stress, and deformation analysis of slopes and seismic response analysis. The specific steps to analyze the dynamic stability of a slope are as follows.

- a. In the QUAKE/W module, the FEM is used to calculate the stress field under the influence of the initial dead weight. The calculation results are imported into the next step of dynamic analysis.
- b. In the QUAKE/W module, the dynamic time history method is used to compute the stress field at each time step based on the initial stress field distribution. The calculation results are then imported into the SLOPE/W module.
- c. In the SLOPE/W module, the potential sliding block is first divided into several soil strips. In the light of the inclination angle of the bottom sliding surface of each soil strip and the finite element mesh that passes through, the shear strength and sliding stress of the bottom of the soil strip are calculated in combination with the stress field under the dynamic time step. All the soil strips are then summed to obtain the strength of the entire potential sliding surface.

Owing to the inhomogeneity of the slope stress distribution and complexity of the spectral characteristics of ground motion excitation, there are multiple potential sliding surfaces with different safety factors at each time step. The sliding surface corresponding to the minimum safety factor is typically of greatest interest, which is also called the critical sliding surface. In the SLOPE/W module, the software can automatically search for the critical slip surface at each time step and calculate its corresponding safety factor in combination with the optimization program. The safety factor of the critical slip surface at each time step can thus be calculated.

(2) Nonlinear constitutive model of soil

To consider the nonlinear mechanical behavior of soil materials, this book chooses the nonlinear dynamic constitutive model in the QUAKE/W module.

The dynamic stress–strain relationship of soil is described by a hyperbola ((Xu & Huang, 2021), and its curve equation can be defined by two parameters, G_{max} and τ_{max} , where the former is called the small-strain shear modulus, which is the shear modulus when the shear strain is zero, and the latter represents the horizontal asymptote of the main line in the longitudinal direction. The physical meaning of the intercept on the axis is maximum shear stress at failure, and $\gamma_r = \tau_{max}/G_{max}$ is the reference strain of the soil. The equation of the backbone can be written as:

$$\tau = \frac{\gamma}{\frac{1}{G_{max}} + \frac{\gamma}{\tau_{max}}} = \frac{G_{max}\gamma}{1 + \frac{\gamma}{\gamma_r}} \quad (3.1)$$

We next consider the mathematical expression of the hysteresis curve. The most commonly used assumption is that the hysteresis curve follows the massing criterion. This criterion assumes that the hysteresis curve can be obtained by the translation and enlargement of the main trunk line. The equations of unloading and reverse loading according to this criterion can be written as:

$$\tau = \tau_A + \frac{G_{max}(\gamma - \gamma_A)}{1 + \frac{\gamma - \gamma_A}{\gamma_r^{ABC}}} \quad (3.2)$$

where τ_A is the shear stress, γ_A is the shear strain at the unloading starting point, γ_r^{ABC} is the reference strain of the trajectory of unloading and reverse loading, and $\gamma_r^{ABC} = 2\gamma_r$. Equation (3.2) can be further written as:

$$\tau = \tau_A + \frac{G_{max}(\gamma - \gamma_A)}{1 + \frac{\gamma - \gamma_A}{2\gamma_r}} \quad (3.3)$$

In the same way, the reverse unloading and forward loading trajectory equations can be written as:

$$\tau = \tau_C + \frac{G_{max}(\gamma - \gamma_C)}{1 + \frac{\gamma - \gamma_C}{2\gamma_r}} \quad (3.4)$$

where τ_C and γ_C are the shear stress and shear strain at the starting point of the reverse unloading, respectively.

In the hyperbolic dynamic constitutive model, the maximum shear stress T_{max} is usually obtained approximately according to the Mohr–Coulomb failure theory. The constitutive model therefore only requires the effective shear parameters of the soil c' , φ' , and the small strain shear modulus G_{max} . An empirical estimation formula of G_{max} is provided in the QUAKE/W module. Taking clay as an example, the expression is:

$$G_{max} = 625 \left(\frac{1}{0.3 + 0.7e^2} \right) (OCR)^k \sqrt{P_a \sigma'_m} \quad (3.5)$$

where P_a is the atmospheric pressure, σ'_m is the average effective principal stress, OCR is the over-consolidation ratio, e is the void ratio, and k is connected with the plasticity index PI , which can be calculated as:

$$k = \frac{PI^{0.72}}{50} \quad (3.6)$$

3.1.2 Finite Element Reliability Analysis Framework Based on PDEM

Section 3.1.1 introduced the calculation process of the dynamic FEM of the slope. This section mainly presents the integration of slope reliability analysis based on

PDEM and slope dynamic stability analysis calculated using GeoStudio software. The specific calculation procedures are summarized as follows.

- a. Probability space division of random variables. After determining the number of basic random variables, select points, using tangent ball or number theory (Chen & Li 2006a, b), determine the number of discrete points n_{sel} , and calculate their distribution probability. By dividing and selecting points in the continuous probability space, the random problem is transformed into an n_{sel} deterministic problem represented by discrete representative points.
- b. Create a seismic dynamic analysis model in the QUAKE/W module and SLOPE/W module with the parameter mean value of the stochastic variable, including geometric model establishment, finite element area and grid division, material definition, finite element area material assignment, ground motion input, boundary condition definition, sliding surface inlet and outlet position setting, and model verification steps. Owing to the spatial variability of the soil physical properties, the grids must be defined with the same size and position as the stochastic field unit in the finite element model to ensure a one-to-one correspondence of the stochastic field units and finite element unit. Save the complete finite element dynamic analysis model as a calculation source file with the extension “.xml”.
- c. For different stochastic sources in a slope system subjected to seismic dynamic excitation, adopt the Karhunen-Loève (K-L) series expansion method to simulate the anisotropic stochastic field of the soil parameters. The spectral representation method and stochastic function are used to express the non-stationarity and stochasticity of the seismic excitation and generate the ground motion time histories. The stochastic fields are consistent with the number n_{sel} of generated scattered points in probability space. The “.xml” file is a structured markup language, which stores all the information of the slope seismic dynamic finite element analysis model (e.g., area size, grid coordinates, material parameters, load records, and boundary constraints). Find the material parameters and load records, use programming language to write a program to modify them in batches, and save the modified “.xml” file as a new calculation file.
- d. Use the cmd.exe command line program that comes with the Windows system and the DOS operating system to write a batch program that can automatically calculate multiple “.xml” files.
- e. After the batch calculation is completed, multiple folders corresponding to the calculation time steps will be generated under the SLOPE/W module of each “.xml” file. Find the file titled “slip_surface.csv” in the folder, from which the critical safety factor, sliding surface, and other information in the current time step can be extracted.
- f. Substitute a series of deterministic analysis and calculation results into the generalized probability evolution equation (GDEE), and use the finite difference numerical method for its solution. Calculate the probability density function (PDF) curve, cumulative distribution function (CDF) curve, and dynamic reliability of the slope stochastic system.

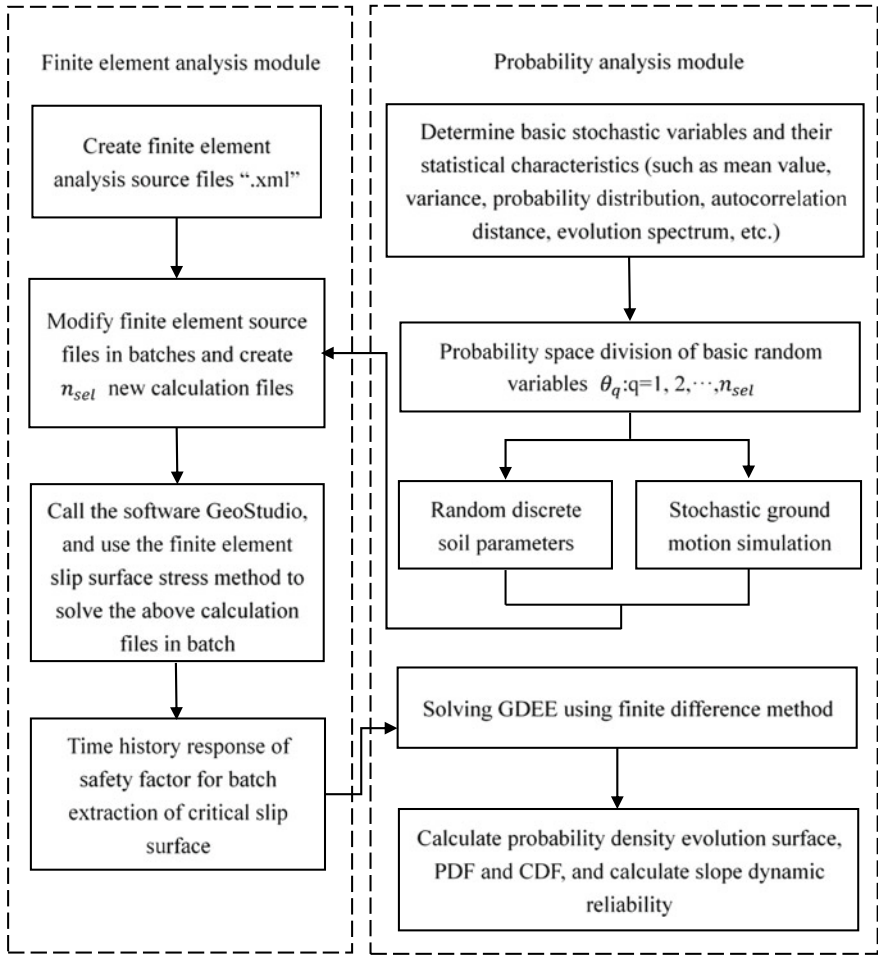


Fig. 3.1 Flow chart of slope reliability analysis using the PDEM

Figures 3.1 summarizes the slope seismic dynamic reliability calculation process based on the PDEM and FEM.

3.2 Description of Stochastic Factors of Slope

The uncertainties of slope systems originate from the spatial variabilities of the soil parameters and seismic motion excitations. Earthquakes have strong stochasticity in terms of space, time, and magnitude. Numerous studies (Johari & Khodaparast, 2015; Mahdiyari et al., 2017; Wu et al., 2015) have considered the stochastic

nature of the seismic spectral characteristics in slope reliability analysis. However, the current considerations of earthquake activity mostly use the pseudo-static method. This approach can neither determine the response of the non-stationary characteristics of seismic samples nor describe the nonlinear mechanical behavior of soil under seismic motion. The reliability analysis method is illustrated by the theory of probability and statistics, which can consider the randomness of multiple physical parameters for seismic slope stability analysis. The use of the non-linear dynamic time history method to analyze seismic dynamics is therefore necessary, through which the randomness of the geotechnical parameters and ground motion spectrum parameters are considered for reliability analysis.

3.2.1 Generation of Stochastic Fields

Differing from general building materials, soil is a natural product that forms under long-term geological action and is subjected to a range of different physical, chemical, and natural environmental effects during its formation process. Soil parameters often have spatial variability, which is manifested in the form of different physical characteristics at different points in the soil with a certain correlation between points. The spatial variability of soil has a great influence on its properties, and is an irreplaceable factor in slope reliability analysis and assessment.

In the initial stages of slope reliability analysis and research, only the influence of stochastic fields and parameter anisotropy was considered on the predetermined dangerous sliding surface. The common method is to divide the sliding surface in each soil layer, consider the local average value of the parameters in each section as a random variable, and determine the anisotropic characteristics of the soil mechanical parameters by describing the correlation between the random variables (Cho, 2007; El-Ramly et al., 2002; Li & Lumb, 1987). The main drawback of this method is that the stochastic field is one-dimensional and the soil parameter anisotropy cannot be considered. Although this approach of considering the stochastic field only on the sliding surface is easily calculated, it oversimplifies the actual situation and is highly unreasonable.

The spatial variability of soil physical characteristics means that the soil physical quantity at different locations in space can be regarded as random variables. A more reasonable stochastic field simulation method therefore involves the discretization of the soil parameters in the entire research object area. The discrete stochastic field parameters are then assigned to the corresponding finite element grid to perform reliability analysis considering soil anisotropy (Cho, 2009; Griffiths et al., 2009; Jha, 2015). Because the K-L series expansion method has high simulation accuracy and fast discrete efficiency, this section considers the anisotropy of the soil physical properties and uses the K-L series expansion method for calculation and simulation.

(1) **Simulation of relevant non-normal stochastic field**

The simulation steps of related non-normally distributed stochastic fields are summarized as follows.

- a. Divide the stochastic field into a finite element grid. For calculation simplicity, the stochastic field unit grid is generally consistent with the finite element unit grid, and the coordinates of the center point of each grid are calculated.
- b. Compute the eigenvalue λ_i and eigenvector $\varphi_i(x)$ of the autocorrelation function. According to Eq. (3.7), select the autocorrelation function form under the condition of a two-dimensional stochastic field, use Eq. (3.8) to calculate the corresponding eigenvalues and eigenvectors, and arrange them in descending order of eigenvalues.

$$\rho(x, x') = \begin{cases} \exp\left(-\frac{|x-x'|}{l}\right), & (a) \\ \exp\left(-\frac{|x-x'|}{l_x} - \frac{|y-y'|}{l_y}\right), & (b) \end{cases} \quad (3.7)$$

$$\int_{\Omega} \rho(x, x') \varphi_i(x') d\Omega_{x'} = \lambda_i \varphi_i(x) \quad (3.8)$$

where l is the relative distance of the one-dimensional stochastic field, x and x' are the coordinates of any two points in the one-dimensional stochastic field, (x, y) and (x', y') are the coordinates of any two points in the two-dimensional stochastic field, and l_x and l_y are the relative distances in the horizontal and vertical directions in a two-dimensional stochastic field, respectively. Equations (3.7a) and (3.7b) are suitable for one- and two-dimensional stochastic fields, respectively.

- c. Generate the independent standard Gaussian random variable $\xi_{k,i}(\theta)$. Latin hypercube sampling technology can be applied to effectively ensure the uniformity and completeness of the standard normal random variables.
- d. Consider the correlation between soil physical parameters. According to Eq. (3.10), calculate the mutual correlation coefficient matrix in the Gaussian distribution, as shown in Eq. (3.9). Use Cholesky factorization to acquire the lower triangular matrix L , and multiply it by the independent Gaussian random variables $\xi_{k,i}(\theta)$ to acquire the relevant Gaussian stochastic variables $\chi_{k,i}(\theta)$.

$$R_{0c,\varphi} = (\rho_{0ij})_{2 \times 2} = \begin{pmatrix} 1 & \rho_{0c\varphi} \\ \rho_{0c\varphi} & 1 \end{pmatrix} \quad (3.9)$$

$$\rho_{0ij} = \frac{\ln(\rho_{ij} COV_{X_i} COV_{X_j} + 1)}{\sqrt{\ln(1 + COV_{X_i}^2)} \sqrt{\ln(1 + COV_{X_j}^2)}} \quad (3.10)$$

$$\chi_{k,i}(\theta) = \xi_{k,i}(\theta) \cdot L^T k = c, \varphi \quad (3.11)$$

where COV_{X_i} is the coefficient of variation of X_i , and COV_{X_j} is the coefficient of the variation of X_j .

- e. Correlated non-normal stochastic field $\widehat{H}_k^{CNN}(x, \theta)$ simulation. According to the mean value, variance, and probability distribution type of the soil parameter stochastic field, the relevant non-normal stochastic field is obtained using the equal probability transformation formula and calculated as follows:

$$\widehat{H}_k^{CNN}(x, \theta) = G_i^{-1} \left\{ \Phi[\widehat{H}_k^C(x, \theta)] \right\} \quad (3.12)$$

$$\widehat{H}_k^C(x, \theta) = \exp \left(\mu_{lnk}(x) + \sum_{i=1}^n \sigma_{lnk}(x) \sqrt{\lambda_i} \varphi_i(x) \chi_{k,i}(\theta) \right) \quad k = c, \varphi \quad (3.13)$$

where $\widehat{H}_k^C(x, \theta)$ represents the correlated normal stochastic field, G_i^{-1} is the inverse function of the marginal CDF of $\widehat{H}_k^C(x, \theta)$, $\Phi(\cdot)$ is the CDFs of the standard Gaussian variables, and $\mu_{lnk}(x)$ and $\sigma_{lnk}(x)$ are the average value and standard deviation of the stochastic variables, respectively, which obey a Gaussian distribution.

- f. Combining the probability space division of basic random variables, repeat steps b–e n_{sel} times to obtain the n_{sel} realization of the relevant non-normal stochastic field, and calculate the corresponding assigned probability.

(2) Stochastic field simulation results

This chapter selects the clay slope introduced by (Cho, 2010) as the research object. A 10-m-high soil slope model is used, as shown in Fig. 3.2. The stochastic field

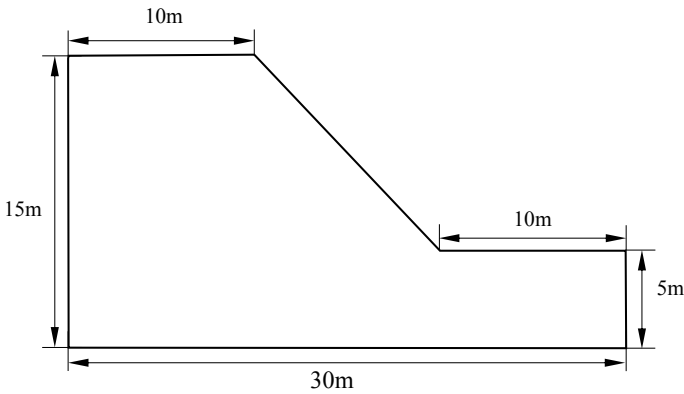


Fig. 3.2 Slope geometry for reliability analysis

model is applied to describe the anisotropy of the soil physical and mechanical properties, and c and φ are regarded as basic stochastic variables. In slope seismic engineering, it is impossible to measure all parameter values at each point in soil space. Stochastic field simulations are generally carried out based on the parameter statistics of a limited number of sample points. The example in this chapter uses an average cohesion value of 10 kPa with a coefficient of variation of 0.3. The mean value of the internal friction angle is 30° and the coefficient of variation is 0.2. Both probability distributions follow a lognormal distribution. Because soil is an anisotropic material, the horizontal and vertical autocorrelation distances differ. This is reflected in the stochastic field, in which the horizontal autocorrelation distance is considerably longer than the autocorrelation distance in the vertical direction, and the difference between the two is generally an order of magnitude. Therefore, in this chapter, the autocorrelation distance is set to 20 m in the horizontal direction, 2 m in the vertical direction, and the cross-correlation coefficient is -0.5 .

According to the stochastic field simulation process described above, the mesh of the stochastic field cells must be first divided. Combined with the finite element analysis model, the model established in this book has a total of 1281 nodes and 1210 elements. Among them, the triangular elements are mainly located near the empty surface of the slope as the transition element body, as shown in Fig. 3.3.

The number of truncation terms n is highly critical when performing stochastic field discretization. If n is too small, it will lead to insufficient calculation accuracy; if n is too large, the computation amount will grow exponentially. The truncation value of n commonly rests with the computational precision and autocorrelation function. This chapter selects $n = 150$, as suggested in the literature (Cho, 2010).

The mean values of the soil parameters c and φ are used for modeling, and a discrete simulation of the related non-normal stochastic field is carried out according to Eq. (3.13). Figure 3.4 shows a typical realization. The value of c clearly fluctuates around the mean owing to the location changes. This is much closer to the actual

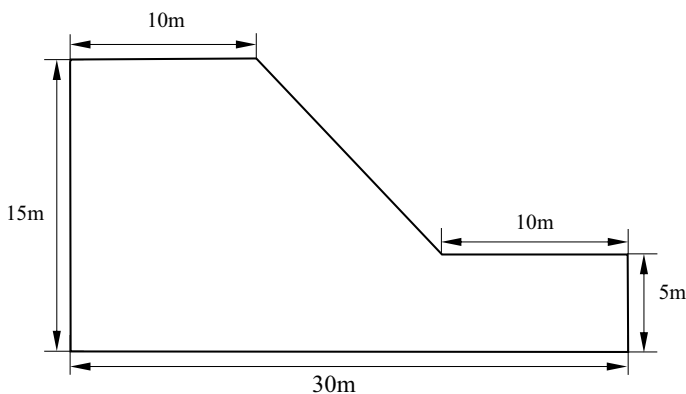


Fig. 3.3 Finite element model of a slope for reliability analysis

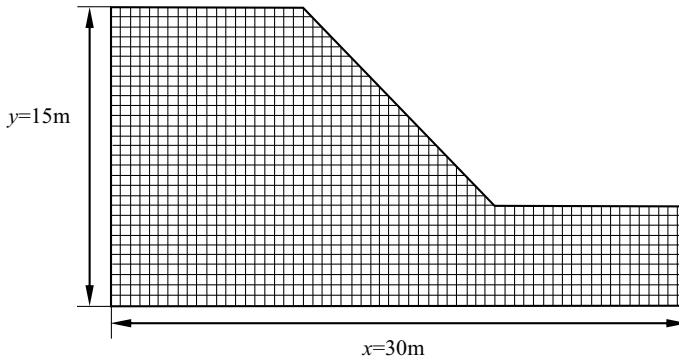


Fig. 3.4 Typical realization of cohesion stochastic field

distribution of soil physical and mechanical parameters. According to the consequences of the tangent sphere of the two basic random variables, the stochastic fields are sequentially discretized using different statistical eigenvalues of c and φ , and 127 sets of non-normal stochastic fields related to the soil parameters are obtained. With limited statistical information, these 127 stochastic fields are used to approximately replace the true distribution of the soil parameters.

3.2.2 Stochastic Seismic Ground Motion Model

Existing ground motion observation records have shown that earthquakes exhibit notably non-stationary characteristics owing to the complex and uncertain conditions, such as the focal mechanism, propagation path, and engineering site characterization. This non-stationary characteristic is manifested in the time domain as follows. The ground motion will sequentially go through (1) an initial increasing intensity phase, (2) a strong earthquake phase with a stable intensity region, and (3) an attenuation phase of gradually weakening intensity, which is called the non-stationary intensity. The performance in the frequency domain is as follows. Ground motions at different frequencies moments have different vibration energies, which are called non-stationary frequencies characteristics. Secondary hazards (e.g., damage accumulation and resonance effects) are common in geotechnical engineering works (e.g., slopes) owing to the non-stationary ground motion characteristics, which has a serious effect on the seismic response of slope engineering and structures. The non-stationary characteristics of the ground motion intension and frequency should therefore be reasonably considered when establishing the ground motion model. Furthermore, the future ground motions of a slope site should be used as the load input when performing seismic slope reliability analysis. However, the location and vibration characteristics of future ground motions are difficult to predict and exhibit randomness.

This section uses the modified Clough-Penzien power spectrum model to express the intensity-frequency non-stationary features of ground motions. A stochastic ground motion model is established using the spectral representation-stochastic function method, and a series of ground motion acceleration sample time histories are generated.

(1) Stochastic ground motion simulation

The method of establishing the generalized evolution PSD function is introduced in Sect. 2.4.1. Equations (2.34)–(2.39) indicate that the generalized power spectrum model for fully non-stationary ground motion is completely determined by 10 parameters. Among these, parameters a and b indicate the non-stationary characteristics of ground motions in the frequency-domain, parameters c , d , and n express the non-stationary characteristics of ground motions that change over time, parameters ω_0 and ξ_0 reflect the characteristics of the site, and parameters \bar{a}_{max} , \bar{r} , and T together reflect the amplitude and duration characteristics of the seismic motions.

Appropriate essential stochastic variables are then chosen using the generalized evolution power spectrum to represent the earthquake randomness, and the non-stationary seismic motion is simulated by applying the spectrum representation-stochastic function method (Liu et al., 2015a, b). Considering the non-stationary seismic motion stochastic process, the mean value of $\ddot{X}_g(t)$ is zero, and the expression of the first type of spectrum can be written as:

$$\ddot{X}_g(t) \approx \sum_{k=1}^N \sqrt{2S_{\ddot{X}_g}(t, \omega_k) \Delta\omega} [\cos(\omega_k t) X_k + \sin(\omega_k t) Y_k] \quad (3.14)$$

where $\omega_k = k\Delta\omega$ and requires that the frequency difference is sufficiently small, and X_k and Y_k are standard orthogonal stochastic variables that satisfy the following conditions:

$$\begin{aligned} E[X_i] &= E[Y_i] = 0 \\ E[X_i Y_j] &= 0 \\ E[X_i X_j] &= E[Y_i Y_j] = \delta_{ij} \end{aligned} \quad (3.15)$$

For the sake of reducing the quantity of standard orthogonal random variables $\{X_k, Y_k\}$, the concept of a stochastic function (Tang & Liu, 2011) is adopted to express the normal orthogonal random variables as functions of the essential stochastic variables. Considering that the ground motion stochastic system is composed of a single basic random variable Θ , the stochastic function can be written as:

$$\bar{X}_n = \sqrt{2} \cos\left(k\Theta + \frac{\pi}{4}\right), \bar{Y}_n = \sqrt{2} \sin\left(k\Theta + \frac{\pi}{4}\right) \quad (3.16)$$

Among them, the basic stochastic variable Θ obeys a homogeneous distribution on the interval $[-\pi, \pi]$. The standard orthogonal random variable $\{\bar{X}_n, \bar{Y}_n\}$ clearly satisfies Eq. (3.15). Note that in Eq. (3.14), the expansion of the generalized evolution power spectrum follows a certain order of energy, which leads to a certain difference in the order of the standard orthogonal random variables $\{X_k, Y_k\}$ and $\{\bar{X}_n, \bar{Y}_n\}$. Therefore, $\{\bar{X}_n, \bar{Y}_n\}$ should be reordered to satisfy the simulation demands of the stochastic process.

A certain simulation error exists owing to the number of truncated terms, which is similar to the discrete expression of a stochastic field. The variance error of the non-stationary ground motion stochastic simulation is defined as Liu et al. (2015b):

$$\varepsilon(N) = 1 - \frac{\int_0^{\omega_u} \int_0^T S_{\ddot{x}_g}(t, \omega) dt d\omega}{\int_0^\infty \int_0^T S_{\ddot{x}_g}(t, \omega) dt d\omega} \tag{3.17}$$

where $\omega_u = N\Delta\omega$ is the calculation cutoff frequency and N is the quantity of cutoff terms.

(2) Non-stationary ground motion generation results

Table 3.1 lists the parameter values of the generalized evolution spectrum model for non-stationary ground motions recommended in this book according to current Chinese standards (DL5073–2000). The model parameter \bar{a}_{max} is generally considered to be the typical value of the horizontal design basic seismic acceleration.

This book considers the corresponding design basic seismic acceleration value under a seismic fortification intensity of VII degrees, namely $\bar{a}_{max} = 0.1$ g. A category-IV site is selected as the research object. The stochastic ground motion model and spatial stochastic field model of the geotechnical parameters are introduced to comprehensively consider the stochasticity and uncertainties of the ground motion and spatial distribution characteristics of the soil.

Table 3.1 Parameter values of the generalized evolution spectrum model of non-stationary ground motion

Parameter	Site type			
	I	II	III	IV
$\omega_0(s^{-1})$	31.42	20.94	15.71	9.67
ξ_0	0.64	0.72	0.80	0.90
$a(s)$	4	5.5	7	8.5
b	1.8	1.8	1.8	1.8
$c(s^{-1})$	8	4	2	1
d	0.1	0.1	0.1	0.1
\bar{r}	3.50	3.37	3.3	3.02
$T(s)$	15	20	25	30

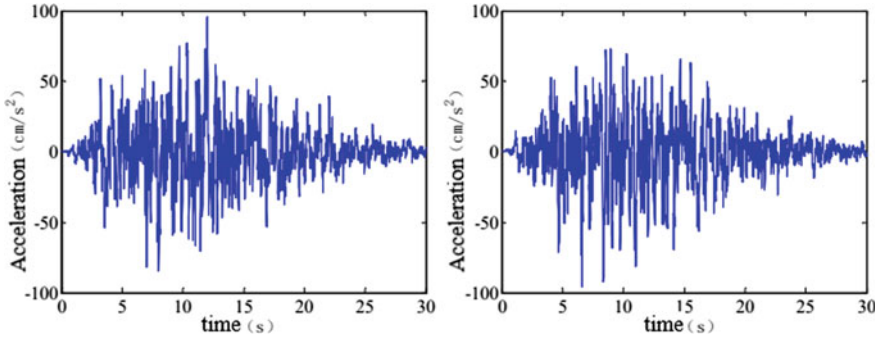
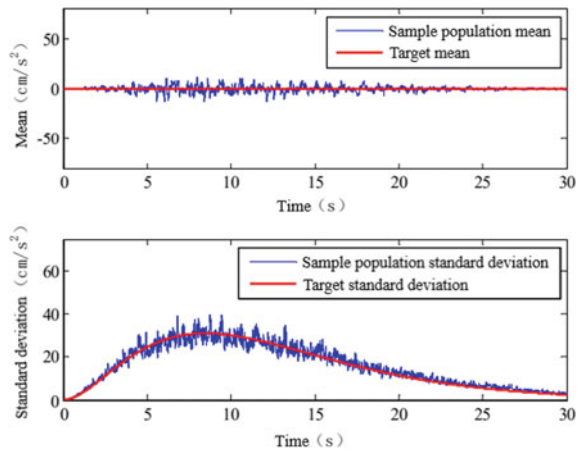


Fig. 3.5 Representative samples of non-stationary stochastic ground motions

According to the simulation method of non-stationary ground motions, the number theory method is first used to select sample points to discretize the three basic random variables into representative point sets into standard Gaussian probability space and calculate their probabilities. A total of 226 samples points is obtained. This corresponds to the basic random variable Θ , which describes the stochasticity of ground motion, and transforms it into a uniform distribution on $[-\pi, \pi]$ using an equal probability transformation. The discrete representative samples points are then substituted into Eq. (3.16) to produce a series of standard orthogonal stochastic variables, and the non-stationary seismic motion simulation spectrum expression Eq. (3.14) is used to generate a sequence of representative seismic acceleration time histories (Fig. 3.5). The quantity of truncation terms is 2000, the frequency difference $\Delta\omega = 0.15$ rad/s, and the truncation frequency $\omega_u = 300$ rad/s. Substituting the error calculation into Eq. (3.17) yields a variance error of 2.24%.

Figure 3.6 shows a comparative analysis of the overall mean, standard deviation, and target value of the 226 representative seismic acceleration time histories. The

Fig. 3.6 Comparison of the mean and standard deviation between the population and target of the non-stationary stochastic ground motion samples



degree of agreement between the sample population and target is basically the same. The target mean value is zero because the ground motion is usually assumed to be a non-Gaussian stochastic process with a mean value of zero. The target standard deviation is calculated by the Fourier transform of the power spectrum based on the autocorrelation function.

3.3 Slope Stochastic Seismic Response Analysis

This chapter first considers a single random factor and the geotechnical parameter uncertainty. MATLAB is used to complete the stochastic field discretization by sequentially modifying the calculation source file (“`.xml`”) to combine the soil parameter stochastic field and finite element calculation model, and 127 new “`.xml`” calculation files are generated. Using the same method, 226 new “`.xml`” calculation files are generated that account for the uncertainty of the soil physical properties and stochasticity of earthquake excitations based on the number theory selection results.

A series of deterministic analysis calculation results are then obtained by batch processing, which are substituted into the GDEE, and the finite difference method is applied for its solution. The PDF of the slope nonlinear dynamic response considering the influence of the soil parameter uncertainty and spatial variability is obtained, which contains all the probability information of the slope stochastic system.

When solving the GDEE, Li and Chen (2003) compared the differences among the unilateral and bilateral difference schemes in terms of convergence, compatibility, and stability. They demonstrated that the bilateral difference scheme has a preferable computational result, but that it is necessary to further combine the unilateral difference scheme to handle extreme event analysis problems. To assure the reliability of the results, this chapter compares the Lax-Wendroff (LW) format and the modified total variation diminishing (TVD) format in the bilateral difference format. The results indicate that the LW format has a faster computational astingency and higher accuracy, but does not ensure the non-negativity of the PDF. The TVD avoids the shortcomings using a flux limiter.

Figures 3.7, 3.8, 3.9, 3.10, 3.11 and 3.12 show the seismic response results of the slope safety factor under single and double random factors. Among them, Figs. 3.7 and Fig. 3.8 show the response under the uncertainty of geotechnical parameters, and Figs. 3.9, 3.10, 3.11 and 3.12 show the results under the combined action of the geotechnical parameter uncertainties and ground motion stochasticity.

Figure 3.9 is the mean and standard deviation time history curve of the slope safety factor calculated using LW and TVD under dual random factors. There is no substantial difference between the two calculation formats, and the relative error is calculated to be 2.7%. This value is less than the allowable error requirement of 5%, which ensures the accuracy of the finite difference solution.

Figures 3.7 and 3.10 are the PDFs of the slope safety factor under single and double random factors, respectively, at three times selected during the entire earthquake event. The distribution range of the safety factor and peak PDF value are shown

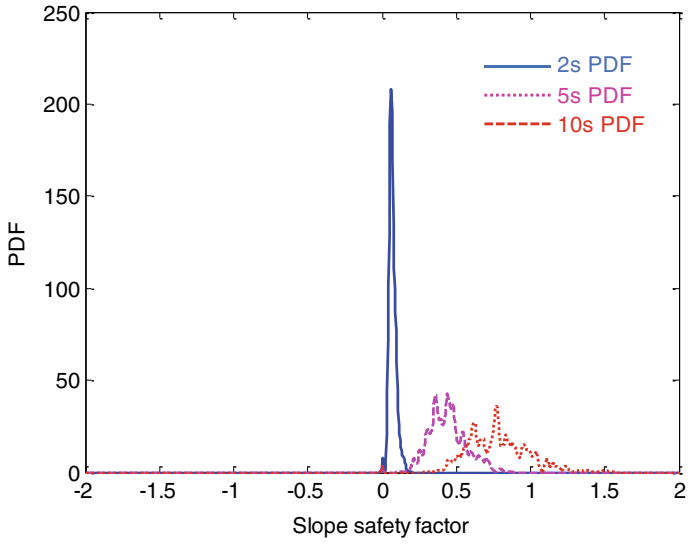


Fig. 3.7 PDFs of the slope safety factor under a single random factor

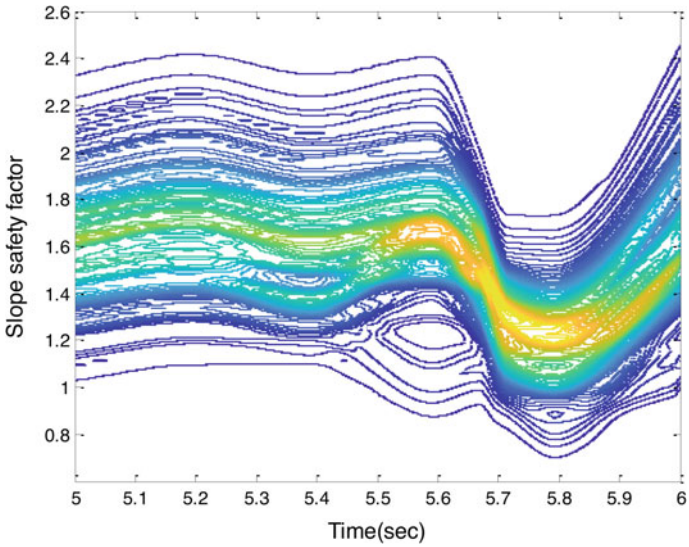


Fig. 3.8 Equal probability density contour of the slope safety factor under a single random factor (5–6 s)

Fig. 3.9 Mean and standard deviation of the slope safety factor under dual random factors

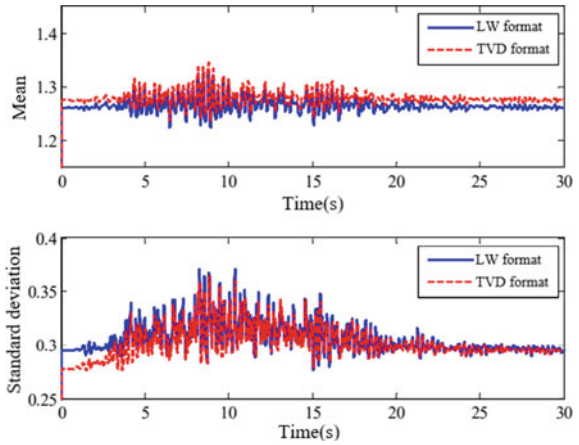


Fig. 3.10 PDFs of the slope safety factor at different times under dual random factors

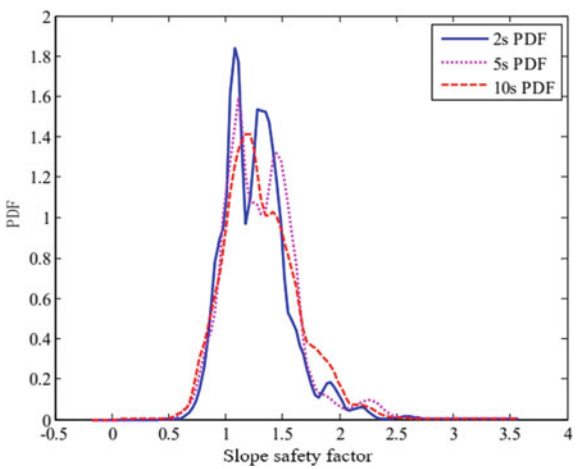


Fig. 3.11 Slope safety factor probability density evolution surface under dual random factors (5–6 s)

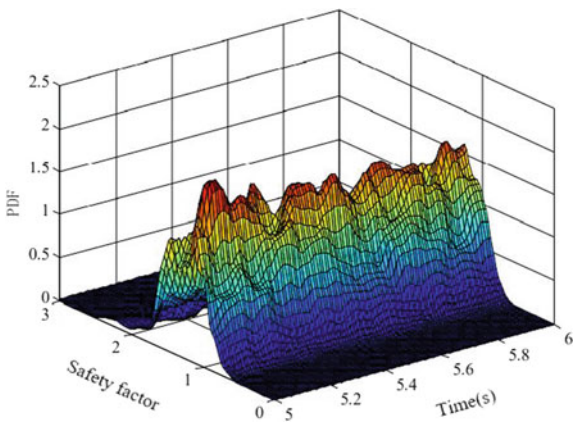
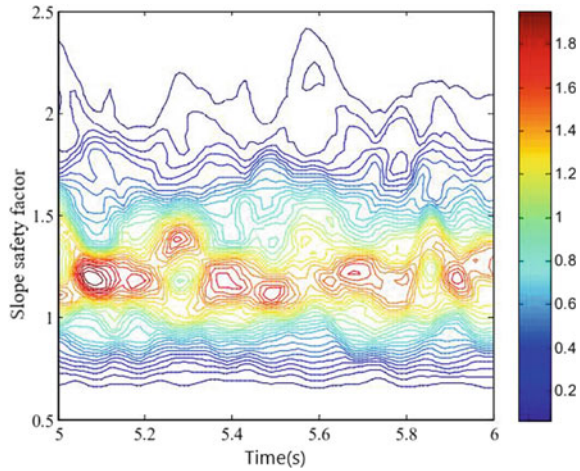


Fig. 3.12 Slope safety factor probability density contour under double random factors (5–6 s)



to change over time. This represents the dynamic influence of random factors on the safety factor. The PDF values are also usually no longer lognormally distributed and there is multimodality. This demonstrates the potential inaccuracy of conventional slope reliability analysis methods based on pre-assumed response probability distribution types (e.g., lognormal distribution).

Figure 3.11 shows the slope safety factor probability density evolution surface at 5–6 s intercepted under dual random factors. The PDF clearly presents a complicated evolution process with time. The surface evolves over time like the peaks of a mountain range. The top of the mountains corresponds to larger PDF values (red regions), and the foot of the mountains corresponds to smaller PDF values (blue regions). The PDF profile shapes greatly differ at different times, and there is also a multi-peak phenomenon at the top of the mountains where the PDF value is larger.

Figures 3.8 and 3.12 show the equal probability density contours under single and double random factors, respectively, which were acquired by projecting the probability density evolution surface on the horizontal plane. The densely-curved areas indicate higher PDF gradients at those locations. The probability density evolves over time in the graph, similar to a water flow. This “flow” process is quite complicated and contains a large number of vortices, which is thus non-stationary flow. When the fixed safety factor is 1, the probability density exerts notable fluctuation characteristics with time, which indicates the possibility of failure changes with time under earthquake action. The equal probability density line under the combined action of the double random factors of the ground motion and soil parameters in Fig. 3.12 is denser and more disorderly than that in Fig. 3.8, with the appearance of a large

number of vortices over an expanded distribution range. The trend of the equal probability density contour in Fig. 3.12 is also relatively stable and does not contain the visible fluctuations observed in Fig. 3.8, which reflects the impact of the ground motion amplitude characteristics.

3.4 Slope Nonlinear Stochastic Seismic Dynamic Reliability Analysis

3.4.1 Principles of Slope Reliability Analysis

Many of the factors that influence slope seismic dynamic stability (e.g., soil physical and mechanical parameters, external loads) can be generally regarded as random variables, which can be summarized as two comprehensive quantities of load Q and resistance R . The powerful function Z of the slope is then expressed as:

$$Z = g(R, Q) = g(X) = F_s(X) - 1 \quad (3.18)$$

where $X = (X_1, X_2, \dots, X_n)^T$ is a random vector and F_s is the slope safety factor. Powerful function calculations can be performed to evaluate the slope safety state. A slope is generally in a safe state when the powerful function is >0 . When the performance function is 0, the system is in the critical state and the powerful function is referred to as the ultimate state equation. When the powerful function is <0 , the slope is in a failure state and its corresponding probability is referred to as the failure probability P_f , which is given as:

$$P_f = P(Z < 0) = \int_{Z < 0} f(X) dx \quad (3.19)$$

where $f(X)$ is the joint PDF of the performance function g . The reliability index β is also introduced to characterize the slope stability margin, which is defined as:

$$\beta = \frac{\mu_Z}{\sigma_Z} \quad (3.20)$$

where μ_g is the expectation and σ_g is the standard deviation of the powerful function g .

Slope dynamic reliability analysis is the product of a combination of deterministic seismic dynamic stability evaluation and dynamic reliability assessment. Its essence is to transform uncertain problems into certain definite problems for solution. Deterministic methods (e.g., limit equilibrium method, FEM) can be applied to establish

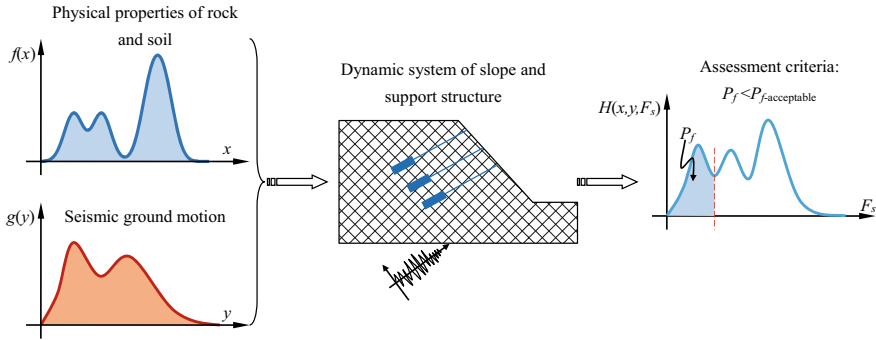


Fig. 3.13 Solution modes of slope reliability analysis

the analysis model of slope stability and acquire the safety factor F_s in Eq. (3.18). The external nesting then has a universal reliability calculation method to compute P_f and β in Eqs. (3.19) and (3.20). The solution mode is shown in Fig. 3.13.

To obtain the nonlinear dynamic reliability of a slope, the PDF and CDF of the safety factor under dynamic action are calculated using the extreme virtual distribution based on the PDEM (Chen & Li, 2007). This analysis is similar to probability density evolution theory under static conditions, and also treats the time-invariant response as the cut-off random variable of the virtual stochastic process by creating a virtual procedure. However, the time-invariant response is usually selected as the extreme or equivalent extreme value of the time history curve. The lowest safety factor value is usually selected as the judgment value of the slope stability (Huang & Xiong, 2017).

3.4.2 Results of Slope Stochastic Seismic Dynamic Reliability Analysis

Using the above method, the PDF and CDF are achieved based on extreme events under the combined action of double random factors, as shown in Figs. 3.14 and 3.15. The PDF of the slope seismic dynamic safety factor no longer exhibits a typical parameter probability distribution (e.g., censored normal distribution, logarithmic distribution) owing to the combined effects of the ground motion stochasticity, soil parameter uncertainties, and nonlinearity dynamic behavior of the slope. There is instead a notable multi-peak phenomenon, which strongly illustrates the shortcomings of reliability analysis using the parameter fitting method that presupposes the stochastic response distribution type. Assuming that the safety factor is 1, the slope is in a state of limit equilibrium. According to the CDF, the slope failure probability is 0.5150 when considering the stochastic excitation and uncertainty of the soil parameters.

Fig. 3.14 PDF of the slope safety factor based on extreme events in the limit state

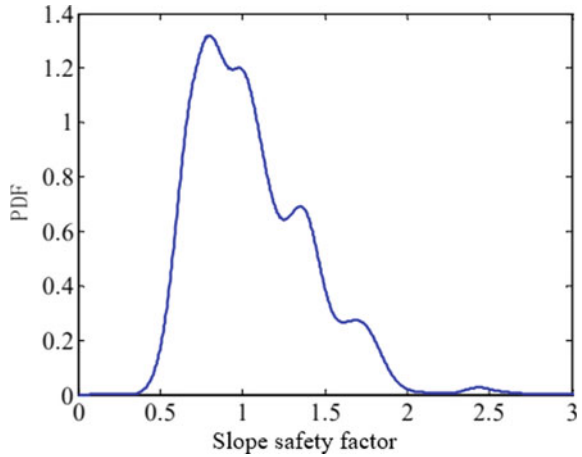
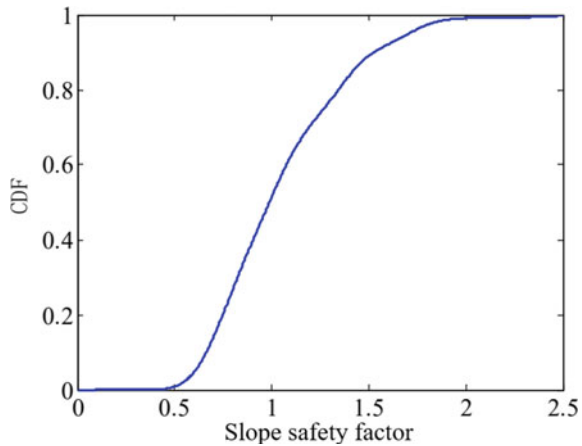


Fig. 3.15 CDF of the slope safety factor based on extreme events in the limit state



3.5 Verification of Slope Reliability Analysis Method Based on PDEM

3.5.1 Monte Carlo Simulations

The MCS method is a commonly used approach in reliability analysis. This method can consider the nonlinearity and discreteness of limit state surfaces and has a certain versatility. However, the large number of calculations required to accurately estimate the failure probability is a bottleneck that restricts the practical application of this method, especially when the powerful function has no analytical formula and the failure probability is relatively small. The MCS method is therefore a calculation method in slope stochastic nonlinear dynamic reliability analysis with relatively high

accuracy. In practical applications, the MCS method is used to verify the approximate analytical results of other numerical solutions (e.g., PDEM). This section uses the MCS method to verify the reliability analysis methods introduced above at static and dynamic levels.

(1) **Static level verification**

The slope model shown in Fig. 3.2 is used considering the large amount of MCS calculations, and the random variable model is used to describe the uncertainty of the soil parameters, ignoring the relevance between c and φ . The probability distribution is assumed to be a lognormal distribution. The static stability analysis adopts the SLOPE\W module and simplified Bishop method, and the sliding surface search adopts the cut-in and cut-out method. On the basis of the average parameter values, the safety factor is 1.207 under static conditions.

Differing from dynamic conditions, the safety factor of a slope under static conditions is no longer a time history curve, but degenerates to a point. It is therefore necessary to artificially introduce a virtual time parameter for each safety factor calculation result to make the slope safety factor a cut-off random variable for the virtual random process, and then import it into the generalized probability density evolution equation.

This article uses the MCS method based on Latin hypercube sampling. Using the “lhsnorm” function in MATLAB, 10,000 samples were randomly generated, the safety factors of each sample were calculated, and statistical analysis was performed. The analysis results are compared with the analysis results based on the PDEM.

Figure 3.16 is a PDF of the safety factor under static conditions obtained by the MCS and PDEM calculation methods. The processing of the MC calculation data adopts the kernel function method. Figure 3.16 shows that the PDF curves obtained using the two calculation methods have good consistency. Figure 3.17 is the CDF achieved by the MCS and PDEM calculation methods, and the agreement between

Fig. 3.16 PDF of the safety factor calculated based on the PDEM and MCS methods under static conditions

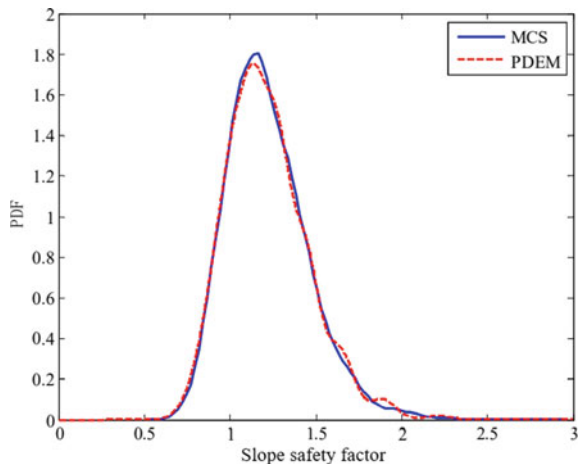


Fig. 3.17 CDF of the safety factor calculated based on the PDEM and MCS methods under static conditions

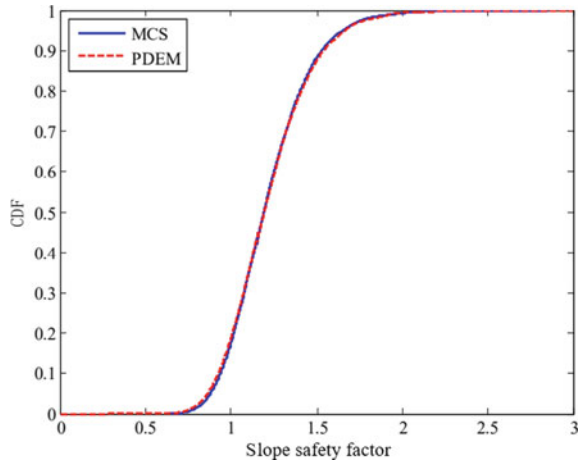


Table 3.2 Comparison of the first two-order statistics and failure probability of the PDEM and MCS methods

	PDEM	MCS	Relative error (%)
Number of calculations	127	10,000	–
Mean	1.2190	1.2187	0.025
Variance	0.2492	0.2407	3.5
Probability of failure	0.1861	0.1729	7.6

the two is almost the same. Assuming that the safety factor is less than 1 to define a slope in a failure state, the slope static failure probability calculated by the PDEM and MCS methods is 0.1861 and 0.1729, respectively.

Table 3.2 further compares the first two statistics calculated by the two methods, and the relative errors are relatively close. Notably, when calculating the relative error, the MCS result is assumed as the exact solution. However, the calculation result of the stochastic simulation is not necessarily the exact solution (Chen & Li, 2006b). From the standpoint of calculation time, the slope reliability analysis using the PDEM has a calculation efficiency that is nearly a hundred times higher than that of the MCS method.

(2) Seismic dynamic level verification

On the basis of static verification, dynamic reliability analysis is further performed under seismic conditions. The analysis process in Fig. 3.2 is applied. The corrected strong motion record El Centro wave is applied. The initial stress field distribution is first calculated, the QUAKE/W module is then used to computed the stress and strain distribution, and the finite element slip surface stress method in the SLOPE/W module is used to acquire the slope safety factor time history curve.

In this section, the hyperbolic dynamic constitutive model is used to calculate the nonlinear dynamic time history analysis method. In addition to the known parameters in Sect. 3.2.1, pivotal parameters such as the damping ratio and small strain shear modulus G_{max} are required. The damping ratio used in this book is 0.05, and the maximum value is 0.3. G_{max} is estimated according to the empirical formula given in this module. The maximum depth of the slope is 15 m, the soil is normally consolidated, the void ratio is set to 1, the plasticity index is set to 18, and the static lateral pressure coefficient is set to 0.5. The function relationship between G_{max} and effective stress is obtained, as demonstrated in Fig. 3.18.

When calculating the initial stress field of the slope, the constraint condition is that the two ends of the slope are fixed in the X direction and the base of the slope is fixed in the X/Y direction. After entering the dynamic analysis, the bottom restraint conditions remain unchanged, and the two ends of the restraint conditions become a fixed Y direction. Mean values of c and φ are used to compute the time history curve of the slope safety factor under the action of seismic excitation, as shown in Fig. 3.19. The slope safety factor decreased to the minimum value of 1.0086 at 2.46 s under the ground motion action, and the maximum value (1.6095) appeared at 4.52 s.

The sample selection for the MCS method based on Latin hypercube sampling included a sample size of 10,000, which was verified from the sample average value and standard deviation. Figure 3.20 illustrates the standard deviation of the slope safety factor computed by the PDEM and MCS methods. Figure 3.20 shows that, aside from some visible errors at a few points, the degree of agreement between the two is quite consistent.

We then consider a sample set composed of different slope safety factor time history curves at the same time, in which the cut-off random variable and its statistical analysis can be used to obtain the PDF at that time. This book chooses the slope safety factor cut random variables at 5 s and 8 s, and compares the PDFs calculated by the PDEM and MCS methods, as shown in Figs. 3.21 and 3.22, respectively. The PDFs

Fig. 3.18 Relation diagram between clay G_{max} and effective stress

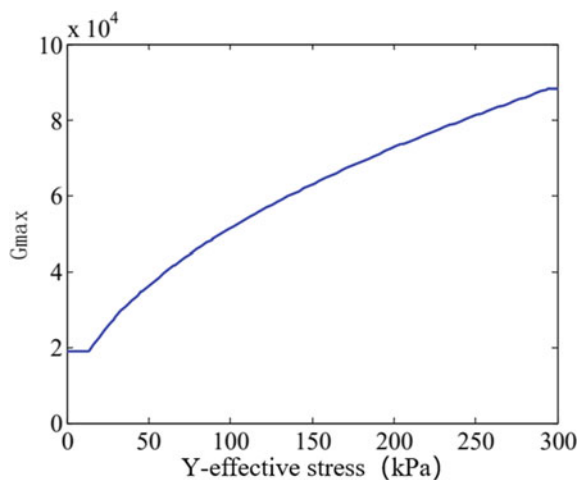


Fig. 3.19 Time history curve of the slope safety factor

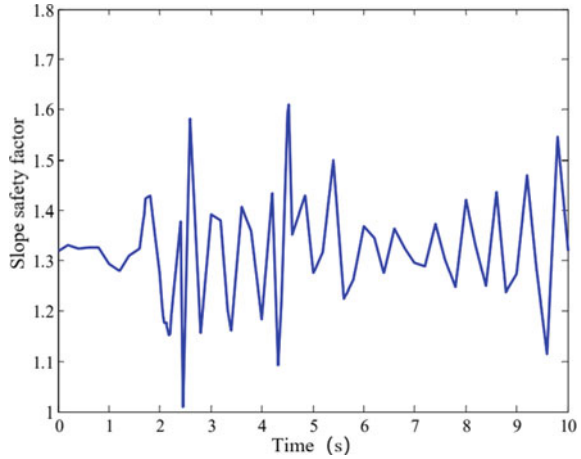
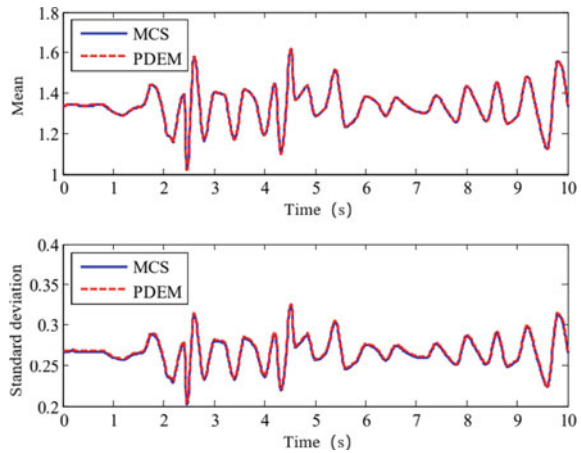


Fig. 3.20 Mean and standard deviation values of the safety factors calculated based on the PDEM and MCS methods under dynamic conditions



achieved using the two methods are nearly the same; however, the calculation amount of the MCS method is nearly one hundred times higher than that of the PDEM.

Figures 3.23 and 3.24 show the PDF and CDF results of the extreme value distribution of the slope safety factors under earthquake excitations, and compares the results of the PDEM and MCS calculations. Similarly, when the slope safety factor is equal to 1, the slope is in a critical state. On the basis of Fig. 3.24, the slope seismic dynamic failure probability calculated based on the PDEM is 0.5132, and the dynamic failure probability calculated by the MCS method is 0.5148. The relative error is only 0.31%, which is greatly reduced compared with the relative error under static conditions. This is because of the analysis error caused by introducing the virtual time parameters when solving the static force, which reflects the shortcomings of the MCS method in terms of stochastic convergence. A comparison of

Fig. 3.21 PDF of slope safety factor calculated by the PDEM and MCS methods at $t = 5$ s

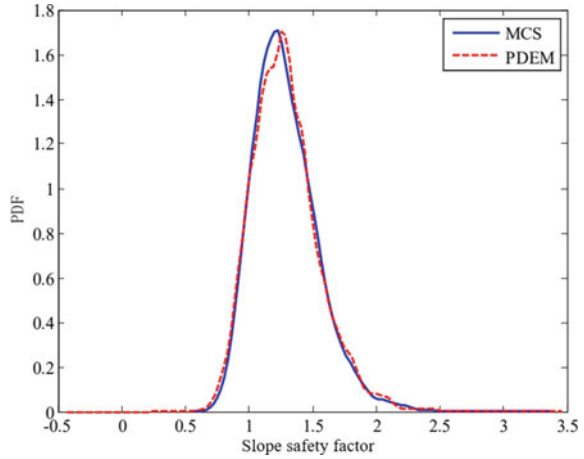
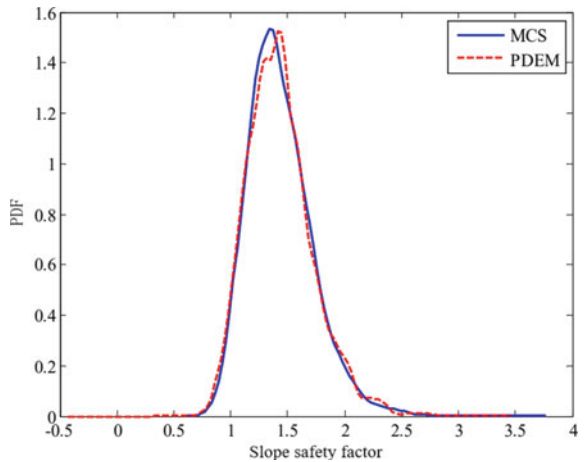


Fig. 3.22 PDF of the slope safety factor calculated by the PDEM and MCS methods at $t = 8$ s



the slope failure probability under static and dynamic action clearly shows that the failure probability increases by nearly a factor of three for the nonlinear seismic dynamic stability of slopes that suffer from seismic excitations.

3.5.2 Verification Using a Closed Form Analytical Solution

The previous section verifies the effectiveness of the PDEM compared with the Monte Carlo stochastic simulation results. This section takes a single-degree-of-freedom system as an example to verify the effectiveness of the PDEM method from the perspective of analytical solutions. A single-degree-of-freedom system is

Fig. 3.23 Comparison of the slope safety factor PDF under extreme conditions

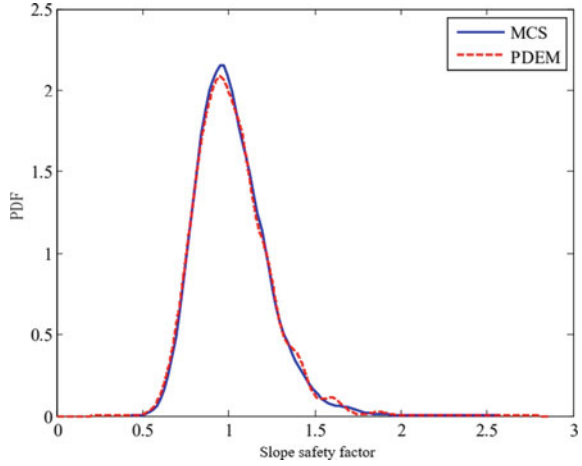
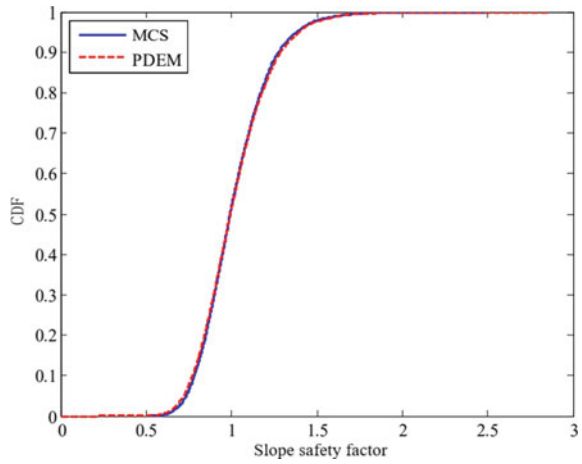


Fig. 3.24 Comparison of the slope safety factor CDF under extreme conditions



subjected to the stochastic vibration effect, the PDF of the response is computed, and the solution is compared and verified with the PDEM.

Here, the single-degree-of-freedom system exposed to stochastic excitation is expressed as:

$$\ddot{X} + X = (1 - \omega^2)\cos(\omega t) \tag{3.21}$$

where ω is a uniform random variable on $[5\pi/4, 7\pi/4]$, and the initial conditions of the dynamic equation are $X(t)|_{t=0} = x_0, \dot{X}(t)|_{t=0} = \dot{x}_0$.

To facilitate the calculation of the dynamic differential equation shown in Eq. (3.21), it is assumed that $X(t)|_{t=0} = x_0 = 1.0\text{m}$ and $\dot{X}(t)|_{t=0} = \dot{x}_0 = 0$. The analytical result of Eq. (3.21) can be acquired as:

$$X(t) = (x_0 - 1)\cos t + \cos(\omega t) = \cos(\omega t) \quad (3.22)$$

where $X(t)$ is a stochastic process because ω is a stochastic variable.

The PDF of ξ is denoted as f_ξ , assuming $\xi = \omega t$. According to the conservation of probability, ω can be obtained as:

$$f_\xi(x, t) = \frac{1}{t} f_\omega\left(\frac{x}{t}\right) \quad (3.23)$$

$X(t)$ can be re-expressed as $X(t) = \cos(\xi)$ if $X(t)$ is further denoted as $Z = \cos(\xi)$. Its PDF $f_z(x, t)$ can then be represented as:

$$f_z(x, t) = \frac{1}{\sqrt{1-x^2}} [f_\xi(\arccos x, t) + f_\xi(2\pi - \arccos x, t)] \quad (3.24)$$

Equation (3.24) can be therefore repeated as $X(t) = Z$, similarly, the PDF of $X(t)$ can be expressed as:

$$\begin{aligned} f_X(x, t) &= f_Z(x, t) \\ &= \begin{cases} \frac{1}{\sqrt{1-x^2}} [f_\xi(\arccos x, t) + f_\xi(2\pi - \arccos x, t)], & |x| \leq 1 \\ 0, & \text{otherwise} \end{cases} \end{aligned} \quad (3.25)$$

Because ω is uniformly distributed on $[5\pi/4, 7\pi/4]$, its PDF is:

$$f_\omega(x, t) = \begin{cases} \frac{1}{\frac{7\pi}{4} - \frac{5\pi}{4}} = \frac{2}{\pi}, & \frac{5\pi}{4} \leq \omega \leq \frac{7\pi}{4} \\ 0, & \text{otherwise} \end{cases} \quad (3.26)$$

Therefore, according to a series of mathematical derivations, the PDF of $X(t)$ at $t = 1$ s can be obtained as:

$$f_X(x, t)|_{t=1} = \begin{cases} \frac{1}{\pi\sqrt{1-x^2}}, & -\frac{\sqrt{2}}{2} \leq x \leq \frac{\sqrt{2}}{2} \\ 0, & \text{otherwise} \end{cases} \quad (3.27)$$

When $t = 1$ s, the second-order statistics (e.g., average and standard deviation) can be obtained based on the PDF $f_X(x, t)|_{t=1}$ of the displacement response $X(t)$ of the single-degree-of-freedom system, according to:

$$\begin{aligned} \mu(t) &= E[X(t)] = \int_{\eta_1}^{\eta_2} \cos(xt) f_{\omega}(\omega) dx \\ &= \frac{1}{\eta_2 - \eta_1} [\sin(\eta_2 t) - \sin(\eta_1 t)] \end{aligned} \tag{3.28}$$

$$\begin{aligned} S_X(t) &= \int_{\eta_1}^{\eta_2} [\cos(xt)]^2 f_{\omega}(\omega) dx \\ &= \frac{1}{(\eta_2 - \eta_1)t} \left[\frac{(\eta_2 - \eta_1)t}{2} + \frac{\sin(2\eta_2 t) - \sin(2\eta_1 t)}{4} \right] \end{aligned} \tag{3.29}$$

Among them, $\eta_1 = 5\pi/4$, $\eta_2 = 5\pi/4$. The standard deviation $X(t)$ can therefore be obtained as:

$$\sigma_X(t) = \sqrt{S_X(t) - \mu_X^2(t)} \tag{3.30}$$

Figure 3.25 compares the PDF results of the displacement response obtained by the PDEM and analytical solutions in the single-degree-of-freedom system. By comparison of the PDF levels, it is theoretically explained that the probability density evolution theory has a higher calculation accuracy and effectiveness. The evolutionary level of the PDF of the stochastic dynamic system lays the foundation for the solution of the system dynamic reliability.

Figure 3.26 shows the second-order statistical solution (mean and standard devi-

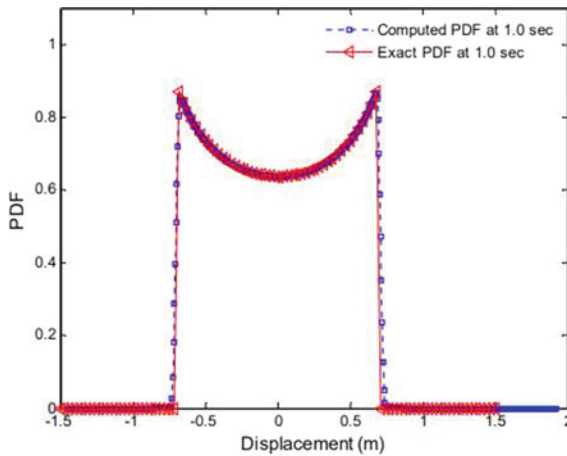
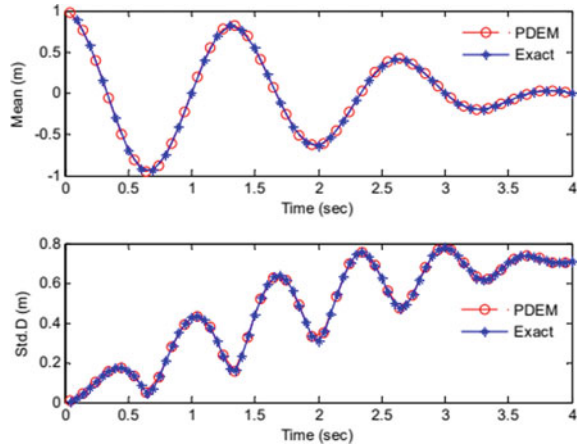


Fig. 3.25 PDF of the displacement response in a single-degree-of-freedom system ($t = 1$ s) (reprinted from Huang et al. 2015 with permission of Elsevier)

Fig. 3.26 Second-order statistics information (mean and standard deviation) of a single-degree-of-freedom system (reprinted from Huang et al. 2015 with permission of Elsevier)



ation) of the single-degree-of-freedom stochastic dynamic system. The analytical solution further demonstrates the correctness and validity of the PDEM.

References

- Chen, J., & Li, J. (2007). The extreme value distribution and dynamic reliability analysis of nonlinear structures with uncertain parameters. *Structural Safety*, 29(2), 77–93.
- Chen, J., & Li, J. (2006a). Strategy of selecting points via number theoretical method in probability density evolution analysis of stochastic response of structures. *Acta Mechanica Sinica*, 38(1), 134–140.
- Chen, J., & Li, L. (2006b). Strategy of selecting points via sphere of contact in probability density evolution method for response analysis of stochastic structures. *Journal of Vibration Engineering*, 19(1), 1–8.
- Chen, X., Gao, R., & Gong, W., et al. (2018). Random seismic response and dynamic fuzzy reliability analysis of bedding rock slopes based on pseudoexcitation method. *International Journal of Geomechanics*, 18(3).
- Cho, S. E. (2007). Effects of spatial variability of soil properties on slope stability. *Engineering Geology*, 92(3–4), 97–109.
- Cho, S. E. (2009). Probabilistic stability analyses of slopes using the ANN-based response surface. *Computers and Geotechnics*, 36(5), 787–797.
- Cho, S. E. (2010). Probabilistic assessment of slope stability that considers the spatial variability of soil properties. *Journal of Geotechnical and Geoenvironmental Engineering*, 136(7), 975–984.
- Del Gaudio, V., & Wasowski, J. (2004). Time probabilistic evaluation of seismically induced landslide hazard in Irpinia (Southern Italy). *Soil Dynamics and Earthquake Engineering*, 24(12), 915–928.
- El-Ramly, H., Morgenstern, N. R., & Cruden, D. M. (2002). Probabilistic slope stability analysis for practice. *Canadian Geotechnical Journal*, 39(3), 665–683.
- Griffiths, D. V., Huang, J., & Fenton, G. A. (2009). Influence of spatial variability on slope reliability using 2-d random fields. *Journal of Geotechnical and Geoenvironmental Engineering*, 135(10), 1367–1378.

- Huang, Y., & Xiong, M. (2017). Dynamic reliability analysis of slopes based on the probability density evolution method. *Soil Dynamics and Earthquake Engineering*, 94, 1–6.
- Huang, Y., Xiong, M., & Zhou, H. (2015). Ground seismic response analysis based on the probability density evolution method. *Engineering Geology*, 198, 30–39.
- Huang, Y., Zhao, L., & Li, X. (2020). Slope-dynamic reliability analysis considering spatial variability of soil parameters. *International Journal of Geomechanics*, 20(6).
- Jha, S. K. (2015). Effect of spatial variability of soil properties on slope reliability using random finite element and first order second moment methods. *Indian Geotechnical Journal*, 45(2), 145–155.
- Johari, A., & Khodaparast, A. R. (2015). Analytical stochastic analysis of seismic stability of infinite slope. *Soil Dynamics and Earthquake Engineering*, 79, 17–21.
- Li, J., & Chen, J. (2003). Probability density evolution method for analysis of stochastic structural dynamic response. *Acta Mechanica Sinica*, 35(4), 437–442.
- Li, K. S., & Lumb, P. (1987). Probabilistic design of slopes. *Canadian Geotechnical Journal*, 24(4), 520–535.
- Lin, M., & Wang, K. (2006). Seismic slope behavior in a large-scale shaking table model test. *Engineering Geology*, 86(2–3), 118–133.
- Liu, L., & Cheng, Y. (2018). System reliability analysis of soil slopes using an advanced kriging metamodel and Quasi-Monte Carlo simulation. *International Journal of Geomechanics*, 18(8).
- Liu, Z., Wang, L., Dan, Q., et al. (2015). Generalized evolutionary spectrum of non-stationary ground motion and its applications in seismic design of hydraulic structures. *Journal of Hydraulic Engineering*, 46(9), 1028–1036.
- Liu, Z., Zeng, B., & Wu, L. (2015). Simulation of non-stationary ground motion by spectral representation and random functions. *Journal of Vibration Engineering*, 28(3), 411–417.
- Mahdiyari, A., Hasanipanah, M., Armaghani, D. J., et al. (2017). A Monte Carlo technique in safety assessment of slope under seismic condition. *Engineering with Computers*, 33(4), 807–817.
- Tang, B., & Liu, P. (2011). Expression of stochastic structures with monophyletic random vector. *Journal of Yangzhou University*, 14(4), 64–68.
- Wang, W., Yuan, W., Li, X. C., et al. (2016). Evaluation approach of the slope stability based on deformation analysis. *International Journal of Geomechanics*, 16(2), 6.
- Wu, Z., Chen, J., Li, Y., et al. (2015). An algorithm in generalized coordinate system and its application to reliability analysis of seismic slope stability of high rockfill dams. *Engineering Geology*, 188, 88–96.
- Xu, X., & Huang, Y. (2021). Parametric study of structural parameters affecting seismic stability in slopes reinforced by pile-anchor structures. *Soil Dynamics and Earthquake Engineering*, 147, 106789.
- Zou, J. Z., Williams, D. J., & Xiong, W. L. (1995). Search for critical slip surfaces based on finite-element method. *Canadian Geotechnical Journal*, 32(2), 233–246.

Chapter 4

Dynamic Failure Mechanism and Post-failure Behavior Analysis of Slopes



The previous chapters mainly focus on the failure potential under different seismic intensity conditions, which is essential for landslide prevention. In terms of mitigation, not only should the landslide surface and slope volume be determined, but also the run-out distance and flow depth should be considered. The entire dynamic evolution process of slope failure triggered by earthquake activity usually includes different stages: small deformation accumulation; instability; large deformation flow; and deposition. Studying the stages of slope instability separately cannot clearly explain the evolution mechanism of the entire earthquake-triggered slope failure process. A unified model to analyze the entire landslide process is therefore of great significance for the design of retaining structures.

4.1 Evolution Process of Slope Failure

A slope can be divided into two parts: a skeleton formed by rock and soil particles; and the fluid between the gaps. Weak interactions between rock and soil particles often lead to various mechanical characteristics at different stages, such as solid-like mechanical behavior during the finite deformation stage and liquid-like mechanical behavior during the large deformation stage (Pastor et al., 2010; Prime et al., 2014b). The different geotechnical material characteristics can be distinguished by strain. When the strain of the geotechnical materials exceeds 100%, the materials change from quasi-solid to quasi-liquid (Huang et al., 2012).

The entire dynamic process of earthquake-triggered slope failure can be generally characterized by three stages according to the mechanical characteristics of the geotechnical materials: (1) activation; (2) high-speed flow-like movement; and (3) final deposition. Figure 4.1 describes the entire process of slope instability and failure evolution under seismic dynamic excitation conditions. The initiation stage mainly includes the small deformation accumulation and instability process, the slope is solid-like, and the sliding surface gradually forms and connects. Once the sliding

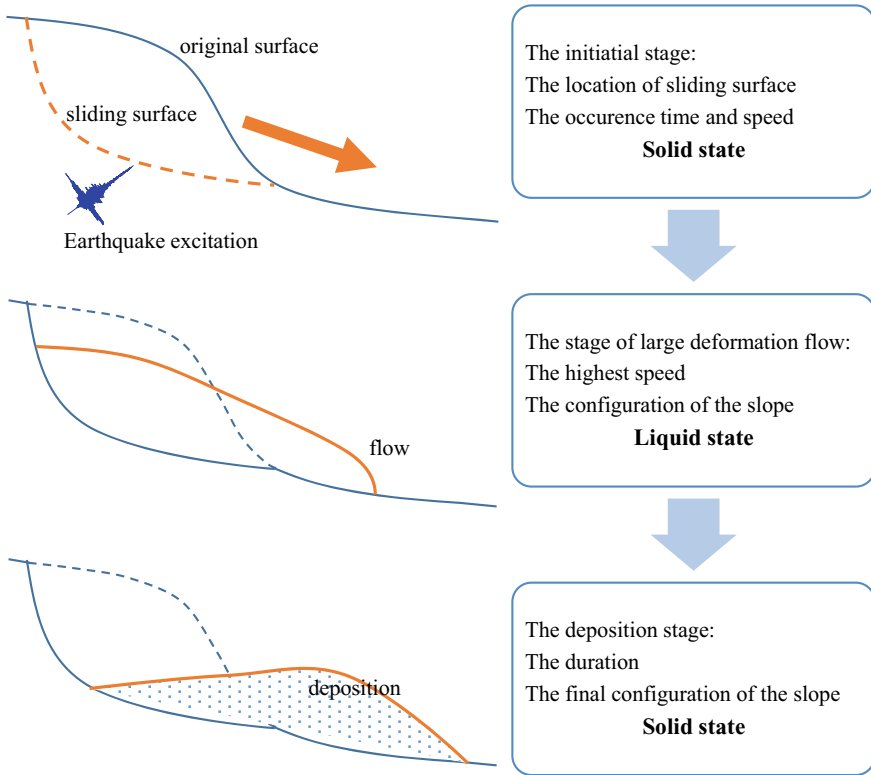


Fig. 4.1 Flow chart of entire process of slope instability and failure evolution under seismic dynamic excitation conditions

surface is formed, the slope becomes unstable and the gravitational potential energy of the slope is transferred into high kinetic energy, resulting in large deformation and fluidization of the geotechnical materials (Prime et al., 2014a). The kinetic energy of the landslide is gradually consumed owing to the influence of topography and the interaction of the moving geotechnical materials, and the deposition stage begins. The geo-materials ultimately reach a new equilibrium and act as a solid. During the entire evolution of slope dynamic instability, the geotechnical materials change from quasi-solid to quasi-liquid and ultimately return again to a quasi-solid. This kind of solid–liquid phase transformation phenomenon that occurs during the process of slope instability and failure was pointed out by Pastor et al. (2010).

4.2 Dynamic Failure Processes and Slope Failure Mechanism

The two main factors that influence the mechanism of earthquake-induced slope instability include the slope body and ground motion.

(1) Slope factors

Slope factors include three types. The first is the topographic amplification effect. It is well known that seismic amplification affects ground motion in all kinds of slopes. The ground motion of slope bodies is gradually magnified with elevation and occurs in both horizontal and vertical earthquakes. Historically, scholars mostly studied the topographic amplification effect through spectral ratios (Geli et al., 1988). Studies have shown that in addition to horizontal seismic action, the vertical seismic action of some site pairs is amplified, especially in the 20 m closest to the surface (Elgamal & He, 2004). At present, the amplification effect of ground motion in slopes can be verified by various means, including measured seismic data and shaking table tests (Fan et al., 2016).

The second slope factor is topographic site effects. Meunier et al. (2008) studied the topographic site effects and showed that landslides triggered by earthquakes mostly occur along ridge crests. This effect is generally referred to as the “backslope effect”, which means that landslides are more densely distributed in the direction facing the earthquake than in the backslope direction. Wang and Xie (2010) analyzed the data of China’s first topographic array in the Wenchuan earthquake and suggested that the slope topography had different amplification effects on the different ground motion frequencies in different directions.

The third slope factor is the progressive failure effect. The reflection effect of seismic waves mainly leads to the tensile and fracture failure of rock mass. Some scholars believe that seismic waves are reflected multiple times in complex multi-layered rock mass, which is more likely to cause rock mass fragmentation. A change of dynamic rock mass characteristics may also lead to resonance with the seismic waves in a specific frequency band, thus leading to more serious slope failure (Jiao et al., 2015).

(2) Ground motion factors

The statistical empirical formulas of seismic landslide investigations in different areas cannot be directly compared because of differing earthquake mechanisms (e.g., strike-slip fault and thrust fault).

Vertical seismic action has attracted increasing attention since the 1979 Imperial Valley earthquake (vertical peak ground acceleration (PGA) = 1.7 g, fault spacing = 3 km) and the 1994 Northridge earthquake (Elgamal & He, 2004) (vertical PGA = 0.8 g, fault spacing = 9 km). In the years following the Northridge earthquake, seismic studies on structural engineering proposed the need to consider the seismic performance of concrete structures subjected to both vertical and horizontal earthquakes (Elnashai & Papazoglou, 1997), and both vertical and horizontal acceleration

response spectra were recommended to be considered in structural seismic design. Studies have shown that 296 earthquakes and the records of 620 stations include fault vertical seismic action (Ambraseys, 1995; Ambraseys & Simpson, 1996), and the vertical acceleration of earthquakes above M6 within 10 km can easily reach more than 0.1 g (Elgamal & He, 2004). On the basis of the measured vertical ground motion data near faults, Aoi et al. (2008) also pointed out that vertical earthquakes can be simulated by a “trampoline” model.

4.2.1 Dynamic Solution Steps

In this chapter, white noise is input to test the overall response of soil slope and adjust the damping parameter of soil. The stochastic ground motion is input through batch processing to obtain all the slope dynamic response-damage conditions. Some of the solutions steps are summarized below.

- (1) Establish a slope model.
- (2) Determine the physical parameters and dynamic boundary conditions of the slope model.
- (3) Arrange monitoring points inside the slope body as measurement indicators of the acceleration, velocity, displacement, and strain, among others.
- (4) Perform a white noise test, and adjust the damping and other dynamic parameters.
- (5) Input the stochastic ground motion.
- (6) Solve the dynamic response and determine the failure behavior of the soil slope under stochastic ground motion.
- (7) Analyze the response information of all monitoring points under the action of an earthquake.
- (8) Extract all the calculation information of the monitoring points to analyze the destruction process and failure mechanism.

4.2.2 Slope Dynamic Calculation Model

This section studies the formation process of the sliding surface in a soil slope. Using the FLAC2D dynamic analysis module, the failure process and instability mechanism of soil slope under stochastic earthquakes are systematically and comprehensively studied by batch processing a large number of intensity-frequency non-stationary stochastic ground motions. The calculation model includes three parts: a geometric model; parameter setting; and monitoring setting.

- (1) Geometric model of soil slope

A homogeneous soil slope model with a height of 10 m and foot of 45° is built in this section, as shown in Fig. 4.2a. Figure 4.2b presents the FLAC2D model grid with

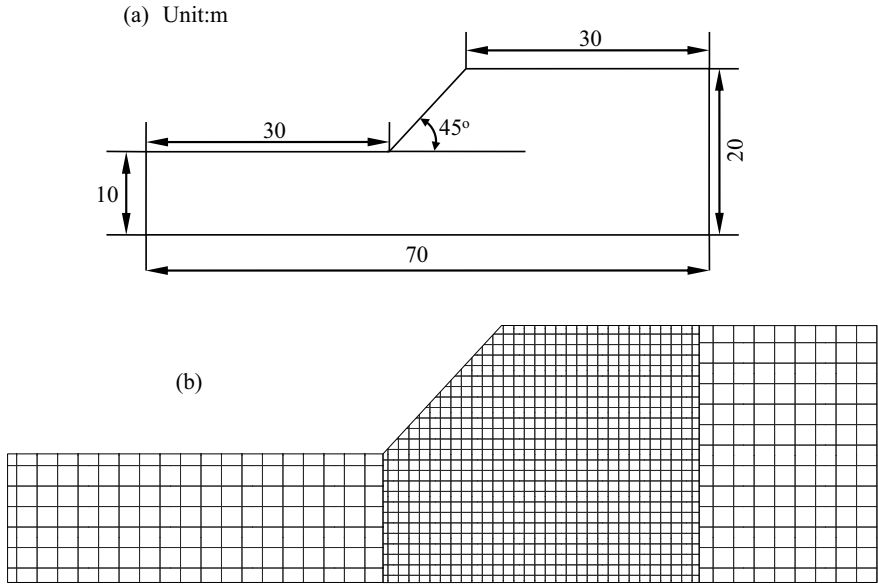


Fig. 4.2 Model of a homogeneous soil slope **a** and sketch of the finite element mesh in FLAC2D **b**

4020 calculation regions containing 52 boundary grids automatically generated by the free field boundary system on both sides of the model. The maximum grid size is 1 m, which meets the grid size requirements in Eqs. 4.1, 4.2, 4.3, 4.4 and 4.5.

$$V_s = \lambda f \tag{4.1}$$

$$G_{max} = \rho \cdot V_s^2 \tag{4.2}$$

$$K = \frac{E}{3(1 - 2\nu)} \tag{4.3}$$

$$G = \frac{E}{2(1 + \nu)} \tag{4.4}$$

$$l_{max} < \left(\frac{1}{10} \sim \frac{1}{8} \right) \lambda \tag{4.5}$$

(2) Model parameter

The Mohr–Coulomb model is chosen as the constitutive model and the other parameters are listed in Table 4.1. The Rayleigh damping parameter for dynamic calculation is damping ratio (ε_{min}) equal to 0.05 and frequency (f_{min}) of 3.5 Hz.

Table 4.1 Parameters for FLAC2D slope model

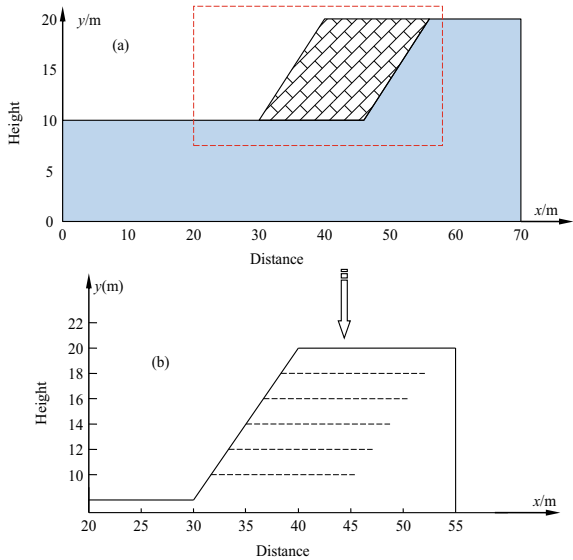
Parameter	Value
Density. (kg/m ³)	1780
bulk modulus K (MPa)	16.67
Shear modulus G (MPa)	7.692
Elastic modulus E (MPa)	20
Poisson ration μ	0.3
Cohesive force c (kPa)	20
Internal friction angle φ (°)	25
Shear strength c_t (kPa)	3
Dilatancy angle θ (°)	0

After the model is established, the safety factor can be obtained using the slice method and strength reduction method, yielding 1.53 and 1.50, respectively. The sliding surface positions obtained by the two methods are nearly the same.

(3) Monitoring design

The strain monitoring arrangement is shown in Fig. 4.3a. Thirty strain monitoring points are arranged in a row with an interval of 0.5 m, which is the same as the distance between every two layers. Because the slope height is 10 m, the whole model has 21 layers and 630 strain monitoring points in total. The layout of these monitoring points and data export are realized using a program written in FISH language. The strain monitoring points are more numerous than those for monitoring the acceleration and displacement because the grid size should be smaller than the distance between

Fig. 4.3 2D Slope profile: typical monitoring points area **a**; partial monitoring profiles for shear strain analysis **b**



adjacent monitoring points to meet the requirement that the adjacent monitoring points can monitor different element information. As shown in Fig. 4.3, the grid size of the strain monitoring area cell is 0.2–0.33 m horizontally and 0.33 m vertically, which is smaller than 0.5 m. Figure 4.3b shows five typical horizontal profiles.

4.2.3 Extraction of Dynamic Slip Surface Based on the Plastic Strain Increment

The typical failure process was analyzed using the ground motion acceleration time history sample wave 1 (selected from 508 earthquake samples), in accordance with the work of Zhao et al. (2020). The strain time history at each location can be obtained according to the strain monitoring points presented in Fig. 4.3. The specific calculation steps are described below.

- (1) The strain time histories curves of 30 monitoring points in the horizontal profile starting from the slope toe were calculated to determine whether or not there was a large plastic strain increment, which reflects that notable failure had occurred. Figure 4.4 shows the plastic strain time histories under the ground motion acceleration time history of sample wave 1, where Fig. 4.4a, c, and e represent the strain time history at various points in the horizontal section with $PGA = 0.1$ g when the slope height of is 3, 5, or 7 m, respectively, and no notable plastic deformation occurs in the slope body. Figure 4.4b, d, and f show the strain time history with $PGA = 0.4$ g when the slope height is 3, 5, or 7 m, respectively. The slope body shows notable plastic deformation, especially in the area 3.5–4.5 m from the slope.
- (2) Determine the coordinates of the maximum plastic strain of the horizontal profile. Figure 4.5a, b show the section profiles of waves 10 and 100, respectively, when $PGA = 0.4$ g. The maximum plastic strain exists at a certain location from the slope surface, which allows the position of the sliding surface coordinates to be determined and the sliding surface development time to be recorded.
- (3) Obtain the position coordinates of 21 points from 21 horizontal sections. The connection fitting is the position of the dynamic slip surface with the seismic sample, as shown in Fig. 4.6.
- (4) In this example, 508 ground motion acceleration time history samples were analyzed to determine the positions of all sliding surfaces. The probability density function (PDF) was analyzed in combination with the sliding surface development time in step 2.

Figure 4.7 shows the contours of the shear strain development under the ground motion acceleration time history of sample wave 1. At the beginning of the earthquake, the shear strain is small (approximately 10–3). The shear strain at the slope toe considerably increases with increasing PGA, and the potential sliding surface develops inside of the slope. Figure 4.7d, e portray the sudden increase of shear

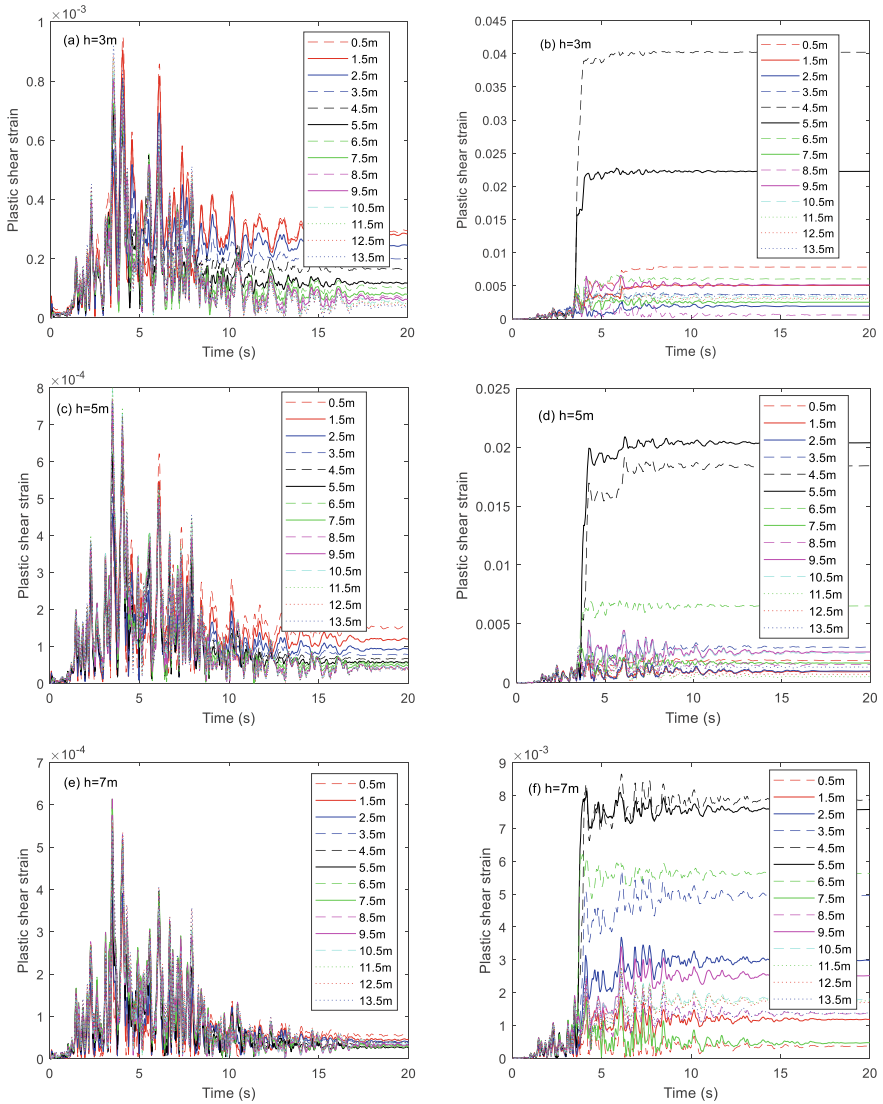


Fig. 4.4 Time history of plastic strain of the slope profile under wave 1

strain within a very short time period (4.6–4.7 s), which indicates that most seismic landslides are sudden, corresponding to Fig. 4.7b, d, f. The shear strain subsequently tends to stabilize, and a slight shear strain appears at the top of the slope. In accordance with the strain development process (Fig. 4.4) and strain contours (Fig. 4.7), the seismic failure process of the slope is roughly determined as follows.

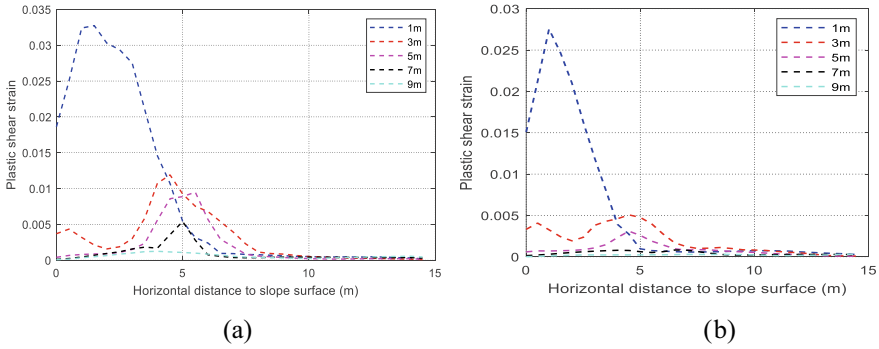


Fig. 4.5 Process of determining the sliding surface position for wave 10: PGA = 0.4 g **a** and wave 100, PGA = 0.4 g **b**

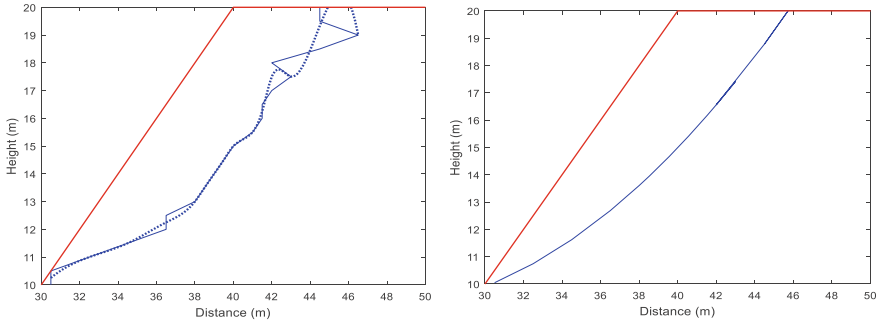


Fig. 4.6 Position of the dynamic slip surface quantified under earthquake action

- (1) The failure sliding surface of the slope continuously develops and only one slip surface can be determined for each ground motion sample.
- (2) During the earthquake, the sliding surface mainly develops from the slope toe to the top, but the top also develops a tensile crack surface in the downward direction. The two sliding surfaces ultimately connect (Sect. 4.3).
- (3) The trend of the shear strain time history is consistent at every monitoring point for a given ground motion acceleration time history, especially near the failure surface. Although the plastic shear strain values are different in Fig. 4.4b, d, and f, the time histories all increase suddenly and level up for the remaining period.

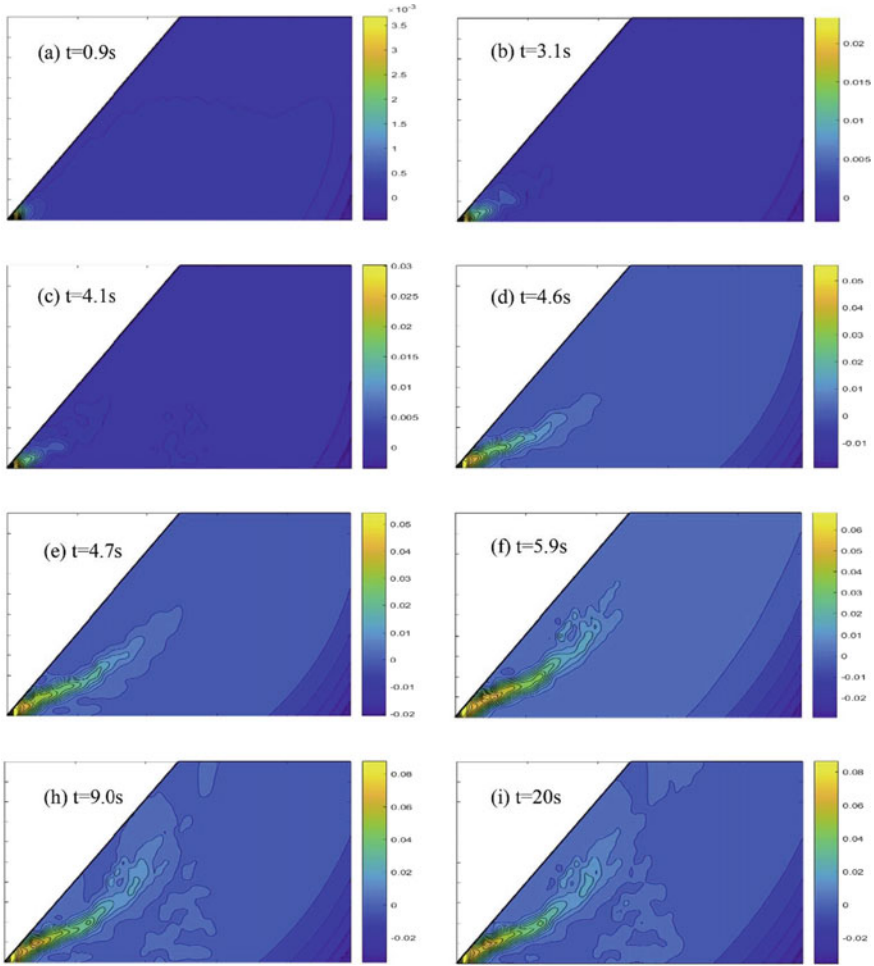


Fig. 4.7 Final plastic strain contours under earthquake action (wave 1, PGA = 0.4 g) (reprinted from Zhao et al. (2020) with permission of Elsevier)

4.2.4 Failure Process Analysis Based on Stochastic Seismic Ground Motion

The characteristics of the slope failure process under stochastic ground motion conditions mainly refer to beginning time, failure accomplishment time, and duration.

In the example presented here, the strain time history was normalized by dividing the final plastic strain for analysis. The failure started when the shear strain achieved 10% of the maximum plastic shear strain, and stopped when the shear strain developed to 90% of the maximum plastic shear strain. The duration was the difference between the beginning time and failure accomplishment time.

Figure 4.8 represents the slope deformation development based on the normalized strain history and strain rate time history. When the shear strain rate fluctuated around zero, the shear strain remained unchanged, which corresponds to failure accomplishment. After checking all the curves, four typical deformation development modes of soil slope can be summarized, as follows.

Figure 4.8a—Type I: Transient slope failure (typically <math>< 0.5\text{ s}</math>). The plastic shear strain curve experienced a large surge under earthquake loading, and the normalized curve of the shear strain rate exhibited an isolated peak.

Figure 4.8b—Type II: Transient slope failure ($\sim 0.5\text{--}1\text{ s}$) with a disconnected process. A short pause occurred in the development of the plastic shear strain, and two or more very close peaks appeared in the normalized curves of the shear strain rates.

Figure 4.8c—Type III: Slope failure is completed in stages over a longer time period ($\sim 2\text{--}4\text{ s}$). The normalized curve of the shear strain rate exhibited several similar peaks.

Figure 4.8d—Type IV: Slope failure took place over a long period of time and was completed in several stages ($>4\text{ s}$), and the normalized shear strain leveled off for more than 2 s during the earthquakes. The plastic shear strain stopped during the earthquakes and the normalized curve of the shear strain rate exhibited two or more completely separate peaks.

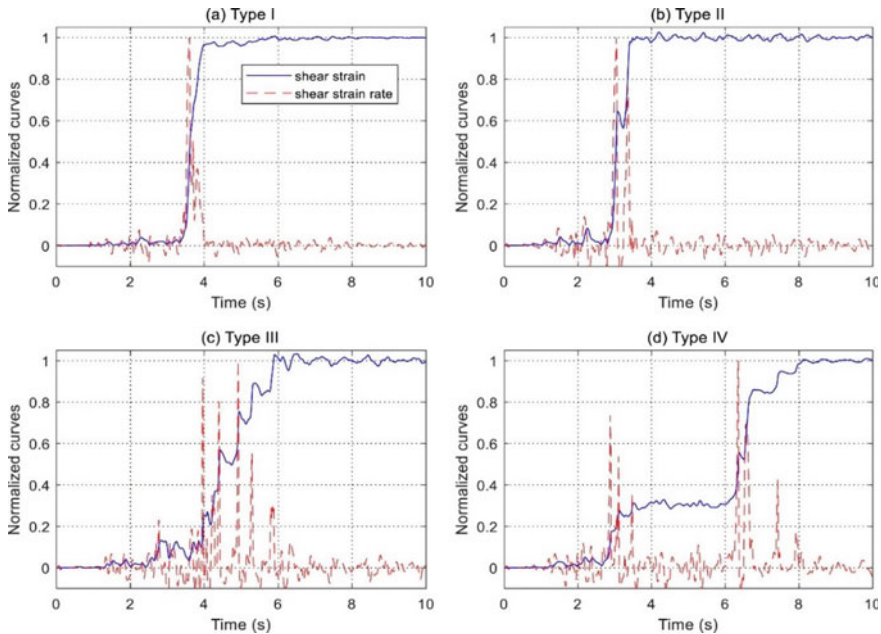


Fig. 4.8 Deformation development patterns of slope based on the normalized shear strain and shear strain rate time history (reprinted from Zhao et al. (2020) with permission of Elsevier)

These four types of deformation development modes have limitations, but they cover almost all the slope outcomes. The number of samples classified as types I and IV was smaller than that of types II and III. Most of the destruction process of an earthquake is therefore completed under several cyclic loads.

4.3 Critical Slip Surface Determination and Landslide Volume Analysis

Previous studies on seismic landslide disasters have shown that the determination of the sliding surface affects the landslide volume (Xu et al., 2016). The relationship between the landslide volume and run-out distance has also been reported in the literature (Peng et al., 2015, 2016).

In the slice method, most slip surfaces are assumed to be circular, which is inaccurate when the slope body is irregular and the material is heterogeneous (Cheng, 2003). A large number of modification schemes based on genetic algorithms and simulated annealing in the search and calculation of non-circular sliding surfaces thus exist (Sun et al., 2008; Zolfaghari et al., 2005). The core of these schemes is to select multiple representative points in a certain area, connect them to form sliding surfaces, and then analyze them based on limit equilibrium. It is also possible to use the nested slices method or modified slices method for dynamic sliding surfaces.

Pre-generated slip surfaces are not necessary for the dynamic strength reduction method, and the factor of safety (FOS) and slip surface position can be simultaneously obtained. The PGA at different points in the same profile can also be used to locate the sliding surface and its development. Similarly, a vertical profile can be set to gradually find the greatest plastic strain point, which ultimately connects into a sliding surface (Zheng et al., 2009).

4.3.1 Model of Slope Stochastic Dynamic Analysis

(1) Model geotechnical parameters

For this equivalent linear slope model, the former shear strain of the unit Gaussian node must be calculated and the shear modulus decay function can be used to update the unit material information (e.g., shear modulus and damping ratio). Using basic parameters, such as soil density and cohesion, the equivalent linear model also requires three material functions for dynamic calculation, which are the G_{max} function, G attenuation function, and damping ratio function. For clayey soil, the G_{max} function is expressed as:

$$G_{max} = 625 \left[\frac{1}{0.3 + 0.7e^2} \right] (OCR)^k \sqrt{P_a \sigma'_m} \quad (4.6)$$

$$k = \frac{PI^{0.72}}{50} \quad (4.7)$$

$$\sigma'_m = \frac{\sigma_v + K_0\sigma_v + K_0\sigma_v}{3} \quad (4.8)$$

where e is the porosity ratio, OCR is the over-consolidation ratio, PI is the soil plasticity index, k is a parameter concerning the plasticity index, which can be calculated using Eq. (4.7), P_a is the reference atmospheric pressure, σ'_m is the average effective stress, which can be calculated using Eq. (4.8) if groundwater is not considered, and σ_v is the overburden earth pressure of the calculated position.

The G attenuation function is calculated using Eq. (4.9) based on the results of Ishibashi and Zhang (1993), and the main parameter is the plasticity index of clay.

$$\frac{G}{G_{max}} = K(\gamma, PI)(\sigma'_m)^{m(\gamma, PI) - m_0} \quad (4.9)$$

$$K(\gamma, PI) = 0.5 \left\{ 1 + \tanh \left[\ln \left(\frac{0.000102 + n(PI)}{\gamma} \right)^{0.492} \right] \right\} \quad (4.10)$$

$$m(\gamma, PI) - m_0 = 0.272 \left\{ 1 - \tanh \left[\ln \left(\frac{0.000556}{\gamma} \right)^{0.4} \right] \right\} \exp(-0.0145PI^{1.3}) \quad (4.11)$$

$$\begin{aligned} n(PI) &= 0.0 && \text{for } PI = 0 \\ n(PI) &= 3.37 \times 10^{-6} PI^{1.404} && \text{for } 0 < PI < 15 \\ n(PI) &= 7.00 \times 10^{-7} PI^{1.976} && \text{for } 15 < PI < 70 \\ n(PI) &= 2.70 \times 10^{-5} PI^{1.115} && \text{for } PI > 70 \end{aligned} \quad (4.12)$$

where γ is the shear strain under cyclic seismic load, and $K(\gamma, PI)$, $m(\gamma, PI)$, $n(PI)$ are functions of the plasticity index of clay.

The soil damping ratio function and shear strain based on Eq. (4.9) can be expressed as:

$$\xi = 0.333 \frac{1 + \exp(-0.0145PI^{1.3})}{2} \left[0.586 \left(\frac{G}{G_{max}} \right)^2 - 1.547 \frac{G}{G_{max}} + 1 \right] \quad (4.13)$$

(2) Stochastic seismic ground motion

The site-based model for producing ground motion was adopted and a total of 508 seismic acceleration histories ground motions were generated. For the equivalent linear analysis model, $\bar{a}_{max} = 0.2g$ is the average PGA, which greatly influences the slope dynamic stability and time-history curve of the safety factor. Huang and Xiong

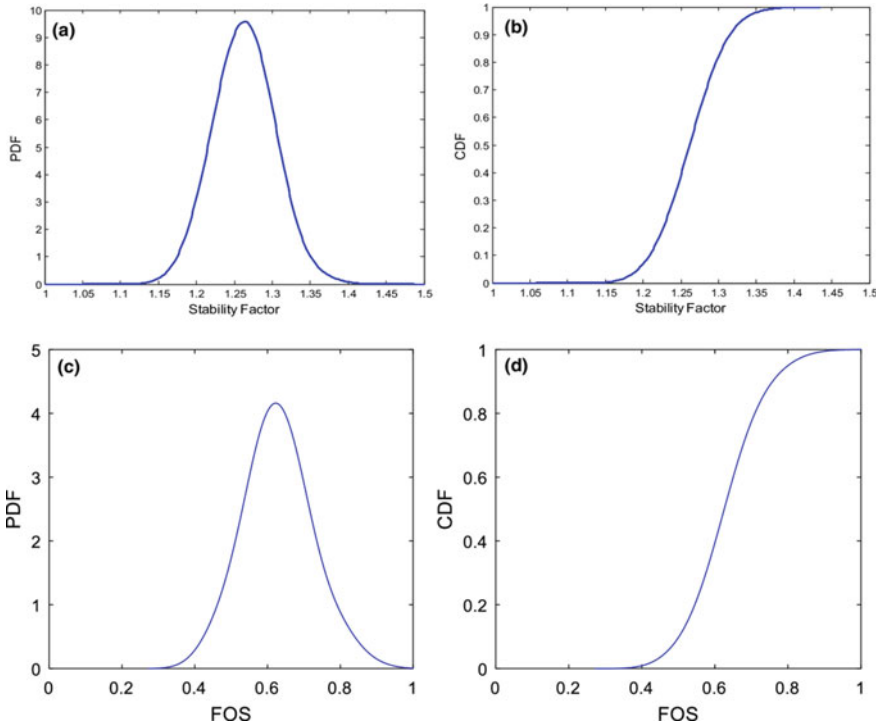


Fig. 4.9 Minimum FOS distributions of a slope under random earthquakes: PDF for PGA = 1 m/s² **a**; CDF for PGA = 1 m/s² **b**; PDF for PGA = 2 m/s² **c** CDF for PGA = 2 m/s² **d** (reprinted from Huang et al. (2018) with permission of Springer)

(2017) used the finite element method and limit equilibrium method (FEM-LEM) to investigation conditions involving a smaller acceleration peak with an average value of $\bar{a}_{max} = 0.1g$. Figure 4.9a shows the PDF and cumulative distribution function (CDF) of the stability factor for an extreme value event, which indicates that the slope would be in a stable state with the smaller peak acceleration. The seismic dynamic reliability is shown in Fig. 4.9b, in which the slope dynamic reliability is close to 1.

The average value of the peak acceleration is adjusted to 0.2 g in this study, and the obtained PDF and CDF of the minimum safety factor are shown in Fig. 4.9c. The minimum safety factor curve obtained from almost all of the ground motion samples is less than 1, which implies that the ground motion samples under this setting value can lead to slope instability, and the damage time and volume of instability can be analyzed and calculated.

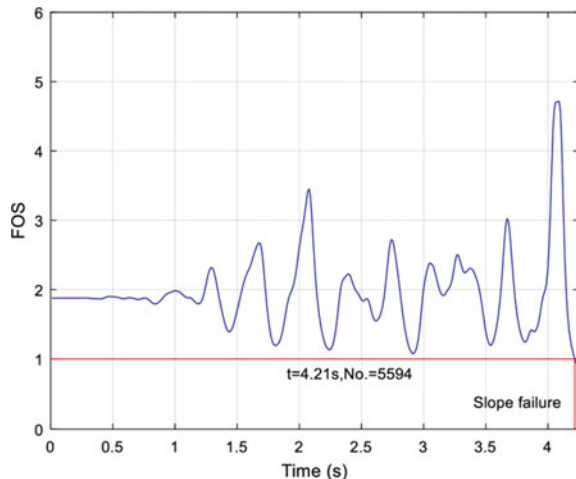
4.3.2 Dynamic Slip Surface and Instability Volume of Slopes

The seismic dynamic instability analysis of soil slopes adopts the failure time and corresponding instability volume based on the time histories curves of the seismic dynamic safety factor.

- (1) The slope instability time refers to the first instance that the safety factor is less than 1 in the time history curve.
- (2) The instability volume refers to the sliding body on the sliding surface corresponding to the slope instability time.

The specific steps are as follows: (1) feed in the representative seismic acceleration time history of wave 1; (2) extract the time history curve of the safety factor; and (3) obtain the corresponding number of sliding surfaces for each time history curve. Once the potential slippery surface is generated, its information (radius, center of circle, and volume) is fixed in the calculation process, which means the information of the coded slippery surface is exactly the same at two different moments. The sliding surface code can therefore be determined once obtaining the sliding time, and the volume can be determined using the information corresponding to the sliding surface code. For example, after inputting the seismic acceleration time history of wave 1 (Fig. 4.10), a sliding time of $t = 4.21$ s is determined, which corresponds to the sliding surface number 5594 and is the most conservative way to identify the most critical sliding surface. Through querying, the sliding volume is found to be 47.713 m^3 for a default thickness of the two-dimensional model of 1 m and the sliding area is 47.713 m^2 .

Fig. 4.10 Computational step of the critical slip surface based on the FOS curve (reprinted from Huang et al. (2018) with permission of Springer)



4.3.3 Evolution Law of Slope Instability Volume

The sliding time and two physical indexes—the instability volume and sliding surface depth—of the corresponding sliding surface were obtained. The reasons for choosing these two indicators are listed as follows.

- (1) The instability volume plays a decisive role in earthquake landslide disasters mainly because there is a high correlation between the instability volume and subsequent disaster scope.
- (2) The sliding surface depth can also represent the magnitude of the landslide volume. The acquisition of the sliding surface depth can thus be beneficial for determining the embedding depth of an anchor and anchor force of a bolt under stochastic seismic ground motion. Different sliding surface depths can be used to determine the different normal stress of the sliding surface.

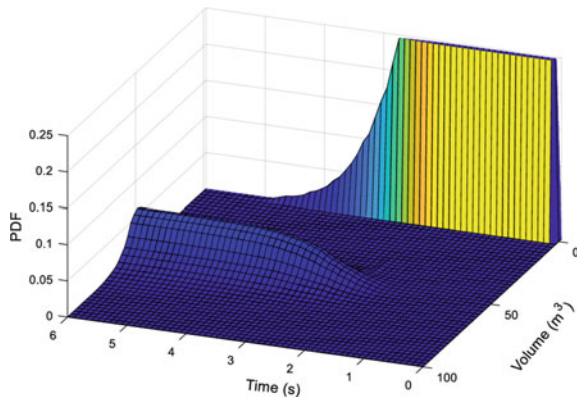
We first obtain the direct result of the instability volume corresponding to the sliding time. The preliminary statistical information of the 508 calculated samples can then be simply obtained by the relationship between the random instability volume and the instability time of homogeneous soil slope. These 508 samples were discretized in the initial probability space, and the sample information provides the basis to solve the probability density function. The evolution law of the obtained physical quantity (volume) is substituted into the probability density evolution equation as follows:

$$\frac{\partial p_{V\theta}(V, \theta, t)}{\partial t} + \dot{V}(\theta, t) \frac{\partial p_{V\theta}(V, \theta, t)}{\partial V} = 0 \quad (4.14)$$

where V represents the instability volume and t represents the earthquake duration.

Figure 4.11 shows the probability density evolution surface of the instability volume calculated using the probability density evolution equation based on the sample information. The diagram shows that there is no slope instability at the initial

Fig. 4.11 Probability density evolutionary surface of the landslide volume (reprinted from Huang et al. (2018) with permission of Springer)



time, and that the probability exerts a maximum value when the volume is zero. As the earthquake activity continues, some samples begin to be damaged and the probability value of the samples with zero volume (indicating safety) begins to decrease. After approximately 5 s, all the samples fail, the probability value is 0 when the volume is 0, and the unstable volume mainly concentrates around 50 m³. The three-dimensional probability density evolution surface directly reflects the uncertainty of slope failure under random earthquake action, which includes the uncertainty of the sliding volume and sliding depth.

4.3.4 Stochastic Seismic Risk Assessment of Slope

The existing methods of risk assessment usually involve equivalent extreme events or the first crossing method, which generally consider physical quantities such as acceleration, displacement, or the unstable volume. If the equivalent extreme events are referred, the maximum sliding volume of each seismic input can be used for analysis. Owing to the monotony of the volume research process, the value of the sliding volume and truncated random variable at the sliding completion time are identical. For example, all the sliding volume distributions at $t = 10$ s can be taken for analysis. All the samples have therefore been destroyed at this moment, and the volume distribution at this time can be considered the final state.

The randomness of the final sliding volume calculated by FEM-LEM coupling is analyzed. Figure 4.12 shows the probability density evolution method (PDEM) analysis and Monte Carlo Method (MCM) simulation analysis of the final instability volume of homogeneous soil slope. The volume distribution in Fig. 4.12 can also be used as a reference for seismic landslide hazard assessment. The seismic landslide volume is closely related to the run-out distance and disaster-causing range, and is generally believed to be proportional to the landslide volume (Li & Chu, 2016; Liu et al., 2017; Zhang & Huang, 2016). The risk of a landslide disaster can be estimated if the sliding volume is multiplied by the potential property loss per unit volume.

The ultimate purpose of studying seismic stability is seismic design. Therefore, in addition to considering the randomness of the instability volume, the position of the slope failure surface and depth of the sliding surface are all essential parameters, which provide a reference for the design of support structures. Three to five samples of ground motion are far from sufficient for current design specifications, and the sliding surface depth varies greatly from 4 to 8 m (Fig. 4.13). For this model, the sliding depth considering the static action is approximately 5.168 m. The sliding depth may therefore be underestimated when using small data samples. If the anchor bolt length and embedded depth of the anti-sliding pile are insufficient in the final design, the failure probability under earthquake will be greatly increased.

If stochastic seismic dynamic analysis is used, the engineer can be informed of all the slope sliding possibilities under seismic action, which will reduce the design defect if the anchor depth is directly embedded in stable rock. Stochastic seismic dynamic analysis can therefore present a completely different idea for seismic design.

Fig. 4.12 Landslide volume uncertainty calculated by the MCM and PDEM: **a** PDF; **b** CDF (reprinted from Huang et al. (2018) with permission of Springer)

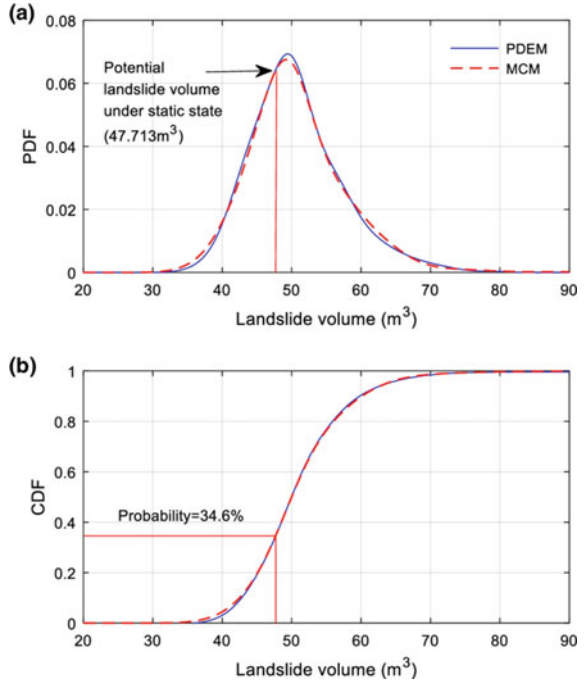


Fig. 4.13 Landslide depth uncertainty: PDF **a**; CDF **b** (reprinted from Huang et al. (2018) with permission of Springer)

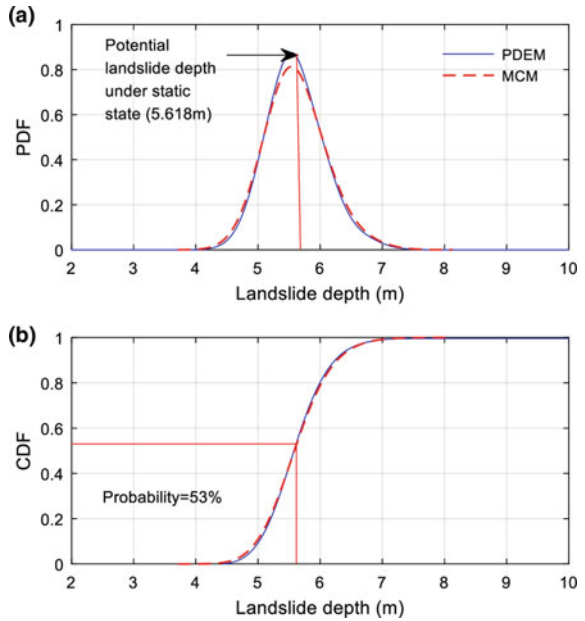
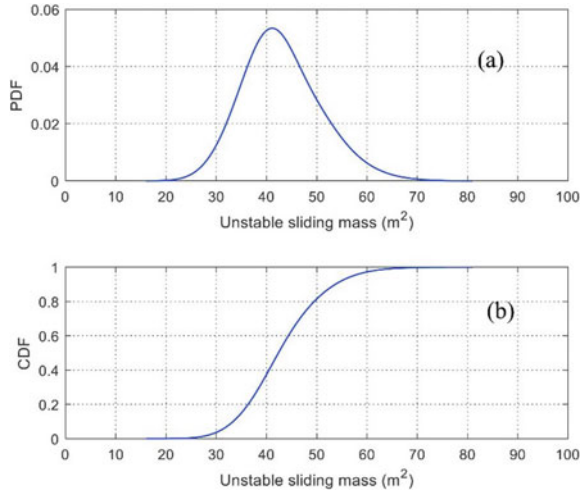


Fig. 4.14 Sliding volume determined by the plastic strain increment method (reprinted from Zhao et al. (2020) with permission of Elsevier)



The actual failure of an earthquake-triggered landslide occurs mostly owing to lower shear-upper tensile fracturing. The role of the top tensile fracture zone should thus be considered based on plastic shear strain slip surface in Sect. 4.3.4.

The specific seismic dynamic state of the sliding surface is not yet determined after the sliding surface connects, and the slope may simply produce several cracks. Using the above method, the area of the unstable sliding region is calculated for all the ground motion samples. The PDF of the unstable sliding body is obtained by the PDEM, as shown in Fig. 4.14. The plane strain analysis indicates that the sliding region is mainly 25–75 m³ with an average of 42 m³.

The unstable volume should therefore also be used as a relevant index to evaluate the seismic landslide risk. The random instability analysis method presented in this section is of great importance to the seismic design of slope engineering.

4.4 Slope Post-failure Behavior Under Random Earthquake Based on Smoothed Particle Hydrodynamics

The seismic dynamic analysis of the first two stages has been previously presented regarding the mechanism and process. In the slope failure process, when soil particles move rapidly and their state changes from elastic to plastic, the stress–strain relationship is no longer in line with the small deformation assumption and enters the large deformation stages. Such disasters (e.g., landslides and debris flows) move quickly and affect a wide region, which often leads to the damage or burial of buildings, transportation facilities, and other structures, which can directly threaten human life. For example, a catastrophic landslide disaster occurred suddenly in Maoxian County

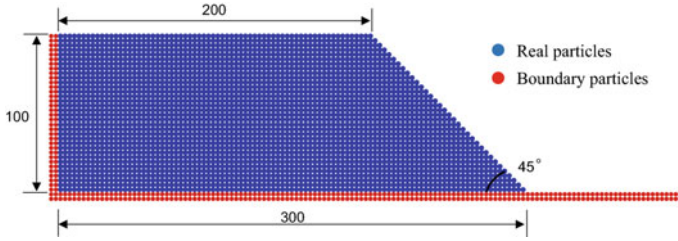


Fig. 4.15 Homogeneous ideal slope model (units: m) (reprinted from Huang et al. (2020) with permission of Springer)

of Sichuan Province in June 2017. The sliding volume was approximately $1.300 \times 10^6 \text{ m}^3$ and the run-out distance was approximately 2.6 km. In April 2007, the Tibet Yi Gong mountain collapsed, producing a landslide volume of $3 \times 10^8 \text{ m}^3$ and run-out distance of more than 6 km, which caused economic losses of approximately 14 million yuan.

The run-out distance is positively relevant to the landslide volume (Okura et al., 2000). Numerous studies have applied slope dynamics reliability analysis with different stochastic factors, such as soil spatial anisotropy (Jiang et al., 2015), horizontal seismic coefficients, and soil unit weights (Johari & Khodaparast, 2015). In this section, the post-failure behavior under random earthquake action is quantitatively analyzed based on smoothed particle hydrodynamics.

4.4.1 SPH Model of Soil Flow Hazards

According to existing reports of slope reliability analysis, Huang et al. (2020) established a two-dimensional ideal slope model to evaluate the large deformation of slopes after an earthquake event (Fig. 4.15). The slope height in this example is 20 m, the top width is 22 m, and the slope angle is 45° . The model is composed of 4767 particles, including 4080 soil particles (blue) and 687 boundary particles (red). Some of the parameters of the ideal slope model are specific listed here: density $\rho = 1850 \text{ kg/m}^3$; elastic modulus $E = 500 \text{ MPa}$; Poisson's ratio $\nu = 0.3$. There are 2873 real particles and 406 boundary particles, which share the same parameters. The artificial viscosity parameter a is 1, the artificial viscosity parameter k is 0.01, the artificial stress parameter ε is 0.3, the time step is 10^{-4} s , and the ratio between the smooth length and particle spacing is 1.2.

4.4.2 Simulation of Random Field

The specific steps of the lognormal random field simulation that link the cohesive force c and internal friction angle φ are described as follows.

- (1) Determine the detailed statistical characteristic of c and φ , including the probability distribution, average value, coefficient of variation, autocorrelation distance, and correlation number.
- (2) Determine the subdivision grid of the two-dimensional random field. To simplify the calculation, the grids are generally selected to be consistent with the particles in the SPH model.
- (3) Select the form of the autocorrelation function, obtain its eigenvalues and eigenvectors by the numerical method, and arrange them according to the size of the eigenvalues.
- (4) Calculate the cross-correlation matrix $R_{1,2}^0$ of the standard normal random field according to Eqs. (4.8) and (4.9), and use Latin hypercube sampling to generate the independent standard normal random variable $\varepsilon_n(\theta)$ (Jiang et al., 2014). On this basis, Eq. (4.10) is used to calculate the related standard normal random variable $\varepsilon_n(\theta)$.
- (5) Generate sample points of the cohesive force c and internal friction angle φ according to the probability space subdivision of the basic random variables, and use Eqs. (4.13) and (4.14) to discretize the relevant lognormal random fields.

According to the above steps, the basic random variable space was divided and 226 representative points were obtained considering the Sobol point set (Radovic et al., 1996). Using the inverse transformation method and generalized F deviation optimization, the lognormal distribution random field is generated, to which c and φ are related. The statistical characteristics of c and φ (Cho, 2010) are presented in Table 4.2. Combined with the particle distribution information in the SPH calculation model, the random field is divided into 4767 nodes, and the soil parameters of each node are assigned to each particle. The average values of c and φ are taken as an example, and the related lognormal random field is simulated. As shown in Figs. 4.16 and 4.17, the value of the soil parameters changes with changing location. On the basis of the probability space subdivision of the random variables, the random field of the statistical characteristic value of different c and φ values is discretized, and a finite number of the sample collection is obtained, which reflects the geological reality of the soil parameters.

Table 4.2 Statistical characteristics of soil parameters

Parameter	Distribution type	Average value	Coefficient of variation	Autocorrelation distance	Cross correlation coefficient
Cohesive force	Lognormal distribution	10 kPa	0.3	$l_x = 20\text{ m}$ $l_y = 20\text{ m}$	$\rho_{c\varphi} = -0.25$
Internal friction angle	Lognormal distribution	20°	0.2		

Fig. 4.16 Realization of a stochastic field of the cohesive force

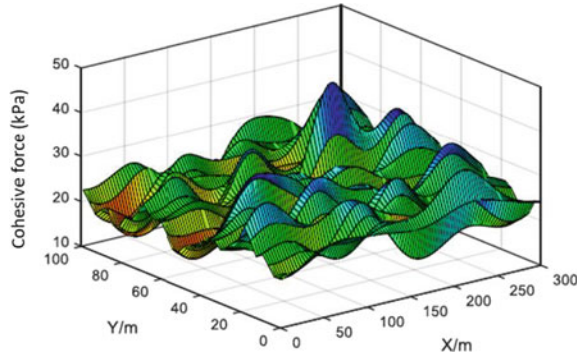
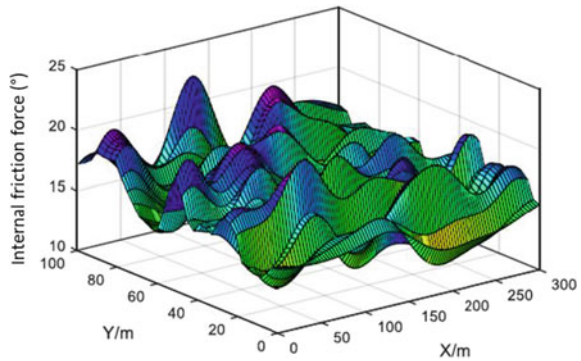


Fig. 4.17 Realization of a stochastic field of the internal friction force



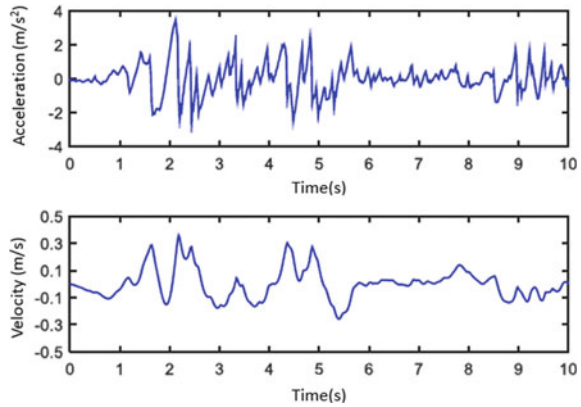
4.4.3 Large Deformation Analysis of Soil Flow Hazards

Referring to Karhunen-Loève series expansion method, the corresponding sample set is produced after generating the lognormal random field to which the c and φ are related. A series of SPH calculation samples were generated under dynamic conditions, in combination with the SPH model in Sect. 4.4.1. The SPH governing equation was solved via batch processing to obtain the deterministic calculation results. The finite difference numerical method was then used to handle the GDEE equation. The PDFs of the flow slip parameters considering of the soil spatial variability were obtained, and large deformation analysis of soil flow hazards was carried out.

There are many format differences when solving GDEE equations. A comparison of three aspects (convergence, compatibility, and stability) shows that the total variation diminishing (TVD) bilateral difference scheme reduces the dissipation, suppresses the dispersion by applying a flux limit, offers the advantages of unilateral and bilateral format differences format of Lax-Wendroff (LW), and calculates the convergence faster with high precision.

The ground motion adopts the El Centro wave, ground motion acceleration, and velocity time history curve, as shown in Fig. 4.18. The SPH simulation process is

Fig. 4.18 Time history curve of ground motion

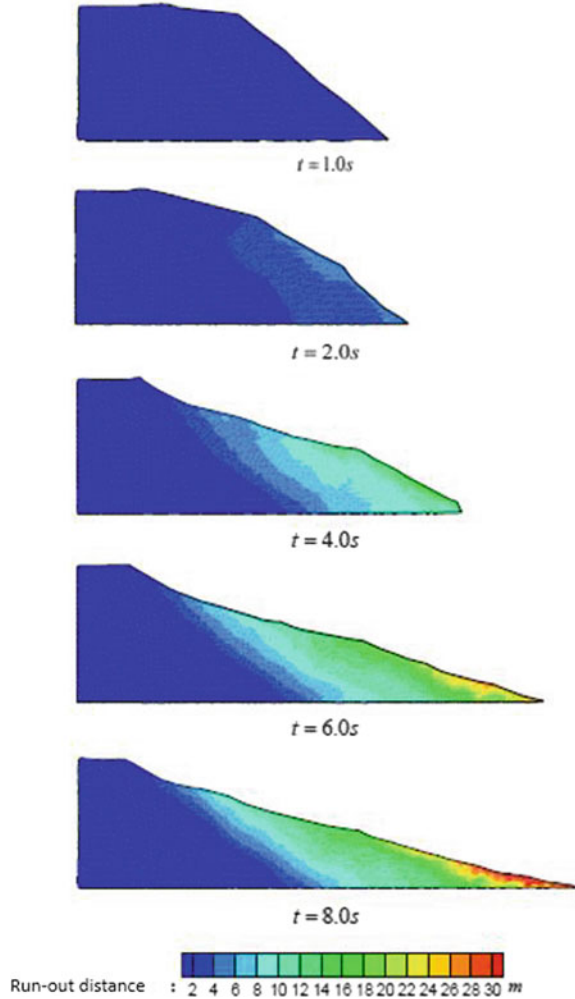


shown in Fig. 4.19. When $t = 1.0$ s, the slope began to exhibit large deformation. Under the action of ground motion, the sliding distance increased until $t = 8$ s, and the run-out distance eventually reached 32.4 m.

The time history curves of the mean and standard deviation values of the flow slip parameters were obtained by analyzing the SPH simulation results. Taking the run-out distance as an example, when $t = 10$ s, the maximum value was 57.8 m, which is more than seven times greater than the minimum value (8.8 m) with an average of 19.4 m. Figure 4.20 highlights the growth of the mean and standard deviation with time. The reason for this increase is that slope began to slip under the earthquake action, and the average run-out distance increased with gradually appearing differences. For example, the flow depth of the area 5 m from the slope toe reached a minimum value of 1.8 m at $t = 10$ s, which is greater than one-third of the maximum value (6.3 m), with a mean of 4.1 m and standard deviation of 0.82. Figure 4.21 depicts the time history curve of mean and standard deviation of flow depth in that section. When $t < 2$ s, the average flow depth is 0, showing that the run-out distance is < 5 m. When $2 < t < 8$ s, the mean flow depth value increases with time, showing that the soil moved during in the large deformation flow process. When $t > 8$ s, the mean flow depth value remains unchanged, which indicates that the large deformation and soil movement had ceased. When $2 < t < 8$ s, the standard deviation of the flow depth exhibits a peak, which indicates an initial increase and then decrease, and illustrates the influence of the soil spatial variability. The large-deformation soil flow disaster shows notable differences, and the discreteness of the flow depth initially increases and then decreases.

The GDEE equation was solved to obtain the probabilistic evolution process and characteristics of the flow-slip parameters. Using the equivalent extreme events, the corresponding virtual process was constructed to obtain the PDF and CDF curves of the flow slip parameters. Figure 4.22 shows the PDF curve of the run-out distance at three typical moments, taking the sliding distance as an example. The PDF of the run-out distance clearly no longer follows a lognormal distribution, which indicates complex mapping between the input and output of the random slope system. When

Fig. 4.19 SPH simulation process



$t = 3.5$ s, the run-out distance distribution ranges between 0 and 12 m, and the peak PDF is 0.3584. When $t = 4.5$ s, the run-out distance is between 1 and 17 m, and the peak PDF is 0.2316. When $t = 5.5$ s, the run-out distance is mainly distributed between 4 and 23 m, and the peak PDF is 0.1406.

Figure 4.23 intercepts the curved surface of the probability density variation of the run-out distance between 3 and 5 s, which demonstrates the complex changing process of the PDF. Figure 4.24 is an equal-probability density plot of the run-out distance, which is the horizontal projection of Fig. 4.26. Where the curves are dense in the figure, the PDF values change rapidly. In contrast, when the curves are sparse, the PDF values change slowly.

Fig. 4.20 Mean and standard deviation time-history curves of the run-out distance considering spatial variability

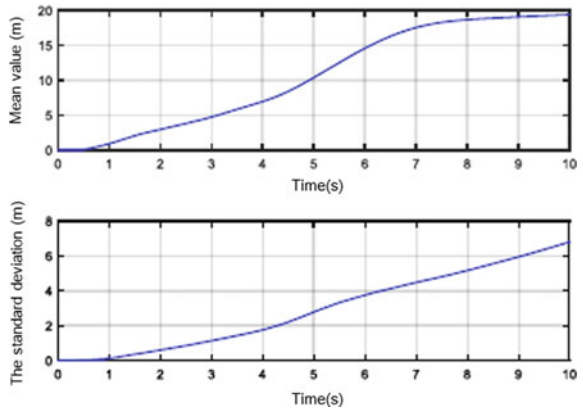


Fig. 4.21 Mean and standard deviation time-history curves of the flow depth considering spatial variability

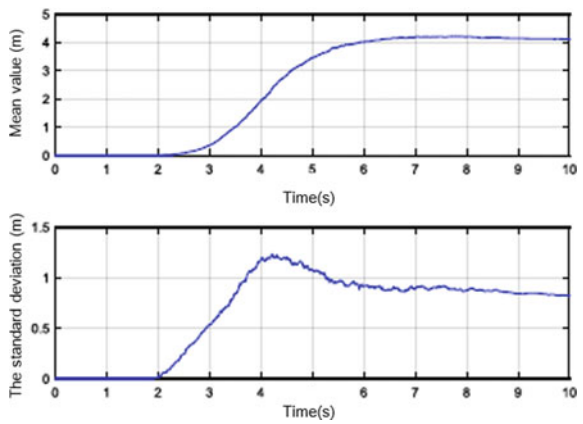


Fig. 4.22 PDF curve of run-out distance under typical moments considering spatial variability

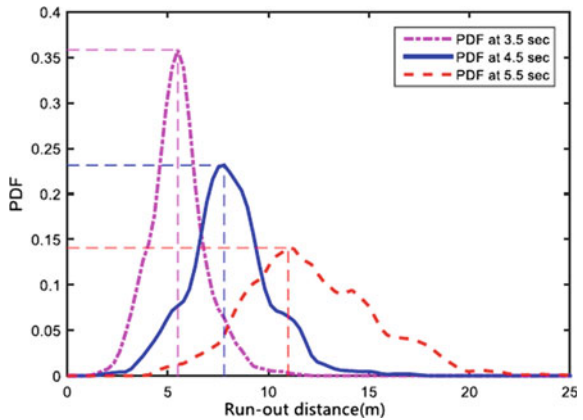


Fig. 4.23
Three-dimensional surface of the probability density variation of run-out distance considering spatial variability

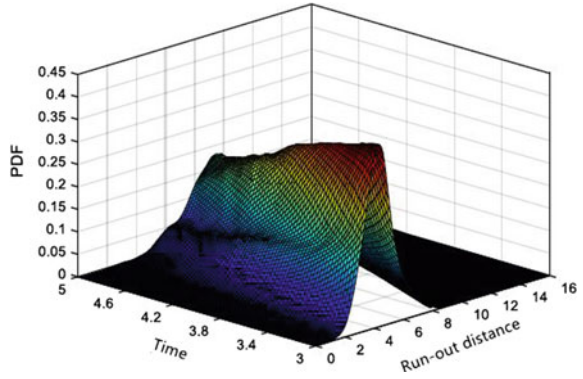


Fig. 4.24 Equal-probability density plot of the run-out distance considering spatial variability

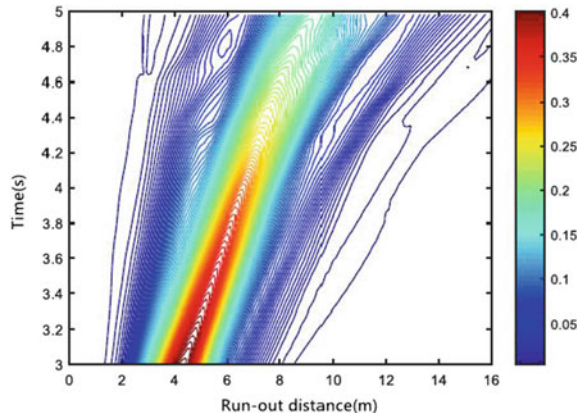


Fig. 4.25 PDF curve of the run-out distance considering spatial variability

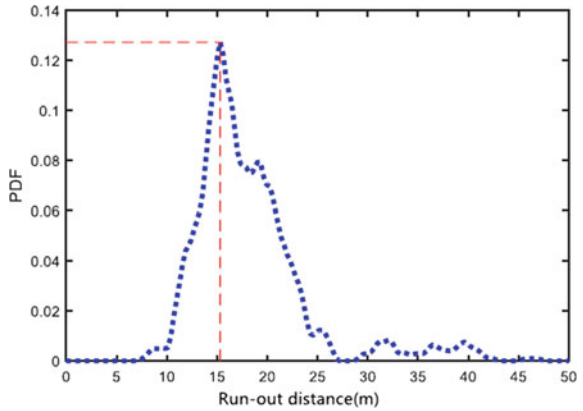
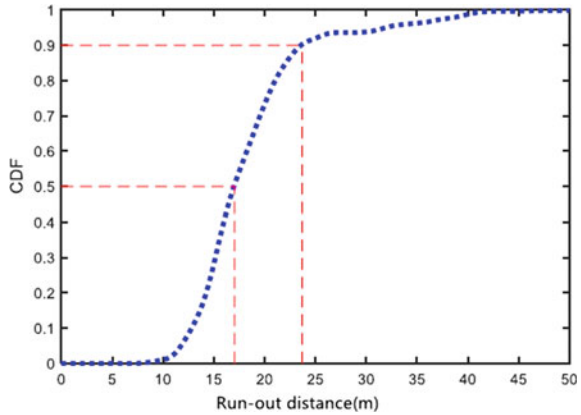


Fig. 4.26 CDF curve of the run-out distance considering spatial variability



The PDF and CDF curves of the final sliding distance were obtained based on the equivalent extreme events, as shown in Figs. 4.25 and 4.26, respectively. The run-out distance ranges from 7 to 43 m and the peak PDF is 0.1274, which corresponds to a sliding distance of 15.3 m. The probability of a run-out distance greater than 17.1 m is approximately 50%, and the probability of a sliding distance less than 23.7 m is 90%. Similarly, the PDF and CDF curves for the flow depth can be obtained, as shown in Figs. 4.27 and 4.28, respectively. The flow depth is distributed between 1.5 and 6.0 m, the peak PDF is 0.7690, and the corresponding flow depth is 4.0 m. The probability of the flow depth more than 4 m is about 50%, and the probability of the flow depth less than 4.8 m is 90%.

Fig. 4.27 PDF curve of the flow depth considering spatial variability

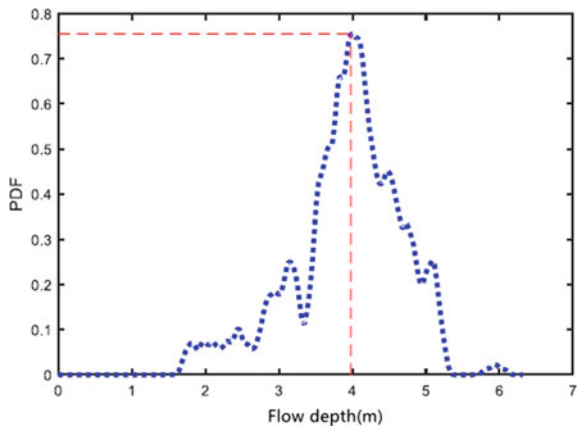
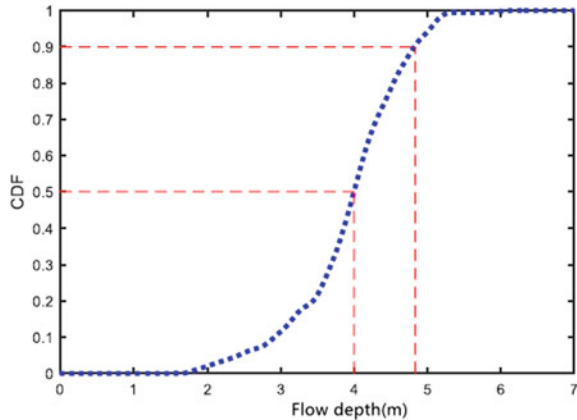


Fig. 4.28 CDF curve of the flow depth considering spatial variability



References

- Ambraseys, N. N. (1995). The prediction of earthquake peak ground acceleration in Europe. *Earthquake Engineering & Structural Dynamics*, 24(4), 467–490.
- Ambraseys, N. N., & Simpson, K. A. (1996). Prediction of vertical response spectra in Europe. *Earthquake Engineering & Structural Dynamics*, 25(4), 401–412.
- Aoi, S., Kunugi, T., & Fujiwara, H. (2008). Trampoline effect in extreme ground motion. *Science*, 322(5902), 727–730.
- Cheng, Y. M. (2003). Location of critical failure surface and some further studies on slope stability analysis. *Computers and Geotechnics*, 30(3), 255–267.
- Cho, S. E. (2010). Probabilistic assessment of slope stability that considers the spatial variability of soil properties. *Journal of Geotechnical and Geoenvironmental Engineering*, 136(7), 975–984.
- Elgamal, A., & He, L. C. (2004). Vertical earthquake ground motion records: An overview. *Journal of Earthquake Engineering*, 8(5), 663–697.
- Elnashai, A. S., & Papazoglou, A. J. (1997). Procedure and spectra for analysis of rc structures subjected to strong vertical earthquake loads. *Journal of Earthquake Engineering*, 1(1), 121–155.
- Geli, L., Bard, P. Y., & Jullien, B. (1988). The effect of topography on earthquake ground motion—a review and new results. *Bulletin of the Seismological Society of America*, 78(1), 42–63.
- Huang, Y., Li, G. Y., & Xiong, M. (2020). Stochastic assessment of slope failure run-out triggered by earthquake ground motion. *Natural Hazards*, 101(1), 87–102.
- Huang, Y., Mao, W., Zheng, H., et al. (2012). Computational fluid dynamics modeling of post-liquefaction soil flow using the volume of fluid method. *Bulletin of Engineering Geology and the Environment*, 71(2), 359–366.
- Huang, Y., & Xiong, M. (2017). Dynamic reliability analysis of slopes based on the probability density evolution method. *Soil Dynamics and Earthquake Engineering*, 94, 1–6.
- Huang, Y., Zhao, L., Xiong, M., et al. (2018). Critical slip surface and landslide volume of a soil slope under random earthquake ground motions. *Environmental Earth Sciences*, 77(23).
- Jiang, S., Li, D., Cao, Z., et al. (2015). Efficient system reliability analysis of slope stability in spatially variable soils using Monte Carlo simulation. *Journal of Geotechnical and Geoenvironmental Engineering*, 141(2).
- Jiang, S., Li, D., Zhou, C., et al. (2014). Slope reliability analysis considering effect of autocorrelation functions. *Chinese Journal of Geotechnical Engineering*, 36(3), 508–518.
- Jiao, Y., Tian, H., Wu, H., et al. (2015). Numerical and experimental investigation on the stability of slopes threatened by earthquakes. *Arabian Journal of Geosciences*, 8(7), 4353–4364.

- Johari, A., & Khodaparast, A. R. (2015). Analytical stochastic analysis of seismic stability of infinite slope. *Soil Dynamics and Earthquake Engineering*, 79, 17–21.
- Li, L., & Chu, X. (2016). Risk assessment of slope failure by representative slip surfaces and response surface function. *Ksce Journal of Civil Engineering*, 20(5), 1783–1792.
- Liu, L., Cheng, Y., Wang, X., et al. (2017). System reliability analysis and risk assessment of a layered slope in spatially variable soils considering stratigraphic boundary uncertainty. *Computers and Geotechnics*, 89, 213–225.
- Ishibashi, I., & Zhang, X. (1993). Unified dynamic shear moduli and damping ratios of sand and clay Soils and Foundations, 33, 182–191.
- Meunier, P., Hovius, N., & Haines, J. A. (2008). Topographic site effects and the location of earthquake induced landslides. *Earth and Planetary Science Letters*, 275(3–4), 221–232.
- Okura, Y., Kitahara, H., Sammori, T., et al. (2000). The effects of rockfall volume on runout distance. *Engineering Geology*, 58(2), 109–124.
- Pastor, M., Manzanal, D., Fernandez Merodo, J. A., et al. (2010). From solids to fluidized soils: Diffuse failure mechanisms in geostuctures with applications to fast catastrophic landslides. *Granular Matter*, 12(3), 211–228.
- Peng, J., Fan, Z., Wu, D., et al. (2015). Heavy rainfall triggered loess-mudstone landslide and subsequent debris flow in Tianshui, China. *Engineering Geology*, 186, 79–90.
- Peng, J., Leng, Y., Zhu, X., et al. (2016). Development of a loess-mudstone landslide in a fault fracture zone. *Environmental Earth Sciences*, 75(8).
- Prime, N., Dufour, F., & Darve, F. (2014a). Solid-fluid transition modelling in geomaterials and application to a mudflow interacting with an obstacle. *International Journal for Numerical and Analytical Methods in Geomechanics*, 38(13), 1341–1361.
- Prime, N., Dufour, F., & Darve, F. (2014b). Unified model for geomaterial solid/fluid states and the transition in between. *Journal of Engineering Mechanics*, 140(6).
- Radovic, I., Sobol, I. M., & Tichy, R. F. (1996). Quasi-Monte Carlo methods for numerical integration: comparison of different low discrepancy sequences. *Monte Carlo Methods and Application*, 2, 1–14.
- Sun, J., Li, J., & Liu, Q. (2008). Search for critical slip surface in slope stability analysis by spline-based GA method. *Journal of Geotechnical and Geoenvironmental Engineering*, 134(2), 252–256.
- Wang, H., & Xie, L. (2010). Effects of topography on ground motion in the Xishan park, Zigong city. *Chinese Journal of Geophysics-Chinese Edition*, 53(7), 1631–1638.
- Xu, C., Xu, X., Shen, L., et al. (2016). Optimized volume models of earthquake-triggered landslides. *Scientific Reports*, 6.
- Zhang, J., & Huang, H. W. (2016). Risk assessment of slope failure considering multiple slip surfaces. *Computers and Geotechnics*, 74, 188–195.
- Zhao, L., Huang, Y., Chen, Z., et al. (2020). Dynamic failure processes and failure mechanism of soil slope under random earthquake ground motions. *Soil Dynamics and Earthquake Engineering*, 133.
- Zheng, H., Sun, G., & Liu, D. (2009). A practical procedure for searching critical slip surfaces of slopes based on the strength reduction technique. *Computers and Geotechnics*, 36(1–2), 1–5.
- Zolfaghari, A. R., Heath, A. C., & McCombie, P. F. (2005). Simple genetic algorithm search for critical non-circular failure surface in slope stability analysis. *Computers and Geotechnics*, 32(3), 139–152.

Chapter 5

Nonlinear Stochastic Dynamic Seismic Response Analysis of Slopes Based on Large Shaking Table Tests



The shaking table physical model testing method is a significant approach for studying the mechanism and modes of structural earthquake failure, evaluating the overall seismic resistance of structures, and measuring the effects of seismic reduction and isolation. The numerical methods of dynamic analysis have advanced in recent years. However, the uncertainties of numerical models and material parameters are becoming an important topic for the validation of results, so that it develops a strong requirement for experimental confirmation with appropriate boundary conditions that are same as the virtual models. This is particularly true when a structure behaves plastically or includes elements whose behavior shows a strong correlation with different load properties, especially seismic excitations. Here we use a dynamical system in which a function is applied to describe the time dependence characteristics of certain points in a geometrical domain. Considering the time dependent and stochastic properties of seismic excitations, the slope should be regarded as a stochastic dynamical system when investigating the randomness of ground motions. In a slope dynamical system, the description on the dynamic characteristics should involve the propagation and spatio-temporal evolution of the kinetic indicators that are assessed using probability (e.g., velocity, acceleration, and displacement). The factors of stability and amplifying effect are significant concerns under stochastic dynamical excitation conditions. The final illustration helps to visualize these effects in an evolutionary method using probability density function (PDF) curves.

Earthquake stochastic dynamic tests were originally based on field tests. Earthquake observation instruments were first set on building structures or slopes, and the dynamic characteristics of these structures or slopes would be measured when an earthquake stimulation was captured by the instruments. However, field prototype tests cannot meet the needs of seismic research owing to the limited number of strong earthquakes and long interim periods. The construction of indoor seismic simulation equipment was therefore proposed, such as shaking tables and centrifuges. A large amount of data can be obtained using such indoor physical methods, and the period over which the data are obtained is greatly shortened.

Shaking table tests loaded with earthquake waves were first used in the 1940s to simulate the seismic behavior of civil engineering structures. The scaling and amount increased substantially by the 1960s. A horizontal and vertical simultaneous seismic simulation shaking table was established by the Institute of Industrial Technology of the University of Tokyo in 1966. Vibrating tables with electromagnetic driving methods began to appear in the late 1960s, such as the seismic simulation shaking table built at the University of Illinois in 1968 (3.65×3.65 m), one built at the University of Tokyo in 1966 (10×2 m), and one of the earliest earthquakes simulating shakers built at the Central Research Institute of Japan Electric Power in 1968 (6×6.5 m).

Prior to 1971, the shakers would vibrate in one direction or switch between horizontal and vertical motion. The degrees of freedom (DOF) did not increase until the seismic simulation shaking table at the University of California, Berkeley was first established. The control system of multi-dimensional earthquake simulation shaking tables is more complicated not only because control must be considered in different directions, but also to consider the influence of coupling effects.

Advances in mechanical system control practices increased with the development of the signal controlling theorem, which contains two popular control techniques: proportion integral differential (PID) control based on displacement; and supply-feedback control using displacement, velocity, and acceleration. However, in 1975, the numerical control method, especially the position sensitive detector control method, was adopted to achieve seismic excitation reproduction wider frequency bands. The position sensitive detector controller can dynamically change the controller parameters according to the system error to achieve adaptive control. In the mid 1990s, the seismic simulation shaker control system was manipulated by both digital and simulation methods; the former contributed to the compensation of control signals and the latter ensured the stability, accuracy, broadband, anti-interference, and linear characteristics of the control system. In this chapter, a large-scale shaking table test is conducted to study the dynamic response of slope under stochastic ground motions, where 144 artificial seismic acceleration time-history samples are generated and demonstrated adopting a spatial evolution power spectrum technique (Zhao et al., 2020).

The purpose of this physical test is to reveal the stochastic nonlinear seismic response rules of slope, and to validate the numerical simulation results using the obtained experimental data. The design of the model box and materials, similarity laws, seismic excitations, loading schemes, monitoring system, and the model production procedures are introduced in detail. The acceleration evolves following the trend that the PDF value changes spatiotemporally in the shaking table test. In the temporal domain, the PDF value initially increases and then decreases after a boost of the progression of the seismic power spectrum. In the spatial range, the PDF value increases upslope in the nonlinear manner, which implies that the mean and standard deviation (MSD) of the amplifying factors increases with elevation following some high-order function (Zhao et al., 2020). The processing of the detailed dataset shows that the factor of safety (FOS) of the upper slope is inferior, and a de-amplifying effect

is recognized at the slope toe under these seismic excitations. Different amplifying factors and the applications of these factors in slope engineering are also discussed in this chapter.

5.1 Model Design for Large Shaking Table Test

With the rise of the infrastructure industry, shaking table tests have become increasingly common in studies of the seismic performance and mechanism of large hydraulic structures, civil engineering structures, nuclear power plants, and other constructions and facilities. These experimental results are good indicators that can verify the validity of computational modeling outcomes. However, research on the geotechnical surroundings and infrastructures within hazardous subgrade regions remains insufficient, especially with regard to the dynamic response under seismic excitations. New analysis methods are being put forward based on the temporally and spatially related evolution characteristics. The uncertainty of seismic ground motions and indistinction on constitutive models of geotechnical materials and structures suggest that probability density functions are one of the best options for overcoming this insufficiency. On the basis of the significance and fact that this uncertainty has seldom been studied in terms of slope seismic response using shaking table tests, this chapter investigates the nonlinear stochastic seismic dynamic response of a slope shaking table test. In mechanical systems, significant similarity matters in terms of geometrics, kinematics, and dynamics of slope models should be addressed, and are therefore introduced throughout the procedure. The similarity law is fully considered in the overall steps.

- (1) Size determination of test model
- (2) Model materials production
- (3) Model construction and measurement
- (4) Seismic excitation generation.

5.1.1 *Size Determination of Slope Model*

The dimension parameters of the prototype include length, width, and height, and should altogether be reduced or enlarged into a model size in some proportion that is called the similarity ratio. The similarity ratio of a slope physical test mainly depends on the purpose of the test, and considers the bearing capacity of the shaker to compare the studied region of the prototype and the model box size.

The shaking table system is located at the Multifunctional Vibration Experimental Center of the State Key Laboratory of Disaster Prevention and Mitigation in the School of Civil Engineering at Tongji University. The shaking table system contains four 4×6 m shaking tables, and one of the largest shakers has a global capability of more than 200 tons. Notably, one 30-ton shaker used in this slope model

Table 5.1 Pivotal parameters of the shaking table

		Parameters	
Geometry	4 × 6 m		
Capacity	30 T		
Frequency	0.1–50 Hz		
DOF	3		
Maximum value	Item and direction	X	Y
	Acceleration	1.2 g	0.8 g
	Velocity	1000 mm/s	600 mm/s
	Displacement	100 mm	50 mm

is sufficient to effectively capture the slope dynamic response with the assistance of well-operating sensors. Essential differences exist between slope engineering and building structures. The research scope of slopes and hazardous landslides consist of a geotechnical loose medium and continuum (e.g., earth, rocks) without a macroscopic bridging capacity. There is therefore no need to engage multi-point shaker coupling, which was originally adopted to investigate the seismic response of structures or bridges with regularly arranged columns and piers. The shaking table in the study of slope lithology simulates in the same manner as single point shaking table tests. Using a combination of materials with relatively high stiffness and low deformation and with the design aim to reuse the slope model, the test requires a rigid model box to simulate lithological boundaries that can resist deformation. Once the shear model box is used, destructive tests are commonly conducted, and soft and deformable soil materials should also be accommodated.

(1) Parameters of shaking table model

The composition of the model box covers a combination of experimental purposes, shaking table size, and shaker capacity. Table 5.1 lists the pivotal characteristics of the 30-ton shaker. In terms of the model box and shaker configuration, there is a threaded hole on the rigid model box with a 36-mm diameter, and the spacing density is 500 mm.

Table 5.2 lists some of the relevant references for the rigid model box geometry in this test, and Table 5.3 lists the model box parameters used for comparison. The shaking table size limit was shown in previous experiments to be generally within 4 m in length. The appearance length of the rigid box used in the test demonstrated here is 3.6 m and the net length is 3.4 m. The design of the model box width and height is ensured from the following fields.

- a. Consideration of model boundary effects. Many scholars have systematically investigated the impact of model width on the slope seismic response (Tang et al., 2017). When the height is 0.6 m, a 1-m width is appropriate. When the width is larger than 2 m, the error will be reduced to almost 0 compared with the prototype. Accounting for previous studies (Lin & Wang, 2006; Shi et al.,

Table 5.2 Reference slope shaking table model rigid box dimensions

No	Appearance size	References
1	3.1 × 1.0 × 0.7 m	Shi et al. (2015)
2	4.4 × 1.3 × 1.2 m	Lin and Wang (2006), Wang and Lin (2011)
3	1.7 × 1.28 × 2.5 m	Fan et al. (2016)
4	2.05 × 0.6 × 1.4 m	Shinoda et al. (2015)
5	3 × 0.4 × 0.6 m	Zhao et al. (2015)
6	5 × 2.2 × 1.2 m	Yuan et al. (2014)
7	3.7 × 2.78 × 2.1 m	Liu et al. (2014)
8	3.7 × 2.78 × 2.45 m	Liu et al. (2013)
9	3.7 × 1.7 × 1.2 m	Huang et al. (2013)
10	3.5 × 1.6 × 1.8 m	Yang et al. (2012)

Table 5.3 Engineering parameters of slope shaking table test model box

Parameters	Values
Physical dimensions	3.5 × 1.5 × 1.6 m
Bottom bolt inner size	3.5 × 1.5 m
Internal dimensions	3.4 × 1.0 × 1.6 m
Model box weight	1.35 T
Design slope earthwork	2.5 m ³
Model box material	High-strength steel, tempered glass

2015; Wang & Lin, 2011), the reasonable internal net width is determined to be 1 m for the balance of little accuracy loss and model expense reduction.

- b. Combination of sample preparation difficulty, shaker bearing capacity, and internal volume control. We set the internal net height of the model box to 1.6 m and the maximum height of the slope materials to 1.5 m. The model parameters concluded in this chapter in Table 5.3 are in accordance with the rigorous experimental review that conducted by other authors in Table 5.2.

(2) Assembly of the model box

The slope model box framework was welded using 20 #b channel steel, 10 #b channel steel, 10 # I-steel, and 10 # equilateral angle steel, according to the Chinese code Hot Rolled Section Steel The front and back profiles are made of 10-mm-thick tempered glass to monitor slope deformation using high-speed cameras. The channel steel at the bottom has 10 bolt holes at specific coordinates, which can be connected and fixed with the shaking table. To reduce the relative slip between the slope model and bottom during vibration, the steel bottom plate should be handled as a rough surface. The complete appearance of the assembled model box is shown in Fig. 5.1.

(3) Model box frequency test

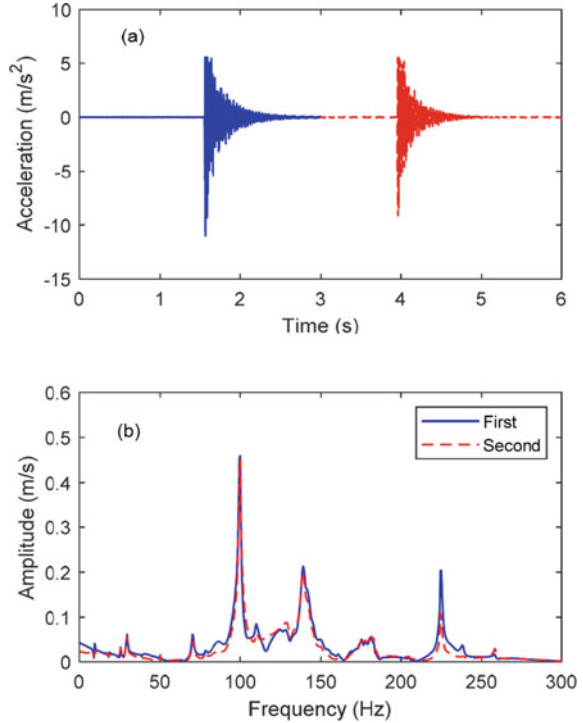
Fig. 5.1 Rigid model box

When the inherent frequency of a structure coincides with the compulsive vibration frequency, the input energy of the vibration tends to be transferred to the mechanical objective. Mechanical resonance poses a problem in geotechnical engineering practice, particularly when the structure objectives have a relatively low inherent frequency, which is likely to meet the vibration frequency, and the large amount of energy restored in the vibration is presented as a notable amplitude that may destroy the entire structure objectives. The inherent frequency of the model box is therefore not permitted in the seismic input frequency domain; Otherwise, the resonance of the rigid box will not only destroy the structure, but also distort the output acceleration when the input is close to the inherent frequency.

The inherent frequency of a rigid box is generally much higher than that of soil. The upper critical seismic frequency applied by the shaker is approximately 50 Hz, which increases the difficulty when using inadequate seismic frequencies to test its inherent frequency. The actual seismic frequency must be confirmed to be lower than that of the model box before the formal experimental excitations to avoid energy dissipation caused by the environment. The inherent frequency is therefore measured in the pretest by manually knocking with a hammer, and the initial frequency of this free vibration can be beyond that for the resonance.

The high-frequency signal is first created by rigid hammer knocking. Notably, the initial frequency must be sufficiently high and the hammer must be stiff with a good elastic modulus. The hammer knockings excite the box twice continuously along the length direction. One or more sensors are placed on the bottom and side wall of the box to record the acceleration data during this process. A group of time and frequency domain curves of the acceleration and amplitude signal are shown in Fig. 5.2. The frequency of the first two orders of the frequency-domain signal of the two excitations are 100 and 139 Hz, respectively. This indicates that its inherent frequency is larger than that of the upper limit of the proposed input seismic excitation frequency during the experiment, which means that the resonance has been eliminated.

Fig. 5.2 Frequency test results of the shaking table rigid box in the time and frequency domains (reprinted from Zhao et al. (2020) with permission of Elsevier)



5.1.2 Material Production of Slope Model

The testing materials commonly adopted in physical models include field samples and manual materials in a controlled proportion. To investigate the slope seismic response under different ground motion sequences, the model is expected to be non-destructive and maintain dynamic performance throughout the test. The model should therefore have a sufficient stiffness and resistance to multiple seismic sequences. Materials such as clays and silty sands are thus inappropriate owing to the destruction risk. The simulated prototype materials with an elastic modulus 4 GPa and Poisson’s ratio of 0.3 are shown in the yellow area in Fig. 5.3.

The similarity theorem includes the theory and principles to bridge the gap between the slope response in nature and similar phenomena for research purposes conducted at a particular scale. This generally includes geometric similarity, dynamic similarity, similar boundary conditions, similar motion characteristics, similar materials, and similar media. In this shaking table test, the requirements for the test layout are as follows: base test conditions, model plane size (i.e., similarity ratio), shaker bearing capacity, permissible model box height, equivalent prototype mass, asperity requirement for seismic inputs, horizontal eccentricity ratio in the vibration, the FOS for the vibration during fatigue, and emergency management planning. Test prototypes are therefore often scaled in the model test using similarity theory.

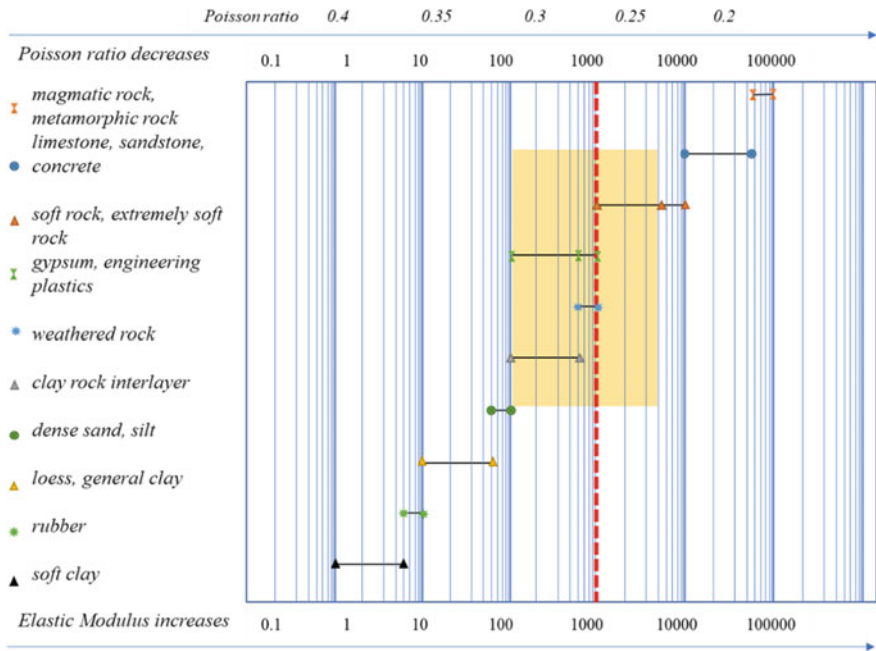


Fig. 5.3 Variance on the elastic modulus and Poisson’s ratio of slope materials (modified from Engineering Geology Manual (2007))

(1) **Material preparation**

Slope prototypes are generally a mixture of hard rock to soft clay; it is therefore challenging to unify the properties of the model materials. Table 5.4 summarizes the current design materials, and three kinds of test materials were selected. These include the on-site soil sample, the single material (e.g., a single clay), and proportioning

Table 5.4 Classification of shaking table slope model material based on previous studies

Materials	Sources	Representative thesis
On-site sample	On-site soils	Wang et al. (2010), Yang et al. (2015)
Single material	Dry sand, clay dam gravel filling, clay slope, earth-rock dam, reinforced retaining wall filling	Huang et al. (2011), Lin and Wang (2006), Liu et al. (2016), Ng et al. (2004), Wang and Lin (2011)
Proportioned material	Cement, gypsum binder, quartz sand, barite aggregate, various rocks, collapses, iron powder, bentonite	Aydan and Kumsar (2009), Fan et al. (2016), Huang et al. (2013), Jiao et al. (2014), Li et al. (2012), Liu et al. (2013, 2014), Shinoda et al. (2015), Xu et al. (2010), Yang et al. (2015, 2012)

Table 5.5 Well-proportioned model rock material in the model test

Material	Quartz sand	Barite powder	Gypsum powder	Glycerin	Water
Proportion (%)	46.5	27.5	20.0	1.3	4.7

material (e.g., barite, quartz sand, and gypsum). The thick mixture should meet the mechanical and physical characteristics of soft rock and hard rock by adjusting the concentration of the single material proportion (Liu et al., 2014). The static and dynamic characteristics of the artificial material must be quantified by a group of direct shear tests or static triaxial tests and dynamic triaxial tests.

When three parameters (sand binder ratio, water paste ratio, and barite content) are controlled in the test, the material density and stiffness should be controllable (Shi et al., 2015). Owing to the availability and adjustability of this proportioning method, a similar material selection scheme is adopted during testing. Here, we use five kinds of engineering materials—barite, quartz sand, gypsum, glycerin, and water—in accordance with the target proportion for good performance, according to details provided in the literature (Aydan & Kumsar, 2009; Fan et al., 2016; Huang et al., 2013; Jiao et al., 2014; Li et al., 2012; Liu et al., 2013, 2014; Shinoda et al., 2015; Xu et al., 2010; Yang et al., 2012, 2015). The specific proportion information is listed in Table 5.5. Of note, the quartz sand is relatively uniform; the particle size is mainly concentrated between 0.5 and 1 mm with an average of 0.68 mm.

(2) Determination of similarity ratio and material proportion

On the basis of dimensional analysis, the Buckingham π theorem is used to determine the dynamic similarity ratio of the shaking table test (Buckingham, 1914). According to the Buckingham π theorem, if a relation equation $f(q_1, q_2, q_3 \dots q_n) = 0$ has n physical quantities and k independent basic dimensions, it should be converted into a relational formula $F(\pi_1, \pi_2, \pi_3 \dots \pi_{n-k}) = 0$ that contains $(n-k)$ dimensionless π term relations. Without knowing the relationship between formula f and F , if provided the k basic physical dimensions as $A_1, A_2, A_3 \dots A_k$, the remaining $(n-k)$ physical dimensions can be expressed as the power of the k basic dimensions as follows:

$$q_{k+1} = f_{k+1}(q_1, q_2, q_3 \dots q_k) = A_1^{p_1} A_2^{p_2} A_3^{p_3} \dots A_k^{p_k} \tag{5.1}$$

$$q_n = f_n(q_1, q_2, q_3 \dots q_k) = A_1^{r_1} A_2^{r_2} A_3^{r_3} \dots A_k^{r_k} \tag{5.2}$$

If k basic physical quantities are simultaneously multiplied by a conversion factor sequence $C_1, C_2, C_3 \dots C_k$, then k for any integer can be vectorized into Eq. (5.3). The remaining $(n-k)$ physical quantities in Eqs. (5.1) and (5.2) are expressed as Eq. (5.4) and Eq. (5.5), respectively:

$$q'_k = C_k q_k \tag{5.3}$$

$$q'_{k+1} = C_1^{p_1} C_2^{p_2} \dots C_k^{p_k} q_{k+1} \tag{5.4}$$

$$q'_n = C_1^{r_1} C_2^{r_2} \dots C_k^{r_k} q_n \tag{5.5}$$

Equations (5.6) and (5.7) are inferred when the above physical quantities are substituted into the original equations.

$$f(C_1 q_1, C_2 q_2 \dots C_k q_k, C_k^{p_1} q_{k+1} \dots C_1^{r_1} C_2^{r_2} \dots C_k^{r_k} q_n) = 0 \tag{5.6}$$

$$f\left(1, 1 \dots 1, \frac{q_{k+1}}{q_1^{p_1} q_2^{p_2} \dots q_k^{p_k}} \dots \frac{q_n}{q_1^{r_1} q_2^{r_2} \dots q_k^{r_k}}\right) = 0 \tag{5.7}$$

Equation (5.7) is transformed as follows:

$$\frac{q_{k+1}}{q_1^{p_1} q_2^{p_2} \dots q_k^{p_k}} = \pi_1 \tag{5.8}$$

$$\frac{q_n}{q_1^{r_1} q_2^{r_2} \dots q_k^{r_k}} = \pi_{n-k} \tag{5.9}$$

The Buckingham π theorem effectively determines the scale relationship and similarity ratio of the slope shaking table model. It also verifies that the $(n-k)$ physical quantities can be obtained from k basic quantities through a certain conversion factor sequence. The functional relationship of the main physical quantities is listed in Eq. (5.10). The physical quantities are shown in Eq. (5.10) and their symbols and dimensions are listed in Table 5.6.

$$f(\rho, l, E, \mu, c, \varphi, \sigma, \varepsilon, t, f, u, v, a, g, \zeta) = 0 \tag{5.10}$$

In accordance with the dimension analysis method, it is necessary to consider the principle of strain similarity, in which the elastic modulus is similar to the control

Table 5.6 Dynamic similarity ratio of key physical dimension derivation

Physical quantity	Symbol	Dimension	Physical quantity	Symbol	Dimension
Density	ρ	ML^{-3}	Time	t	T
Geometric size	l	L	Frequency	f	T^{-1}
Elastic Modulus	E	$ML^{-1}T^2$	Displacement	u	L
Poisson's ratio	μ	1	Velocity	v	LT^{-1}
Cohesion	C	$ML^{-1}T^2$	Acceleration	a	LT^{-2}
Internal friction angle	φ	1	Gravity acceleration	g	LT^{-2}
Stress	σ	$ML^{-1}T^2$	Damping ratio	ζ	1
Strain	ε	1			

strain under dynamic deformation conditions between the physical model and the prototype. We must therefore verify three control parameters when considering the similarity ratio of the test. We first need a model that is reduced in size to maintain control of the length ratio of the original studied field and modal allowable size. The material density is then difficult to satisfy as the same ratio carried out with size; thus, we should use materials that are the same as the original rocks with similar characteristics. The dynamic response under seismic excitation conditions is the first-order purpose to conduct the experiment and the high-quality data input and acquisition are extremely significant. We thus adjust the acceleration spectrum away from distortion and set the similarity value to 1. To summarize the work for simplification of the similarity model calculations under the premise of the Buckingham π theorem, we make the density similarity $C_\rho = 1$ and the elastic modulus $C_E = \lambda$, which is internally achieved in the 1 g condition. The conversions of the similar constants determined in this experiment are listed in Table 5.7. Of note, the similarity criterion is only one kind of scheme that satisfies the Buckingham π theorem, and is often used owing to its maturity and simplification.

Random excitation is used in the test and the designed slope model does not show notable damage when the ground motion magnitude remains small. The slope

Table 5.7 Similarity ratio affirmation of the test physical dimensions with the Buckingham π theorem

Category	Physical quantity	Value	Abbreviation
Geometric size	Length (Control)	λ	C_L
	Area	λ^2	C_s
	Volume	λ^3	C_v
Material characteristics	Density (Control)	$C_\rho = 1$	C_ρ
	Mass	$C_\rho C_L^3 = \lambda^3$	C_m
	Cohesion	$C_\rho C_L = \lambda$	C_c
	Internal friction angle	1	C_φ
	Poisson's ratio	1	C_μ
	Modulus	$C_\rho C_L = \lambda$	C_E
	Stress	$C_\rho C_L = \lambda$	C_σ
	Strain	$C_\sigma C_E^{-1} = 1$	C_ε
Dynamic characteristics	Acceleration (Control)	$C_a = 1$	C_a
	Force	$C_\rho C_L^3 C_a = \lambda^3$	C_F
	Velocity	$C_L C_t^{-1} = \lambda^{-0.5}$	C_v
	Displacement	$C_\varepsilon C_L = \lambda$	C_d
	Time	$[C_L C_a^{-1}]^{0.5} = \lambda^{0.5}$	C_t
	Frequency	$[C_a C_L^{-1}]^{0.5} = \lambda^{-0.5}$	C_f
	Damping ratio	1	C_ζ

Table 5.8 Comparison between slope prototype and model parameters

Design specification (unit)	Prototype parameters	Model parameters
Slope height (m)	28.75	1.15
Density (kg/m ³)	2000	2000
Gravity acceleration (m/S ³)	9.8	9.8
Elastic modulus (MPa)	4000	160
Poisson ratio	0.33	0.33
Cohesion kPa	1500	60
Internal friction angle (°)	35	35
Time (s)	30	6
Damping ratio	0.05	0.05

model should thus have mechanical parameters similar to the prototype, such as high rigidity. The rock slope height corresponding to its design is generally within 30 m, according to the Technical Code for Building Slope Engineering (2013). The generalized prototype slope of this model is therefore a rock slope with interbedded soft and hard rock. The slope model parameters are displayed in Table 5.8.

The unconfined compressive strength of the model material is 800 kPa, the similarity ratio is 25, and the uniaxial compressive strength of prototype material is $R_c = 20$ MPa. On the basis of the empirical mechanical relationships on soft rocks (Palchik, 2010), the ratio of the elastic modulus to uniaxial compressive strength is $M_c = 200 - 250$. We set $M_c = 200$ for the calculation and model material design. The Young's modulus of the prototype is 4 GPa and the Poisson's ratio is 0.33, whereas the Young's modulus of the model is 160 MPa. The other significant relationships between the different indicators of the model and prototype materials are listed in Table 5.8. The cohesion and internal friction angle of the materials were obtained through a series of basic unit tests, including direct shear tests.

5.1.3 Construction and Measurement of Slope Model

This section introduces the test model preparation, including the model construction and sensor layout design.

(1) Construction of material embedded with sensors

In the beginning of the model construction, foam boards are placed on the bottom of both sides of the model, as shown in Fig. 5.1. According to the proportions listed in Table 5.5, 87.8 kg of barite powder, 63.8 kg of gypsum powder, and 148.4 kg of quartz sand for a total of 300 kg were mixed in a large mixer to ensure that all the materials were uniformly mixed for the convenience of the subsequent steps. It is

noted that the quartz sand should be added last to prevent uneven mixing in the dry mixing process because the particle size is relatively large. The mixer direction is changed several times to fully mix the three components, which takes approximately 8–10 min.

Glycerin solution is prepared in advance according to the proportion of glycerin and water in Table 5.5. Next, 14.1 kg of dry material and 900 g of solution are slowly combined during the stirring process in a small mixer.

The model is constructed from bottom to top in the model box. Each 5-cm-thick soil is regarded as a layer and the loose soil is consolidated into a denser layer after spreading the first layer. In the same way, the bottom is constructed to include 5 layers, with a total height of 30 cm.

The chromatic aberration of the tempered glass surface should be sufficiently discrepant to allow clear observations. A certain proportion of black sand (e.g., 30%) is therefore added in a 1–2 cm layer thickness close to the edge of the side wall to increase the chromatic aberration and facilitate high-speed imaging. Figure 5.4a shows an image after stirring the dyed sand, and Fig. 5.4b shows an image of the 10×10 cm grid lines. All images are processed using software in the displacement field for supportive analysis.

The prepared model must be conserved for 5–7 days owing to the presence of gypsum. The model is hoisted and fixed onto the vibrating table after maintenance, various sensor collection channels are installed, and high-speed photogrammetry equipment is erected.

(2) Layout of the dynamic response measurement

The sensors are sensitive, stable, and have a high accuracy in service under static and dynamic measurement conditions. Even if the input signals change little over time, the relation is apparent between the input and output data of the slope, which reflects the sensitivity characteristics. The requirement of real-time and accurate

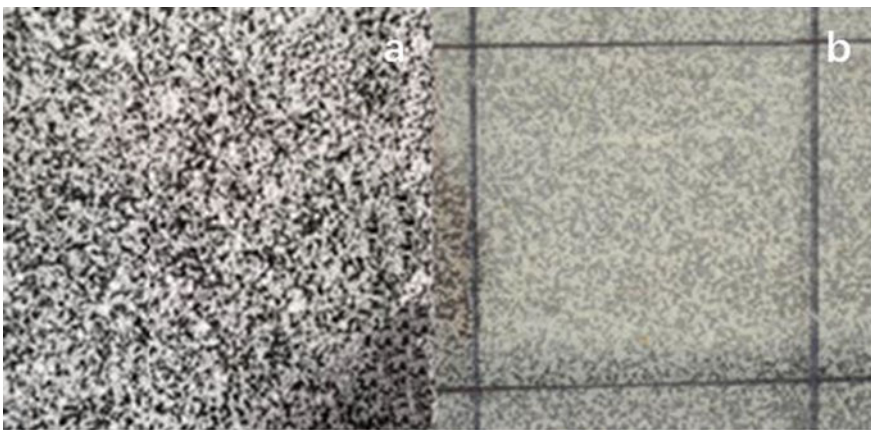


Fig. 5.4 Model side dyed sand treatment **a** and view of grid line **b**

Table 5.9 Test sensors in the shaking table model

	Sensor types	Test sampling frequency	Quantity
Contact measurement	Acceleration sensor	256 Hz	45
	Pull-wire displacement meter	256 Hz	8
Non-contact measurement	High-speed photography equipment	1000 frames/s	1
	3D laser scanner	/	1

measurements is emphasized in the dynamic signal recording of the slope. To obtain high-quality measurements, contact and non-contact measurement approaches are planned in the grid. The sensor information is listed in Table 5.9.

The main parameters are shown in Table 5.10, and the principles of the sensors are as follows. The determination of the range of acceleration sensors is based on a preliminary numerical calculation. The results indicate that the maximum acceleration amplification factor of the slope top, which is the most dangerous part of the model, should be within 5 under seismic stimulation. It is therefore evident that under the maximum seismic input of 0.8 g, the acceleration sensors with a 5 g range have an adequate capacity for real-time measurements without over-ranged accidents. The acceleration sensors used in this test include 25 acceleration sensors (JF106T, Yangzhou Jufeng Technology Co., Ltd.) and 20 piezoelectric acceleration sensors (DH105E, Donghua). The principle of these acceleration sensors is that an HY-ZK-1 impedance converter can be used to convert the charge signal into a voltage signal. The key parameters are listed in Table 5.10.

On the basis of the analogy with particle image velocimetry technology, several high-speed cameras are installed to take photographs of the dynamic objects to collect a sequence of digital images. These 3D information solutions to the target and analytical algorithms are combined to measure the structural or motion parameters. The 3D coordinate information of the high-speed moving target is obtained using a continuous picture sequence taken with the high-speed camera. The seismic spatial response information of the target objective is available after analysis, which directly reflects the static, kinetic, and dynamic characteristics of the slope.

The advantages of high-speed camera measurement technology are generalized as follows. First, dynamic measurements can record the spatial positions and state of objects at any instant. Dynamic information of every moving step can be continuously recorded with intensive sampling, which provides the monitoring system with favorable dynamic characteristics. Second, non-contact measurements can achieve the measurement purpose with as few changes to physical properties of materials as possible, which makes the measurements more reliable and closer to reality. Third, multi-point acceleration measurements allow simultaneous data acquisition from multiple monitoring points and collateral analysis on multiple regions. The development of high-speed camera measurement technology, auxiliary devices, and algorithms has reached an accuracy of 10^{-2} pixels, which ensures accurate analysis.

Table 5.10 Detailed parameters of the multi-type sensors (JF106T, DH105E)

Sensor type	Item	Sampling interval
JF106T acceleration sensor	Frequency range	0.2~1000 Hz
	Temperature range	-40~150 °C
	Charge sensitivity	1200 PC/g
	Range	±10 g
	Maximum impact	100 g
	Transverse sensitivity	<5%
	IRF	8 kHz
	Capacitance	6000 pF
	Insulation resistance	>109 Ω
	Sensitive original	PZT-5
	Weight	118 g
	DH105E acceleration sensor	Frequency range
Temperature range		-20~80 °C
Charge sensitivity		1000 MV/ms ⁻²
Range		±5 g
Maximum impact		50 g
Transverse sensitivity		<5%
Internal structure		Shear
Weight		165 g

Note IRF refers to the installation resonance frequency. Detailed information on the displacement sensors is not provided here

The high-speed camera used in this test is an I-SPEED 7 high-performance camera with a peak of 500,000 fps. Figure 5.5 shows an image of the camera, light source, and a lighting effect diagram during excitation with a shuttering time of 0.1 μs. The parameters of the high-speed camera are listed in Table 5.11. Sunlight with diffuse reflection makes it possible to obtain a picture with a frame rate within 250 fps. However, darker pictures tend to increase the frame rate. Following the provided instruction, the image is quite distinguishable when the frame rate is below 1000

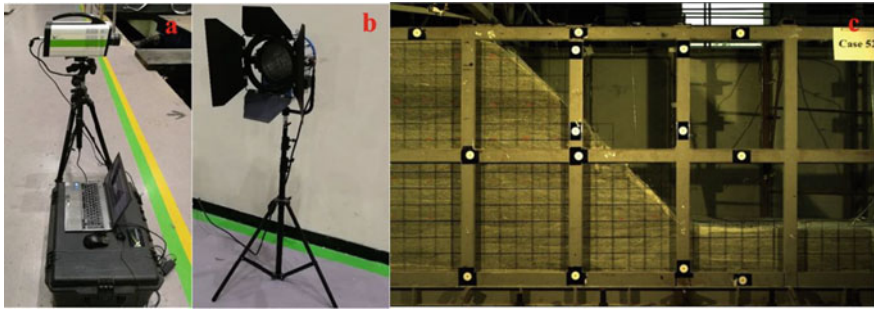


Fig. 5.5 High-speed camera **a**, light source **b**, and lighting effect diagram during excitation with the shuttering time of $0.1 \mu\text{s}$ **c**

Table 5.11 Detailed parameters of the I-SPEED 7 series high-speed cameras

I-SPEED 7	Sampling interval
Upper limit of frame rate	500,000 fps
Resolution	2048×1536 ppi
Shutter type	Global exposure
Shutter time	$1 \mu\text{s}$ Standard mode, 250 ns fast mode
Built-in SSD	500 GB
Recording time	1000 fps 16.1 s; 500 fps 32.2 s
Operating temperature	$0\text{--}40 \text{ }^\circ\text{C}$

fps in the direct sunlight at approximately 50,000 lx, whereas the frame rate of pictures beyond that critical frame rate is not adequate for data processing. Hence, a professional light source is required in the test, with two high-speed camera-specific light sources, as shown in Fig. 5.5. To recede the local light spots caused by the direct irradiation on the model box, the two light sources are placed on both sides of the model box along oblique axes. Each single light source has a power of 3520 W and nominal voltage of 220 V.

To obtain pictures with high resolution and sufficient light in combination with the upper limit of the forced vibration of the shaker at 50 Hz, 500 fps is chosen to ensure the picture quality and dataset density. The test is recorded in trigger mode, the maximum length of each recording is 32 s, and the longest earthquake duration is 20 s. Each seismic wave is stored for 20 s, with 10,000 pictures collected each time. These pictures are stored in real-time in .jpg or .jpeg format in a hard drive, saving approximately 13 GB of pictures each time.

The high-speed cameras are placed on both sides of the model box, and the 3D laser scanner is set on the front of the model. A total of 45 sensors (A0–A44) are installed in the experiment, the layout of which is shown in Fig. 5.6. The acceleration sensors A16, A26, A36, and A42 were damaged owing to the vibration impact on the material, thus 41 acceleration sensors were in service for further seismic measurements.

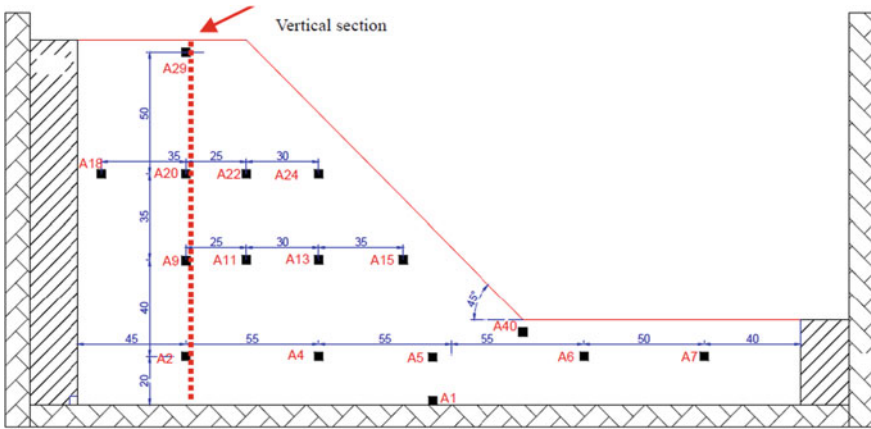


Fig. 5.6 Stochastic response acceleration sensor observation profile

5.1.4 Ground Motion Generation and Response Acquisition

(1) Ground motion generation

The number of artificial excitation samples must be sufficiently large to analyze after the test and sufficiently small to operate during the test. In accordance with previous research (Liu et al., 2016), it is believed that the dynamic analysis requires 144 ground motion samples, for which the cutoff error is less than 5% and the average response spectrum fits well with the standard spectrum. The response spectrum represents the curve of the ultimate seismic spatial responses of a single point system with the inherent vibration period of the particles under deterministic seismic excitation. The definition of the average response spectrum of the sample generated by the seismic ground motion model is described in Chap. 2. Using this method, 144 acceleration time history ground motion samples are used as the seismic inputs. Some parameters of the ground motion generation are listed in Table 5.12. To clarify the concepts of these parameters, the ground motion model parameters involved in Chap. 2 are rewritten as follows:

Table 5.12 Parameters of artificial seismic excitation time history in slope shaking table test

Parameters	Values	Parameters	Values
a	6	T	30 s
b	0.2	$\bar{\omega}_g$	15.71 rad/s
c	5.5	$\bar{\xi}_g$	0.72
d	2	\bar{a}_{\max}	196.2 cm/s ²
n	2	\bar{r}	2.83

$$A(t) = \left[\frac{t}{c} \exp\left(1 - \frac{t}{c}\right) \right]^d \quad (5.11)$$

$$S_0(t) = 2 \frac{\bar{a}_{max}^2}{\bar{r}^2 \pi \omega_g(t) \left(2\xi_g(t) + \frac{1}{2\xi_g(t)} \right)} \quad (5.12)$$

$$\omega_g(t) = \omega_0 - a \left(\frac{t}{T} \right)^n; \xi_g(t) = \xi_0 + b \left(\frac{t}{T} \right)^n; \omega_f(t) = 0.1\omega_g(t) \quad (5.13)$$

$$\omega_0 = \bar{\omega}_g + \frac{a}{2}; \xi_0 = \bar{\xi}_g - \frac{b}{2} \quad (5.14)$$

where T is the ground motion duration, n is the function shape control variable, which is equal to 1 to represent the linear time-variation $\bar{\omega}_g$, $\bar{\xi}_g$, c , and d are determined based on the regional on-site categories, \bar{a}_{max} is the average of ground motion peak acceleration, and \bar{r} represents the equivalent crest factor of smooth ground motion.

The 144 pieces of the ground motion samples in this batch are generated according to the Class II site parameters in the specifications. There exists a factor of five differences in the time history and frequency spectra between the prototype and slope model based on the similarity laws. The time for real seismic waveform mainly fluctuates between 5 and 25 s. We thus take 30 s for the spectrum analysis. As expected, the low-amplitude components contribute the most in this time domain, and the similarity laws are also realistic in terms of the difference of horizontal axis of the frequency spectra.

In the following section, a total of 151 artificial seismic samples are generated to acquire the seismic response of the different regions of the slope to study the amplification and de-amplifying effects. The ground motion time history stimulations include seven white noise samples with a prefix name of W_n , and 144 artificial ground motion samples with a prefix name of R_d .

(2) Seismic response acquisition

The excitation scheme with 144 slope seismic samples is listed in Table 5.13. The slope dynamic response characteristics are recorded in real-time to accordingly study the seismic response of the slope under the excitation of each seismic sample.

5.2 Seismic Response Analysis of Slope Model

A large amount of data is captured in the file format, as described in Sect. 5.1, and each seismic response result corresponds with one piece of a seismic sample. This section focuses on the analysis and processing of the seismic characteristics of the slope model under these conditions. An approach is adopted to illustrate the

Table 5.13 Scheme for ground motion time history spectrum of the slope

No	Wave file name	No	Wave file name	No	Wave file name	No	Wave file name
1	Wn 1	39	Rd 37	77	Rd 74	115	Rd 110
2	Rd 1	40	Rd 38	78	Rd 75	116	Rd 111
3	Rd 2	41	Rd 39	79	Wn 4	117	Rd 112
4	Rd 3	42	Rd 40	80	Rd 76	118	Rd 113
5	Rd 4	43	Rd 41	81	Rd 77	119	Rd 114
6	Rd 5	44	Rd 42	82	Rd 78	120	Rd 115
7	Rd 6	45	Rd 43	83	Rd 79	121	Rd 116
8	Rd 7	46	Rd 44	84	Rd 80	122	Rd 117
9	Rd 8	47	Rd 45	85	Rd 81	123	Rd 118
10	Rd 9	48	Rd 46	86	Rd 82	124	Rd 119
11	Rd 10	49	Rd 47	87	Rd 83	125	Rd 120
12	Rd 11	50	Rd 48	88	Rd 84	126	Rd 121
13	Rd 12	51	Rd 49	89	Rd 85	127	Rd 122
14	Rd 13	52	Rd 50	90	Rd 86	128	Rd 123
15	Rd 14	53	Wn 3	91	Rd 87	129	Rd 124
16	Rd 15	54	Rd 51	92	Rd 88	130	Rd 125
17	Rd 16	55	Rd 52	93	Rd 89	131	Wn 6
18	Rd 17	56	Rd 53	94	Rd 90	132	Rd 126
19	Rd 18	57	Rd 54	95	Rd 91	133	Rd 127
20	Rd 19	58	Rd 55	96	Rd 92	134	Rd 128
21	Rd 20	59	Rd 56	97	Rd 93	135	Rd 129
22	Rd 21	60	Rd 57	98	Rd 94	136	Rd 130
23	Rd 22	61	Rd 58	99	Rd 95	137	Rd 131
24	Rd 23	62	Rd 59	100	Rd 96	138	Rd 132
25	Rd 24	63	Rd 60	101	Rd 97	139	Rd 133
26	Rd 25	64	Rd 61	102	Rd 98	140	Rd 134
27	Wn 2	65	Rd 62	103	Rd 99	141	Rd 135
28	Rd 26	66	Rd 63	104	Rd 100	142	Rd 136
29	Rd 27	67	Rd 64	105	Wn 5	143	Rd 137
30	Rd 28	68	Rd 65	106	Rd 101	144	Rd 138
31	Rd 29	69	Rd 66	107	Rd 102	145	Rd 139
32	Rd 30	70	Rd 67	108	Rd 103	146	Rd 140
33	Rd 31	71	Rd 68	109	Rd 104	147	Rd 141
34	Rd 32	72	Rd 69	110	Rd 105	148	Rd 142

(continued)

Table 5.13 (continued)

No	Wave file name	No	Wave file name	No	Wave file name	No	Wave file name
35	Rd 33	73	Rd 70	111	Rd 106	149	Rd 143
36	Rd 34	74	Rd 71	112	Rd 107	150	Rd 144
37	Rd 35	75	Rd 72	113	Rd 108	151	Wn 7
38	Rd 36	76	Rd 73	114	Rd 109	152	/

Note Rd represents random seismic excitations; Wn represents white noise samples

stochastic characteristics and variability of the indicators to investigate their seismic behavior considering the slope dynamic response with variable ground motion.

5.2.1 Dynamic Characteristics of the Slope Model

(1) White noise test

To estimate slope dynamic characteristics, the tests must be nondestructive and the model must be completed in the pretest before the seismic samples are officially applied. The white noise tests are performed for that purpose in the verification. Slope gridlines on the plexiglass box are shown in Fig. 5.7. In this pretest, an artificial white noise excitation is used to estimate the slope completeness. Figure 5.8 shows the temporal curves and frequency spectra of the white noise sample. Because the maximum value of the frequency input of the vibration shaker is 50 Hz, the frequency range for the white noise generation is set to 0–50 Hz. The duration is 40.96 s and the lowest frequency of the ground motion is set to 0.024 Hz ($1/40.96 \text{ s} = 0.0224 \text{ Hz}$), which contributes to the fluctuation in the low-frequency range in Fig. 5.8.

$$S_A(w) = S_0 \quad (5.15)$$

The white noise inside the slope and white noise response spectra at different slope elevations are shown in Fig. 5.9. The same approach as that of the inherent

Fig. 5.7 Rock slope with gridlines on the plexiglass box



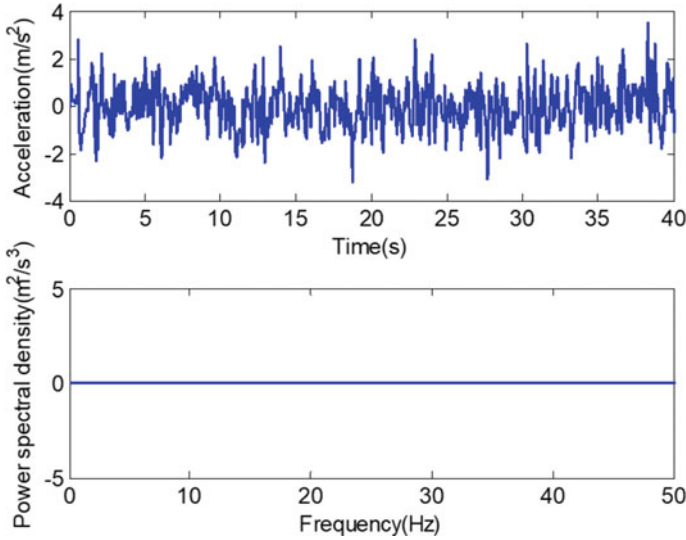


Fig. 5.8 White noise input temporal waveform and frequency power spectrum of the slope model

frequency measurement is adopted to investigate the frequency of the dynamic slope system consisting of the slope model and rigid box. The inherent frequency of the model is found to be approximately 34 Hz, thus the prototype inherent frequency is 6.8 Hz. The amplitude of the response remains different at multiple points inside the slope. The response amplitude generally increases with increasing slope elevation.

There are seven white noises in the validation before the official tests in each group, which contains 24 pieces of official seismic samples. Figure 5.10 shows the sequence in which the pretest that illustrates the slope model frequency spectrum hardly changes when treated with different pieces of white noise inputs, thus releasing a positive signal maintaining that the model keeps similar and complete before the official seismic excitation.

(2) Acceleration seismic responses

A deterministic investigation on the acquisition of the three dynamic response indicators is conducted, and the different elevation regions with their profile responses are selected prior to the statistical analysis in the following stochastic description, as shown in Fig. 5.6. The selection procedure is as follows.

Select the response of the one point monitored under four seismic excitations. This can be extracted from Fig. 5.11 in which the response obtained by multiple excitations differ at the same elevation, and the time domain peak value is 0.4–0.6 g. The data from the A9 acceleration sensor show that the frequency domain ranges under different seismic excitations are somewhat similar, whereas the energy records show a distinguishable difference.

Select the same seismic sample as the seismic input at a different elevation. It can be concluded from Fig. 5.12 that the waveshape changes only slightly at multiple

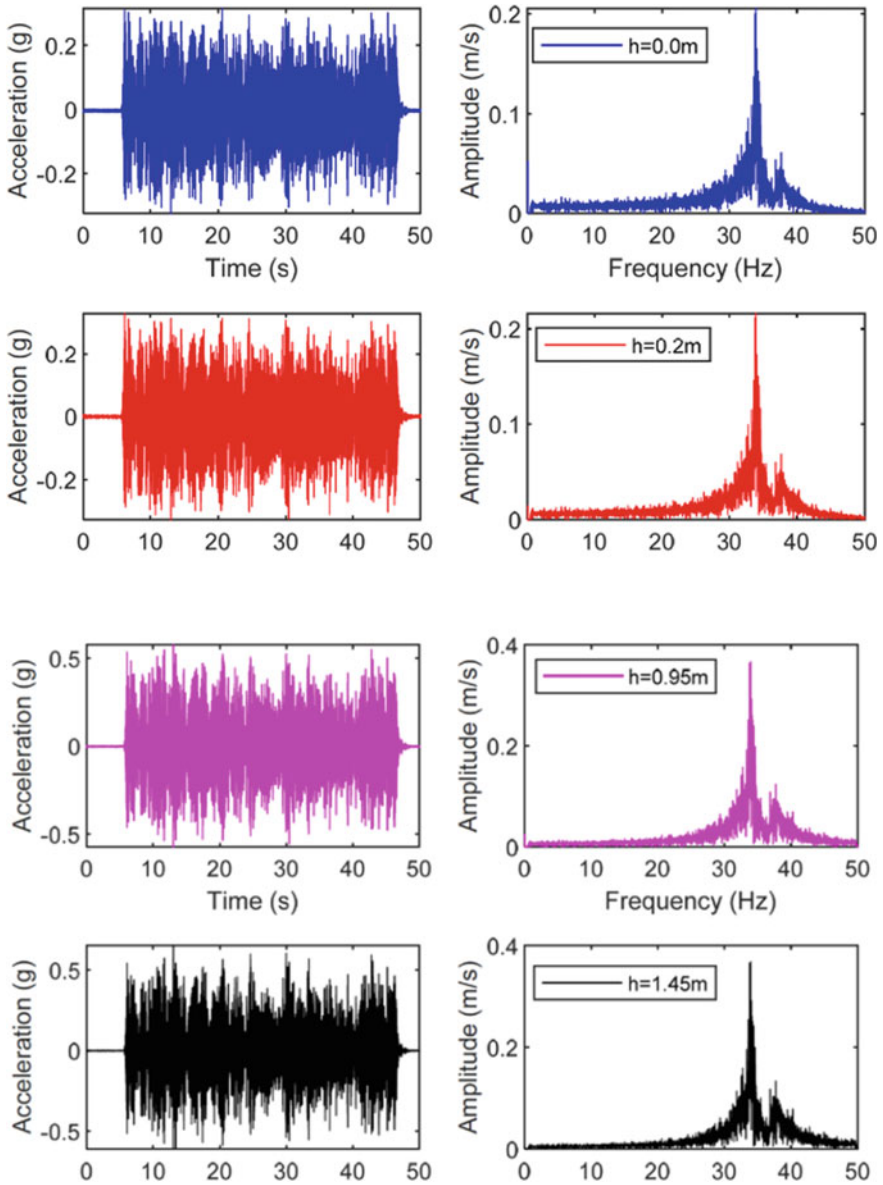


Fig. 5.9 White noise response spectra at different elevations of the slope model

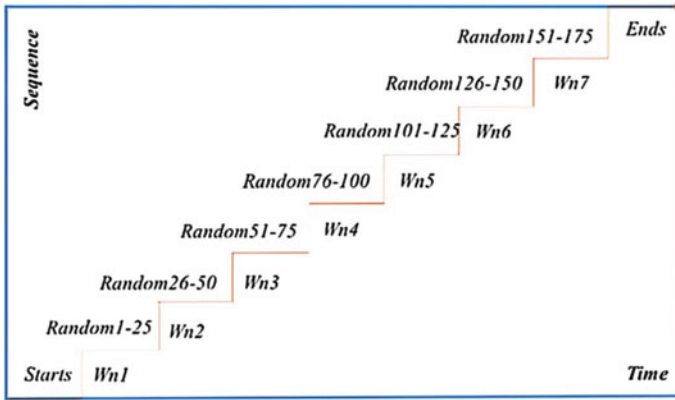


Fig. 5.10 Seismic sample excitation sequence

elevations of this sample, as demonstrated by the amplitude in each round. The intensity of the Fourier spectrum is also proportional to the frequency domain range and elevation.

Owing to the existence of non-stationary seismic excitation characteristics in the time and frequency domain, the acquisition of the slope dynamic response is difficult for obtaining accurate predictions on the seismic response. The data processing and analysis of these performance-based indicators are therefore necessary.

5.2.2 Stochastic Dynamic Response Analysis of Slope

(1) Probability density evolution (PDE) of acceleration response

There are 144 seismic excitation samples applied to acquire the continuous acceleration dataset. In the test, the dominating energy supplement of the acceleration starts at 5 s and ends at 25 s, as displayed in Fig. 5.13; however, the amplitude and frequency components vary with time. The distribution of the three typical elevations at the slope bottom A1, middle part of the slope A9, and slope top A29 are positioned at 1, 10, 20, and 29 s of the input sample to study the evolution principles of the probability density of acceleration under this ground motion section. Several respectable conclusions are implied in Fig. 5.14, as follows.

The acceleration PDF of the slope model at a given location at multiple moments follows a standard Gaussian distribution, and the distribution range gradually increases with increasing ground motion amplitude and ultimately returns to the initial calmness when the ground motion ends. For example, the distribution at $t = 1$ s almost coincides with that at $t = 29$ s.

The acceleration PDFs of multiple elevations remain symmetrical and follow normal Gaussian distributions with different standard deviations. The concentration

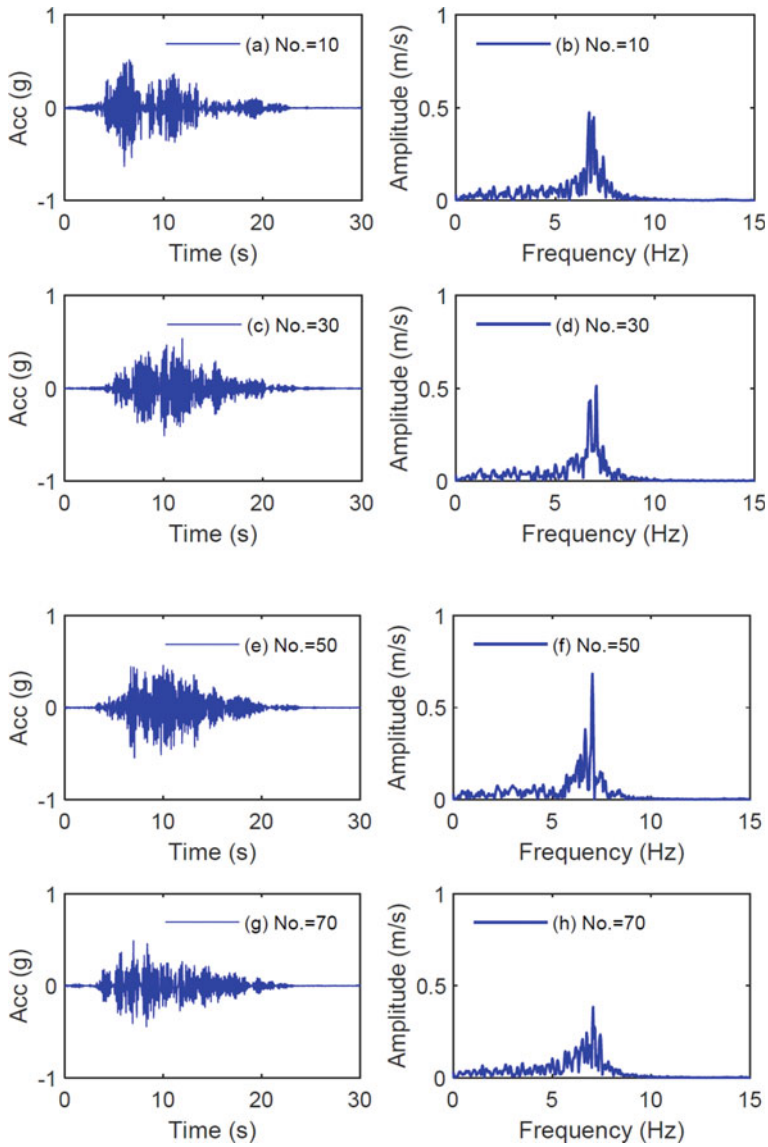


Fig. 5.11 Response and frequency spectra of the A9 sensor inside the slope under different seismic input conditions (No. means the number of ground motions)

degree of a series of curves increases with elevation, which is manifested as the amplifying effect. This phenomenon is particularly apparent for the horizontal acceleration and provides a general rule for the other 143 ground motion samples in the same time domain. We therefore conclude that the deterministic factors become dominant

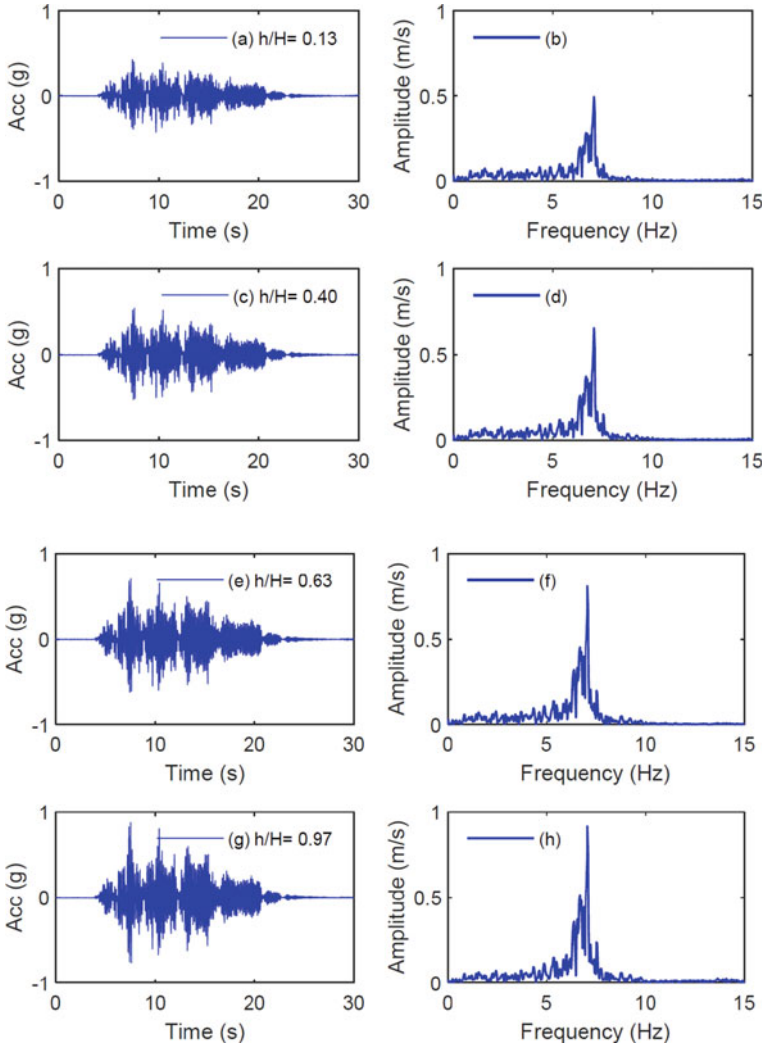


Fig. 5.12 Horizontal acceleration response along the elevation profile under one seismic excitation

with increasing time and elevation, and the features on the initial stochastic curve with large standard deviations are difficult to capture.

Figure 5.14 clearly shows that when the ground motion amplitude is insignificant (e.g., $t = 5$ or 20 s), the acceleration PDF follows a Gaussian distribution. However, when the peak value is large (e.g., $t = 10$ or 15 s), the distribution range of the function is broader and the value at sensor A29 at the slope top is even greater than 0.8 g. The distribution of the PDF of the acceleration changes and smoothness of the distribution function curve decreases.

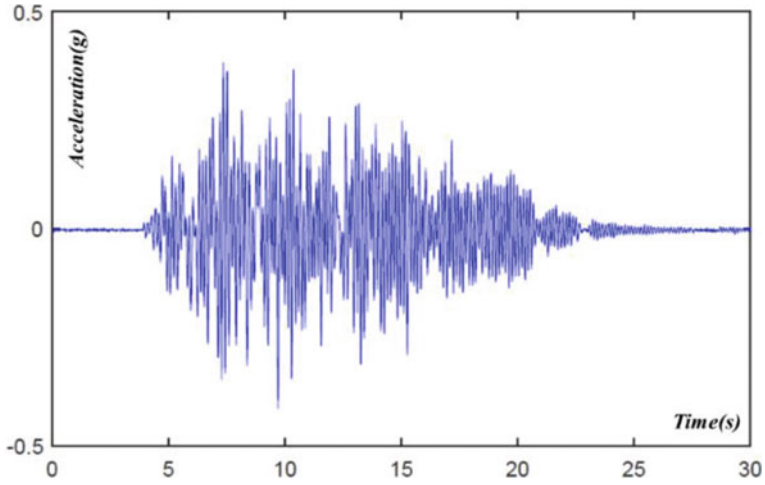


Fig. 5.13 Time history curve of the ground motion captured in the typical test

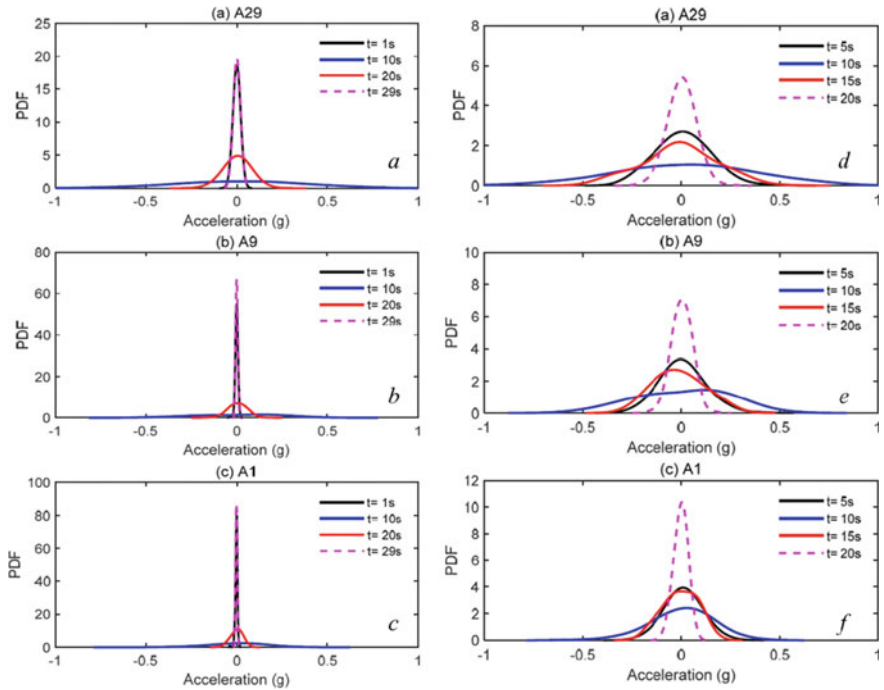


Fig. 5.14 PDFs of the acceleration at 1, 10, 20, and 29 s recorded on sensors A29 a, A9 b, and A1 at different elevations c. PDFs of the acceleration at 5, 10, 15, and 20 s recorded on sensors A29 d, A9 e, and A1 at different elevations f

The dynamic mean value may not be accurately 0. This is mainly caused by the nonlinear deformation of the slope under the high ground motion peak, material nonlinearity, and the random coupling of ground motion. However, owing to the large model stiffness, this part of the deformation is limited to an acceptable range, which has little effect on the study of the random dynamic response.

Figure 5.15 shows part of the acceleration response of the PDE surface under ground motion action measured at sensor A29. The PDF evolves in a normal distribution near the ground motion peak (10–12 s), and the occurrences at the other domain are small. The acceleration amplitude varies between -0.6 and 0.6 g at this time.

Figure 5.16 shows the PDE of the settlement at the slope top to the box edge, where numerous time-varying distributions appear at the peak seismic displacement, which is viewed as residual subsidence. This is caused by the variability of the ground motion samples and nonlinear material characteristics. The peak displacement in the model is within the critical range, so the displacement of the prototype is less than 10 mm according to the law of similarity. This should not cause landslide damage on the slope body within the simulated seismic conditions. Figure 5.17 also shows that the settlement is balanced in the positive and negative directions, which contributes

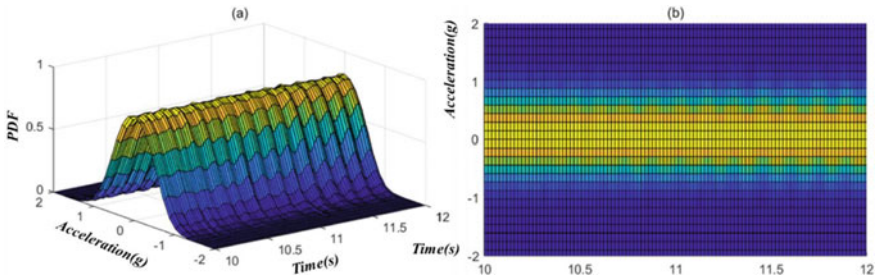
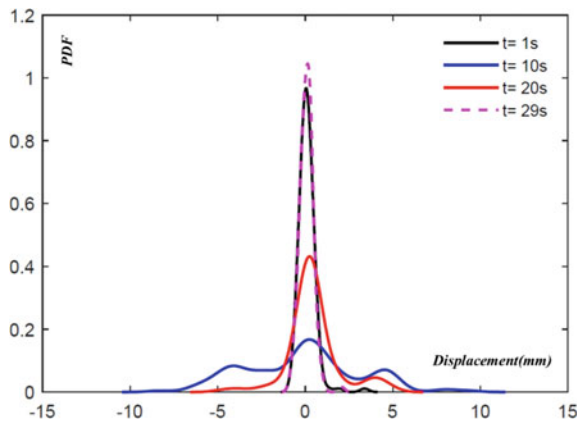


Fig. 5.15 Acceleration probability density evolution surface at sensor A29

Fig. 5.16 PDFs on the time-varying displacement at the slope top



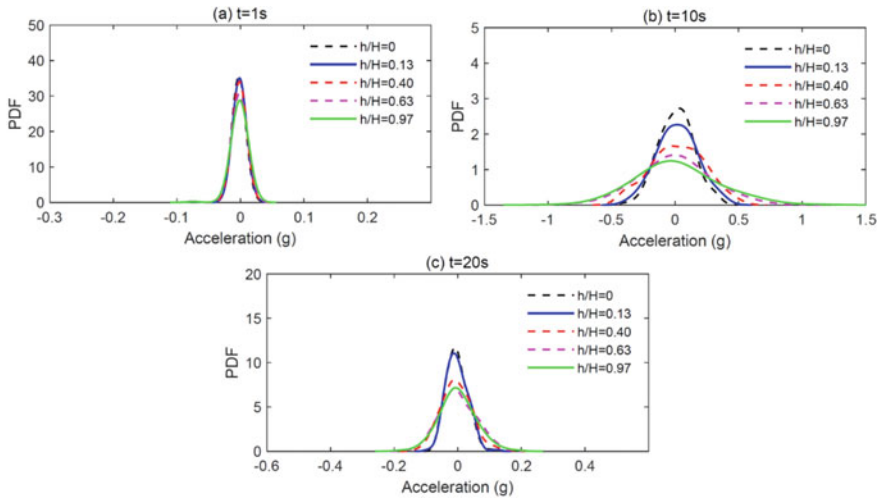


Fig. 5.17 PDFs of the vertical settlement at different elevations of the slope model when the time is 1s, 10s and 20s

to the aspect that the displacement is basically restored to the pre-seismic excitation level after the real earthquake.

(2) Elevation amplification effect on acceleration

a. Analysis of acceleration at multiple elevations

Figure 5.17 shows the PDF of the acceleration amplitude along the elevation profile selected at multiple moments. The acceleration at any time generally appears as an amplifying effect with increasing elevation. The middle and upper parts of the slope may also suffer during heavy earthquakes when the time is fixed. There is a certain skewed distribution when the acceleration amplitude increases and when the acceleration amplitude range in exterior normal direction of the slope is slightly larger than the amplitude range in the interior normal direction. This may be caused by the asymmetric structure of the slope and a certain degree of material nonlinearity.

b. Analysis of equivalent extreme events

Several studies have addressed the elevation amplification effect of slopes because the effect is instructive for designing site selection rules, slope performance, and risk mitigation for buildings in mountainous areas. The steps to investigate and analyze these elevation amplification effects on the acceleration underground motion are as follows.

Extract the maximum seismic acceleration of each monitored point under a certain earthquake stimulation. Compare the response spectrum with that of the base under the seismic excitation to obtain the amplifying factor of the seismic excitation by dividing one by the other. The initial probability of the ground motion should be attached to the amplifying factor.

The probability that an incident occurs should not break the conservation rule, thus the amplifying coefficients and probability of each elevation under ground motion should be acquired by traversing all of the ground motions.

On the basis of the equivalent extreme events, a virtual stochastic method with uncertainty is constructed in this process to solve the PDF of the slope amplifying factor.

Combined with the above analysis, Figs. 5.18 and 5.19 show the slope amplifying factor along the elevation distribution. The amplifying factor at each slope elevation is not a constant, but presents a norm-like distribution.

In general, the acceleration amplifying factor, variability, and probability gradually increase with elevation. The distribution range of the density function accordingly broadens, which implies that the slope dynamic response is more stochastic and becomes harder to predict with increasing elevation.

Most of the horizontal acceleration magnifying coefficients on the slope top exceed 1.5 with a non-transcendental probability of 97%, and the overall distribution is between 1.5 and 3.0, as shown in Fig. 5.20.

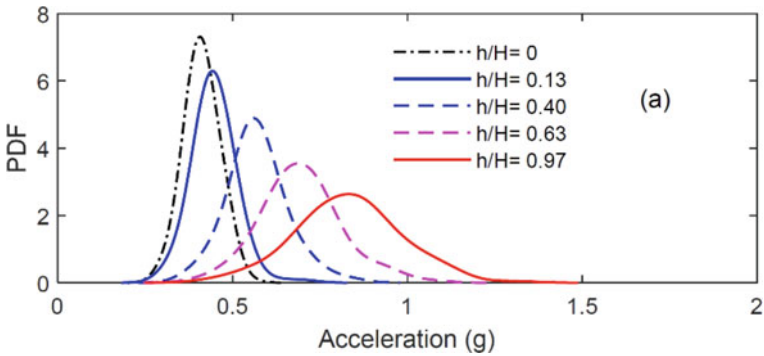


Fig. 5.18 PDF curves of the acceleration elevation amplifying factor

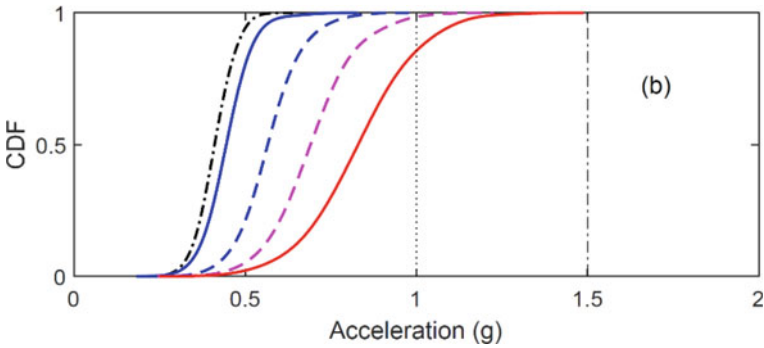


Fig. 5.19 CDF curves of the acceleration elevation amplifying factor

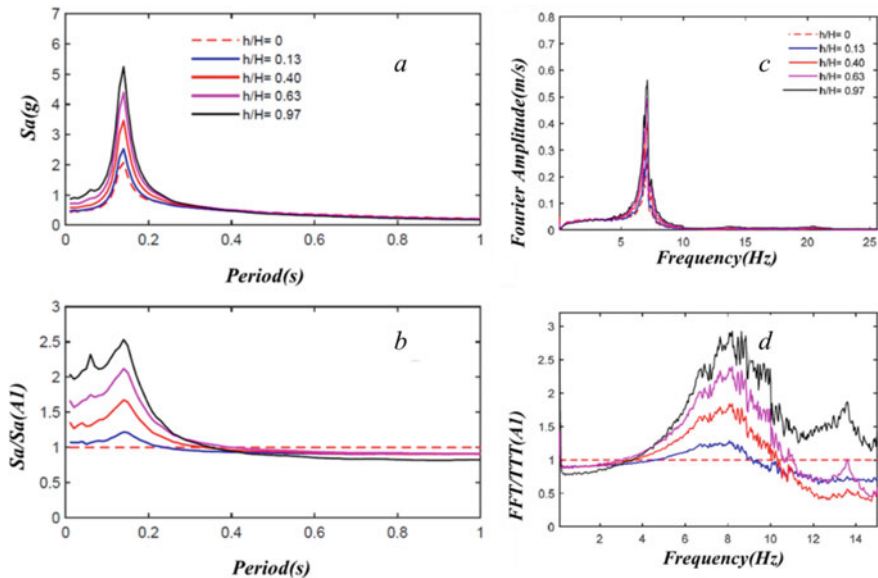


Fig. 5.20 Amplifying coefficient curves based on the average response spectrum under seismic excitation conditions **a, b**, and amplifying coefficient curves based on the average Fourier spectrum under seismic excitation conditions **c, d**

The average value of the slope top amplifying factor is 2.02, and the standard deviation is 0.27. Similarly, the MSD of the amplifying factor increases with slope elevation. It is therefore suggested that the peak design ground motion value of sites should be doubled when buildings or structures are located on top of an engineering slope, and the design calculation should be carried out for security and assurance.

(3) Spectral amplification under vibration

The reason for the concentration the frequency components of the ground motion within the range of 6–7 Hz under the influence of ground motion is explained as follows.

The inherent frequency of the slope model is 34 Hz and the prototype inherent frequency is 6.8 Hz under similar laws. The energy dissipates only slightly during the transfer process, which amplifies the pieces of the ground motion samples close to the inherent frequency.

The high-frequency component of the input seismic sample is filtered.

Conventional shaking table amplifying coefficients are mostly obtained from the horizontal acceleration peak amplification. However, limited research has addressed the frequency domain amplification. Figure 5.20a, b show the average value of the response spectrum for a damping ratio of 0.05 obtained from 144 ground motion inputs of multiple measurement points with increasing elevation. Only the part with the period within 1 s is shown because the slope frequency is fairly high. The results

indicate that the peak acceleration response spectrum corresponding to the predominant period of the slope is 0.147 s ($1/6.8 \text{ Hz} = 0.147 \text{ s}$). The amplifying coefficient curve of the response spectrum is obtained by dividing the average response spectrum at different elevation positions by the reference acceleration A_1 at the slope bottom.

The amplifying coefficient curve based on the average response spectrum is shown in Fig. 5.20a, b. The amplifying coefficient at the slope top near the slope inherent frequency is 2.53, which is 20% larger than 2.02, and thus represents the peak horizontal ground motion value. The amplifying coefficient curve using the fast Fourier transform (FFT) method is shown in Fig. 5.20c, d. The average values are calculated based on the statistical analysis of 144 ground motion samples as follows.

- a. Average horizontal acceleration peak amplifying coefficient
- b. Average horizontal acceleration response spectrum amplifying coefficient
- c. Average horizontal acceleration Fourier spectrum amplifying coefficient.

Figure 5.21 quantifies the result that the average amplifying coefficient of the peak horizontal acceleration value (2.02) is the smallest, that of the response spectrum of the (2.53) is the second largest, and that after the FFT treatment (2.93) is the largest.

In general, closer relationships between the slope inherent frequency and seismic sample are associated with larger amplifying factors. The average value of the

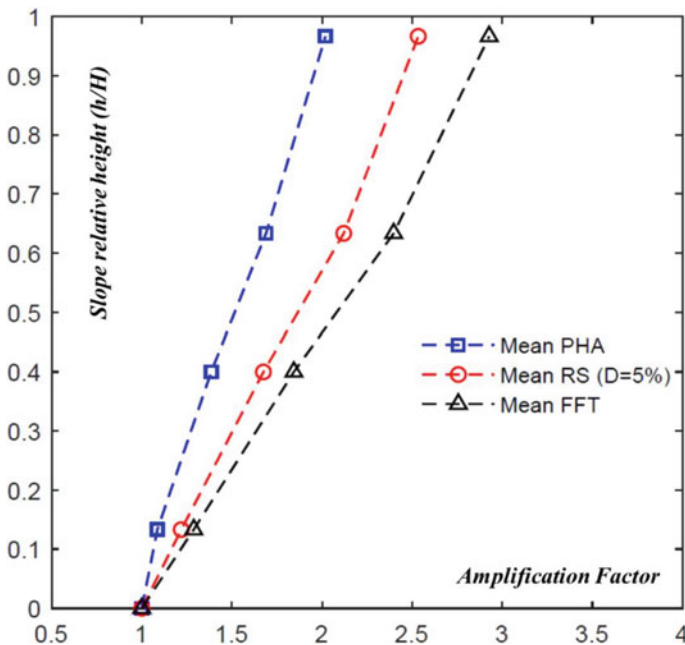


Fig. 5.21 Comparison of the different amplifying factors with elevation during ground motion input (reprinted from Zhao et al. (2020) with permission of Elsevier)

response spectrum is also smaller than the Fourier spectrum amplifying factor owing to the use of an impedance ratio of 0.05. The response spectrum value is inversely proportional to the damping ratio.

5.2.3 Seismic Dynamic Reliability Analysis of Slope

(1) Critical acceleration of slope model

The reliability analysis indicators of slope failure caused by ground motion mainly include the minimum safety factor, vertical settlement or horizontal displacement at the slope top, and the critical acceleration. The minimum safety factor is often used in numerical calculations; however, the displacement obtained from each condition in this test is small. The critical acceleration is accordingly selected to assess whether or not the slope top is cracked. Further slope fracture analysis, such as when the initial condition is a large amplitude input, indicates that the test slope is visibly cracked under tensile forces when the horizontal acceleration of the test slope at the measurement point on the slope top is greater than 1.5 g.

(2) Slope dynamic reliability for engineering design

Figure 5.22 shows the maximum acceleration response of 144 ground motions at each measurement point. The response of the A29 horizontal acceleration sensor at the slope top under ground motion is less than the critical acceleration (1.5 g), which indicates that the dynamic reliability of the test slope under the test conditions is 100% and effectively meets the requirements of multiple tests.

Although the slope is stable in the random test, the dynamic reliability method used in this section can be extended to engineering practice. The PDF of the horizontal acceleration at slope top is acquired based on the site design seismic peak and ground motion sample test result. The tensile strength values of the material are deterministic and converted into the corresponding critical acceleration values of the material at the slope top based on the indoor experiment and engineering practice experience. The CDF curves are then calculated via integration based on the PDF of the horizontal acceleration dataset. Combined with the critical acceleration value obtained in the above step, the tensile crack failure probability at the top of the design slope is obtained.

5.3 Comparison with Numerical Modeling Results

In this section, numerical calculations performed using FLAC3D, a program that uses the finite differential method, is applied to compare with the seismic shaking table test results. The geometric model is built in the prototype size, thus there is no concern regarding similarity problems. When the nonlinear constitutive models are

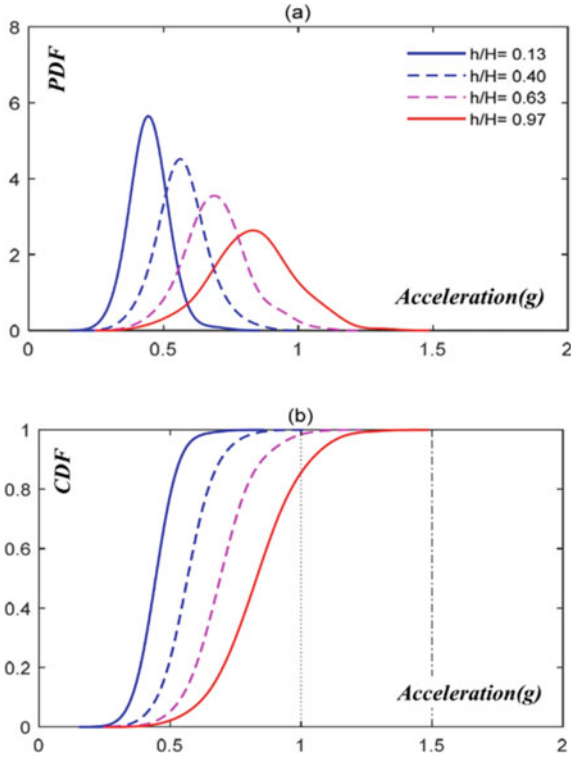


Fig. 5.22 Dynamic reliability of slope top cracking failure based on critical acceleration

applied on the materials, Rayleigh damping should be adopted to temporally delay the effects for dynamic excitations. A free field absorption boundary condition is added on the bottom and side walls of the numerical model to eliminate the reflection led by the propagation of the seismic excitations. Figure 5.23 shows a profile of the displacement contours that correspond with the slope model pretest.

The Gaussian white noise and 144 seismic samples shown in Fig. 5.24 are adopted to simulate the seismic acceleration with a certain intensity. The PGA magnitude at an elevation of 1.2 m is quite distinct from that at 0.1 m, which provides evidence of the amplification effect at the slope top. The first two order inherent frequencies are captured as 35 and 85 Hz.

Figure 5.25 compares the horizontal acceleration response obtained at the same elevation inside the slope of the Wn 1 seismic sample. The results of the response in the shaking table tests and numerical calculations are generally consistent with the temporal and frequency spectra. The shaking table test results are therefore considered credible by comparison with the numerical calculation results. Further work is required to quantify the similarity and account for the unexpected differences.

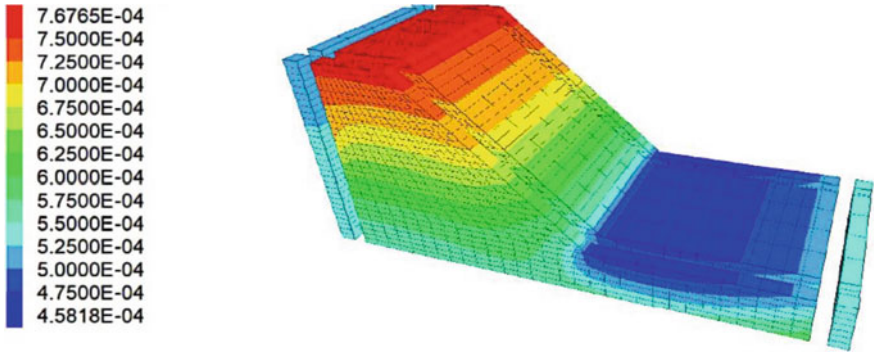


Fig. 5.23 Displacement contours of the 3D calculation model and test seismic excitation input

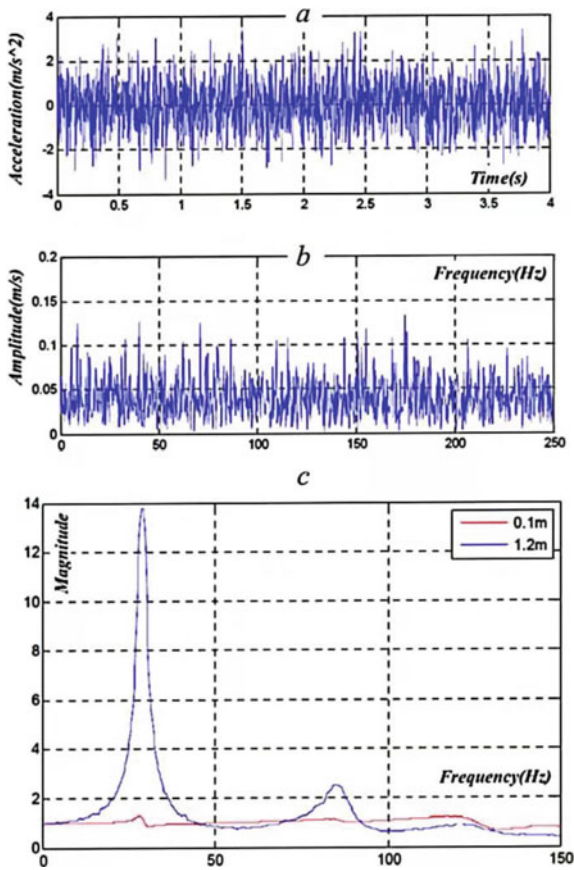


Fig. 5.24 Gaussian white noise time and frequency spectra a, b, respectively. Dynamic characteristics test of the Gaussian white noise model c

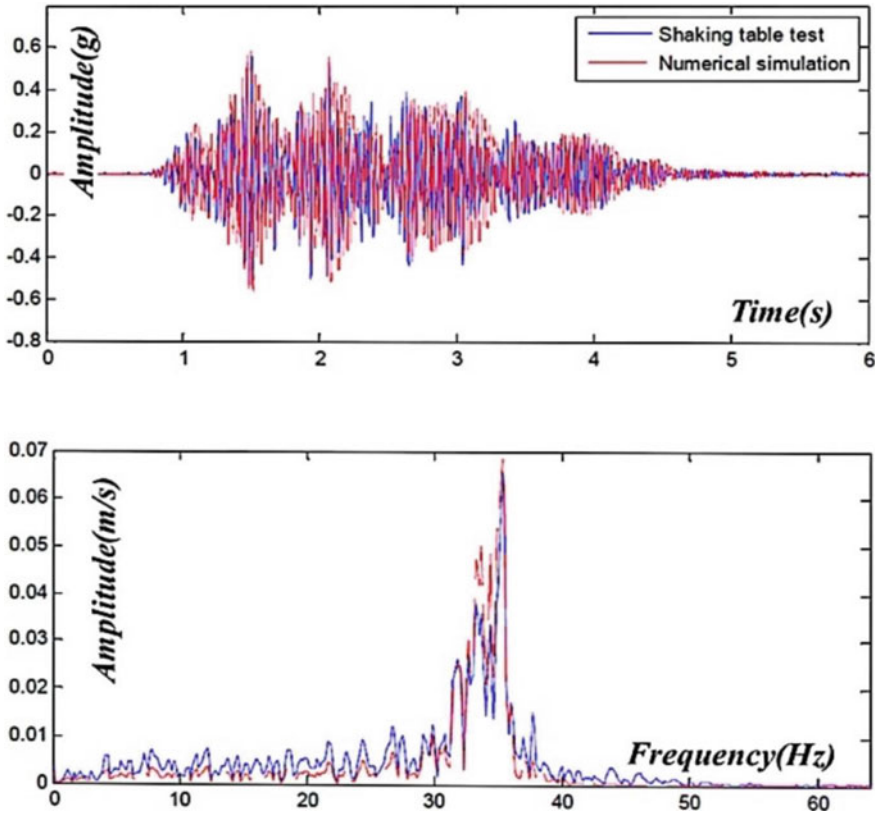


Fig. 5.25 Horizontal acceleration response of sensor A9 in the slope under ground motion Wn 1

References

- Aydan, Ö., & Kumsar, H. (2009). An experimental and theoretical approach on the modeling of sliding response of rock wedges under dynamic loading. *Rock Mechanics and Rock Engineering*, 43(6), 821–830.
- Buckingham, E. (1914). Illustrations of the use of dimensional equations. On physically similar systems, 6.
- Fan, G., Zhang, J., Wu, J., et al. (2016). Dynamic response and dynamic failure mode of a weak intercalated rock slope using a shaking table. *Rock Mechanics and Rock Engineering*, 49(8), 3243–3256.
- Hot rolled section steel. (2008). *General Administration of Quality Supervision, Inspection and Quarantine of the People's Republic of China*, vol. GB/T 706–2008. Beijing: Standardization Administration of China.
- Huang, C., Horng, J., Chang, W., et al. (2011). Dynamic behavior of reinforced walls – Horizontal displacement response. *Geotextiles and Geomembranes*, 29(3), 257–267.
- Huang, R., Zhao, J., Ju, N., et al. (2013). Analysis of an anti-dip landslide triggered by the 2008 Wenchuan earthquake in China. *Natural Hazards*, 68(2), 1021–1039.

- Huang, Y., Han, X., & Zhao, L. (2021). Recurrent neural networks for complicated seismic dynamic response prediction of a slope system. *Engineering Geology*, 289, 106198.
- Jiao, Y., Tian, H., Wu, H., et al. (2014). Numerical and experimental investigation on the stability of slopes threatened by earthquakes. *Arabian Journal of Geosciences*, 8(7), 4353–4364.
- Li, Z., Ju, N., Hou, W., et al. (2012). Large-scale shaking table model tests for dynamic response of steep stratified rock slopes. *Journal of Engineering Geology*, 20.
- Lin, M., & Wang, K. (2006). Seismic slope behavior in a large-scale shaking table model test. *Engineering Geology*, 86(2–3), 118–133.
- Liu, H., Xu, Q., Li, Y., et al. (2013). Response of high-strength rock slope to seismic waves in a shaking table test. *Bulletin of the Seismological Society of America*, 103(6), 3012–3025.
- Liu, J., Liu, F., Kong, X., et al. (2014). Large-scale shaking table model tests of aseismic measures for concrete faced rock-fill dams. *Soil Dynamics and Earthquake Engineering*, 61–62, 152–163.
- Liu, J., Liu, F., Kong, X., et al. (2016). Large-scale shaking table model tests on seismically induced failure of concrete-faced rockfill dams. *Soil Dynamics and Earthquake Engineering*, 82, 11–23.
- Ng, C. W. W., Li, X. S., Van Laak, P. A., et al. (2004). Centrifuge modeling of loose fill embankment subjected to uni-axial and bi-axial earthquakes. *Soil Dynamics and Earthquake Engineering*, 24(4), 305–318.
- Palchik, V. (2010). On the ratios between elastic modulus and uniaxial compressive strength of heterogeneous carbonate rocks. *Rock Mechanics and Rock Engineering*, 44(1), 121–128.
- Shi, Z., Wang, Y., Peng, M., et al. (2015). Landslide dam deformation analysis under after-shocks using large-scale shaking table tests measured by videogrammetric technique. *Engineering Geology*, 186, 68–78.
- Shinoda, M., Watanabe, K., Sanagawa, T., et al. (2015). Dynamic behavior of slope models with various slope inclinations. *Soils and Foundations*, 55(1), 127–142.
- Tang, L., Cong, S., Ling, X., et al. (2017). The boundary conditions for simulations of a shake-table experiment on the seismic response of 3D slope. *Earthquake Engineering and Engineering Vibration*, 16(1), 23–32.
- Technical Code for Building Slope Engineering. (2013). China General Administration of Quality Supervision, Inspection and Quarantine, vol. GB 50330–2013. Beijing: China's Ministry of Housing and Construction.
- Wang, K., & Lin, M. (2011). Initiation and displacement of landslide induced by earthquake—a study of shaking table model slope test. *Engineering Geology*, 122(1–2), 106–114.
- Wang, J., Yao, L., & Hussain, A. (2010). Analysis of earthquake-triggered failure mechanisms of slopes and sliding surfaces. *Journal of Mountain Science*, 7(3), 282–290.
- Xu, Q., Liu, H., Zou, W., et al. (2010). Large-scale shaking table test study of acceleration dynamic responses characteristics of slopes. *Chinese Journal of Rock Mechanics and Engineering*, 29.
- Yang, C., Zhang, J., Liu, F., et al. (2015). Analysis on two typical landslide hazard phenomena in the wenchuan earthquake by field investigations and shaking table tests. *International Journal of Environmental Research and Public Health*, 12(8), 9181–9198.
- Yang, G., Ye, H., Wu, F., et al. (2012). Shaking table model test on dynamic response characteristics and failure mechanism of antidip layered rock slope. *Chinese Journal of Rock Mechanics and Engineering*, 31.
- Yuan, L., Liu, X., Wang, X., et al. (2014). Seismic performance of earth-core and concrete-faced rock-fill dams by large-scale shaking table tests. *Soil Dynamics and Earthquake Engineering*, 56, 1–12.
- Zhao, M., Huang, D., Cao, M., et al. (2015). Shaking table tests on deformation and failure mechanisms of seismic slope. *Journal of Vibroengineering*, 17(1).
- Zhao, L., Huang, Y., & Hu, H. (2020). Stochastic seismic response of a slope based on large-scale shaking-table tests. *Engineering Geology*, 277.

Chapter 6

Conclusions and Prospects



6.1 Conclusions

This book investigates slope as the research object and a nonlinear stochastic dynamic system. A theoretical framework of the nonlinear stochastic dynamics of slope systems is established in combination with physical experiments and numerical analysis. This book focuses on the slope nonlinear stochastic seismic dynamic response, dynamic reliability, and failure phenomena. The entire stabilization process is systematically addressed, focusing on the key scientific problems of slope dynamic conservative systems and evolution processes. The main findings are summarized below.

- (1) A theory of slope nonlinear stochastic seismic dynamic systems is established at the theoretical level. The response of slopes to earthquake activity is considered to be a dynamic conservative system. The slope stochastic dynamic analysis theory is introduced, which includes the establishment of stochastic models of seismic ground motions and rock and soil parameters based on site characteristics, and a probability density evolution equation according to the description of random events. The analysis theory of slope stochastic dynamic systems is established with a theoretical foundation for slope seismic dynamic stability evaluation.
- (2) At the numerical simulation level, the seismic dynamic reliability of slopes is studied under a framework of a probabilistic conservative system under seismic excitations. It is proposed that the slope stochastic dynamic system should be regarded as a probabilistic conservative system, and the slope seismic dynamic reliability is analyzed in combination with the slope stochastic dynamics theoretical framework. The main conclusions are as follows.
 - a. Taking the finite element method (FEM) as an example, probability density evolution method (PDEM)-based slope dynamic reliability analysis is proposed, which considers the nonlinear constitutive relationship of rock and soil materials in combination with the basic steps for solving the

- generalized probability evolution equation (GDEE) using an FEM batch calculation.
- b. The Karhunen-Loève (K-L) series expansion method is used to simulate the stochastic field of the soil parameters, and a spectral representation of non-stationary ground motions is established, namely, the stochastic function simulation method.
 - c. The probability distributions of slope stochastic dynamic response results considering single random factor and double random factors are resolved and subsequently compared and analyzed based on extreme events.
 - d. Monte Carlos simulations (MCS) are used to calculate and verify the effectiveness of the PDEM-based slope dynamic reliability analysis method proposed in this book at both the static and dynamic levels. This method is also verified by the analytical solution of the single degree of freedom system.
- (3) The failure analysis of slope under stochastic earthquake conditions is undertaken at the application level, and the critical slip surface information, dynamic instability mechanism, and behavior analysis after failure are investigated. The uncertainty of the slope instability volume under stochastic ground motions is proposed based on different deformation development modes defined by the designed framework for risk assessment.
- a. The critical sliding surface can be determined once the factor of safety is lower than 1, which is the most conservative determination principle. The landslide volume can also be determined. The three-dimensional probability density evolution surface directly reflects the uncertainty of slope failure under random earthquake conditions, including the uncertainties of the sliding volume and sliding depth.
 - b. Large deformation analysis of soil mass flow hazards is performed based on the probability assessment method for large deformation flow hazards of soil mass and considering the spatial variability of rock and soil materials. The probability density surface of the time-sensitive flow slip parameters is obtained, as well as their PDF and CDF curves based on the equivalent extreme events. The PDF curves present complex probability evolution characteristics with time owing to the soil spatial variability. The PDF curves based on extreme events exhibit bimodal or multimodal characteristics.
- (4) The stochastic dynamic response analysis of slopes was studied using a large shaking table test. A slope shaking table model was appropriately designed and slope shaking table tests were performed under stochastic seismic input conditions. The stochastic dynamic response law of the slope system was determined and verified from the perspective of the physical experiment. The accuracy of the analysis results and effectiveness of the theoretical methods are expected

to be supplied as a scientific and effective theoretical basis for the performance assessment of slope engineering and prevention and control of seismic geological disasters.

- a. The PDF of acceleration response at a given elevation exhibits a normal distribution with mean value of 0 under the time sequence. The distribution range slightly increases with time and ultimately returns to the initial stage at the end of the ground motion. The PDF of the acceleration response at different elevations and a given time also presents a normal distribution with mean value of 0. The dependent value, probability, and variability increase with increasing slope elevation, which demonstrates the amplifying effect of horizontal acceleration. The PDF of acceleration response presents a skewed distribution when the peak ground motion is large and the instantaneous acceleration at the slope top is even greater than 0.8 g. This is caused by the coupling effects of the material non-linearity and randomness of seismic samples.
- b. The horizontal acceleration peak values of 144 points are extracted during the ground motion and compared with the base acceleration peak value to obtain the amplifying coefficient. The results indicate that the amplifying factor at the different slope elevations follows a Gaussian distribution, and its mean value and standard deviation increase with elevation. 79% of the horizontal acceleration amplifying factors on the slope top are greater than 1.5, and mainly distributed between 1.5 and 3.0.
- c. Average value of amplifying coefficient based on acceleration peak is the smallest, that based on the acceleration response spectrum is the second largest, and that based on the acceleration Fourier spectrum is the largest. The reason is that the amplifying factor of the acceleration peak does not consider the amplification of the specific spectrum, but damping is used in the calculation of acceleration response spectrum, which will likely reduce the amplitude of the response spectrum.
- d. The prototype slope is established as a numerical model using FLAC3D with dynamic load input and free field boundary conditions. The amplitude and frequency spectrum of the dynamic response at each elevation show good consistency with the modal test data as a verification.

6.2 Prospects

Although this book presents a range of research on the stochastic dynamic analysis of slopes, there is still room for further development. The future development prospects of this theoretical method are summarized in the following aspects.

(1) *Probabilistic dissipative system research*

An important assumption of the slope stochastic dynamic framework established in this book is that the slope system is a probabilistic conservative system,

in which the total mechanical energy of the system is conserved during movement. However, the conservative probability system based on the principle of probability conservation is not completely suitable for slope dynamic systems. This is because slopes tend to exhibit strong nonlinearity under large earthquake load conditions, and even large-scale dynamic instability and large deformation will occur. Friction, damping, viscosity, impact, and other non-conservative forces presently work for slope dynamics, which implies that the analysis based on slope stochastic dynamics must inevitably face probability dissipation analysis. Slope systems should therefore be regarded as a probabilistic dissipation system. It should be pointed out that the probabilistic dissipative system and probabilistic conservative system are not contradictory, but that their analysis frameworks differ at different design levels of ground motions. For small earthquakes, slopes tend to remain stable and can be regarded as a probabilistic conservative system. Even when regarded as a probabilistic dissipative system, the probability distribution remains completely in the safe domain and the two are equivalent to each other. However, analysis using a probabilistic dissipation framework has a clearer physical meaning and theoretical basis when the ground motion magnitude is large.

(2) ***Guidance on slope performance evaluation***

Supporting structures are one of the most effective methods for slope anti-seismic design, reinforcement, and landslide prevention. Traditional seismic performance evaluation and supporting structure design are mostly based on deterministic theory, which often fails to consider the impact of uncertain factors on the seismic performance of slope supporting structures. In practice, the overall slope performance will be affected by uncertain factors originating from different sources during the design service period of the supporting structure. The existing design methods can be optimized according to the stochastic dynamic response of slope in combination with the slope stochastic dynamic theory established in this book, and the seismic performance design and risk assessment of slope engineering can be carried out considering random factors. Resilience is a new disaster prevention and reduction method that can be used as a new perspective to enhance the practical operability and sustainability of the theoretical framework presented herein by focusing on the performance of materials and structures throughout their life cycle to provide useful theoretical tools for slope performance evaluation in engineering applications.

(3) ***New fields in artificial intelligence***

The amount of calculation required for the stochastic dynamic analysis of slopes is still relatively large. The PDEM is proposed in this book to solve the shortcomings of the large amount of calculation and time-consuming problems of the MCS method. However, this approach is still limited by the time-consuming nature of the calculation for each single deterministic sample. A new method to reduce the calculation amount and deterministic analysis time using existing research is therefore a potential development direction in the future. Big data analysis has become the focus in various scientific fields in

recent years, including the development of machine learning methods (e.g., artificial neural networks, deep learning, and genetic algorithms), which have made significant progress in data extraction, identification, and prediction. Machine learning algorithm research based on the existing experimental data can therefore be carried out in subsequent work. The response related to slope engineering can be determined by means of continuous training and learning, and the internal propagation mechanism of randomness can be deeply studied to resolve the problem of insufficient computational efficiency in randomness performance analysis problems.